THE UNIVERSITY *of* EDINBURGH

Input to output transfer in neurons

Miha Pelko

Doctor of Philosophy

Institute for Adaptive and Neural Computation

School of Informatics

University of Edinburgh

2015

Abstract

Computational modelling is playing an increasing role in neuroscience research by providing not only theoretical frameworks for describing the activity of the brain and the nervous system, but also by providing a set of tools and techniques for better understanding data obtained using various recording techniques. The focus of this thesis was on the latter - using computational modelling to assist with analyzing measurement results and the underlying mechanisms behind them.

The first study described in this thesis is an example of the use of a computational model in the case of intracellular *in vivo* recordings. Intracellular recordings of neurons *in vivo* are becoming routine, yielding insights into the rich sub-threshold neural dynamics and the integration of information by neurons under realistic situations. In particular, these methods have been used to estimate the global excitatory and inhibitory synaptic conductances experienced by the soma. I first present a method to estimate the effective somatic excitatory and inhibitory conductances as well as their rate and event size from the intracellular *in vivo* recordings. The method was applied to intracellular recordings from primary motor cortex of awake behaving mice.

Next, I studied how dendritic filtering leads to misestimation of the global excitatory and inhibitory conductances. Using analytical treatment of a simplified model and numerical simulations of a detailed compartmental model, I show how much both the mean, as well as the variation of the synaptic conductances are underestimated by the methods based on recordings at the soma. The influence of the synaptic distance from the soma on the estimation for both excitatory as well as inhibitory inputs for different realistic neuronal morphologies is discussed.

The last study was an attempt to classify the synaptic location region based on the measurements of the excitatory postsynaptic potential at two different locations on the dendritic tree. The measurements were obtained from the *in vitro* intercellular recordings in slices of the somatosensory cortex of rats when exposed to glutamate uncaging stimulation. The models were used to train the classifier and to demonstrate the extent to which the automatic classification agrees with manual classification performed by the experimenter.

Acknowledgements

Although my name stands at the top of this document, the content would be nowhere close to what it is without a contribution of many individuals I was fortunate enough to share the time and thoughts with throughout these years.

First and foremost I would like to thank Mark van Rossum for taking a chance on me and showing me how science should be done. He is a supervisor anybody can only wish for. With a way to perfectly balance guiding you through your research while at the same time challenging you to find your own way, he really makes it hard to complain about him on the standard group therapy sessions PhD students often hold. Thank you Mark.

Next I want to thank my secondary supervisor Clemens Boucsein and two of his students from Freiburg university Mihael Zohar and Philipp Schnepel who have introduced me to the world of experimental neuroscience with all its glory and sweat. Specifically, the experiments in chapter 4 were performed by Mihael Zohar.

Remember the name Paolo Puggioni. He is going to make it big, wherever he decides to go for. Besides other things, he was the one behind the experiments and analysis in the chapter 2.

I further want to thank the unsung heroes of science - the authors of the open-source scientific software. Keep on fighting the good fight, you are truly providing the building blocks of future in science.

Thanks to Scott, Sander and Martina for taking your time to fight with my inability to ever learn the role of (the?) prepositions. My Slavic soul will be forever grateful.

On a more social note, thanks to the many fellow students in Edinburgh and Frieburg for all the discussions we had over the years. You really made it a fun period of my life.

To the other friends and family thanks for the support and apologies for all the times you had to hear the "after I finish the PhD" excuse. I will do my best to make it up to you.

Finally, thank you Martina. You have been amazing all these years. Here's to the future!

Declaration

I declare that this thesis was composed by myself, that the work contained herein is my own except where explicitly stated otherwise in the text, and that this work has not been submitted for any other degree or professional qualification except as specified.

(*Miha Pelko*)

Contents

Chapter 1

Introduction

The brain is a complex organ present in all higher organisms. It is responsible for integrating information about both the external as well as the internal world of the organism (received via various sensory pathways) [1, 2]. The information is received and transformed within the brain to yield the instructions to a motor system capable of acting and influencing the external world and the inner workings of the organism. At the same time information processing also transforms the brain itself making it possible for organisms to learn and adapt their responses on timescales ranging from milliseconds up to years.

All this complex information processing is believed to be primarily achieved through the interaction of a specific subset of the cells making up the brain - the neurons. The neural membrane is capable of maintaining a voltage gradient between the inside and the outside of the neuron via ion pumps using metabolic energy to push ions against the driving electrical potential. Neurons are capable of influencing the membrane voltage of other neurons through electrical and chemical signals [3, 4] transmitted via connections called synapses [5]. In this thesis I focus on the chemical synapses which convey the information in the direction from a presynaptic neuron to a postsynaptic neuron.

Neurons can be grouped according the function they perform (e.g. sensory neurons responding to external stimulus, motor neurons transmitting the information from the brain to the muscles, etc.), or by the type of the influence they have on the neuron they are connected with via a synapse (excitatory neurons increasing the membrane potential and inhibitory neurons decreasing it). Each of the groups is further split in many subclasses defined by their specific shape and electrophysiological properties [6].

Although the size and morphology of neurons widely varies even within the same

organism, they typically consist of a cell body called a soma and thin tube-like structures extending and branching out of the soma called neurites. The neurites are further split into dendrites and an axon. Synapses are mostly located on the dendrites and the soma and receive the input (excitation or inhibition of the membrane) sent via the axon of the presynaptic neuron.

An example of a neuron is presented in figure 1.1 (bottom). It presents a distinct type of an excitatory neuron named pyramidal cell (more specifically this is a layer 5 pyramidal cell from the rat barrel cortex). Typically for this type of cell we observe a bushy collection of dendrites surrounding the soma called the basal dendrites and one more prominent dendrite called the apical dendrite which extends further from the soma and branches out in a region named the apical tuft (green background in the figure). The image does not include the axon which also typically extends far from the neuron and branches out.

Such a tubular structure allows the neurons to connect to each other over long distances without taking a huge proportion of the tissue required for other supporting cells (glial cells, blood vessels) as well as allowing for a complex connectivity structure. Apart from getting the signals to the soma the neurites also influence the signal processing of the cell [7, 8, 9, 10].

A simplified version of the signal processing performed by the cell is presented in figure 1.1. The neuron receives a set of signals from the excitatory and inhibitory presynaptic cells and integrates them into its own membrane voltage. At the soma and the initial segment of the axon, the neuronal membrane is densely equipped with voltage-gated sodium channels giving rise to the spikes in the voltage called action potentials. Action potentials are transient events propagated along the axon of the neuron and passed onto the next cells.

In order to study information processing properties of neurons and their networks, the field of computational neuroscience often resorts to building models at multiple spatial-temporal scales. The level of detail at which those models are constructed depends on the task at hand - whether it is describing the observed physiological behavior of a neuron following external simulation, finding the plasticity principles in neural networks leading to the emergence of receptive fields, etc. Following the Occam's razor principle, the models should simple as possible while still explaining the observations.

To be able to handle the complexity and the huge number of neurons present in the brain or its subsystems the models are often simplified. Many of those simplifications

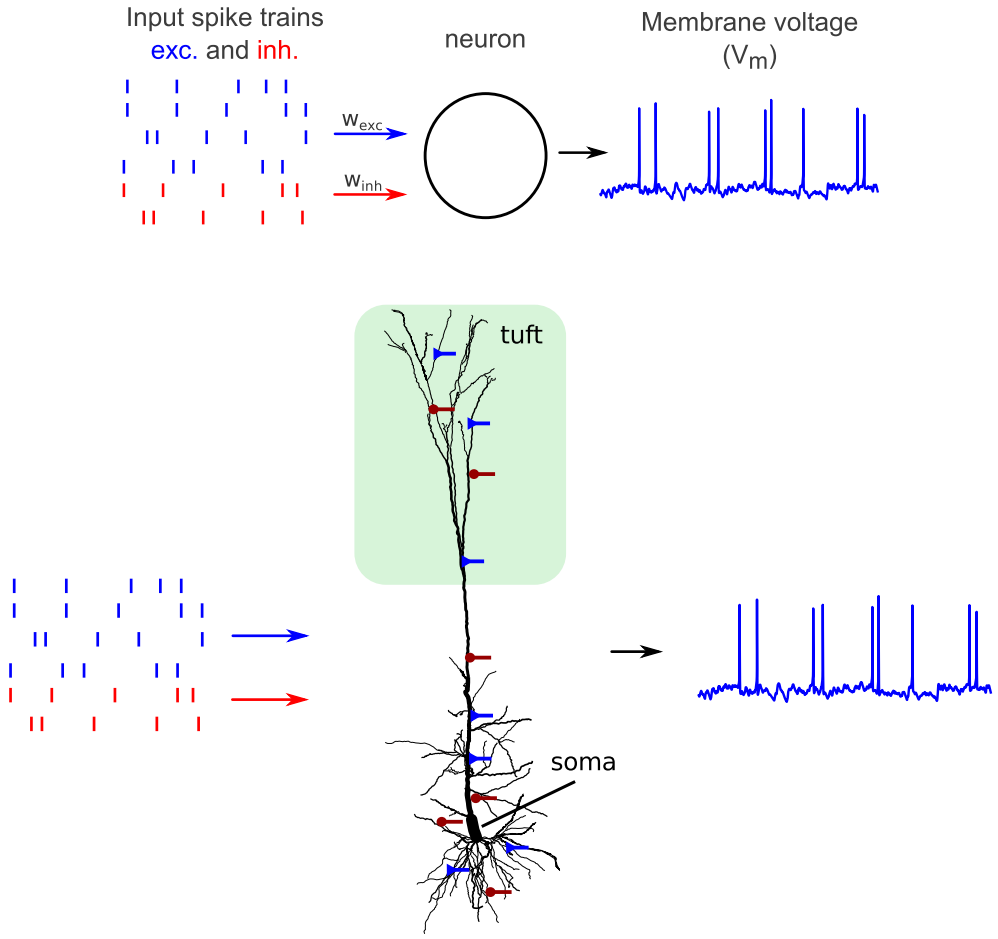

Figure 1.1: **Two levels of complexity in neuronal models.**
(top) Simplification of the single neuron as a single compartment which receives discrete excitatory (blue) and inhibitory (red) events from the presynaptic neurons and integrates them into their own membrane voltage with a nonlinear process. The nonlinear process gives rise to the spikes in the activity called action potentials which cause the discrete events passed on to the cells further down the signal processing chain.
(bottom) Same general process as above but with a higher morphological complexity of the target neuron. Here the inputs are being passed to synapses spread along the full dendritic tree of the cell. All of the inputs are again integrated with the focal point at the soma. In this case we observe an additional effect on the input processing, as the input influence on the membrane voltage is being modified as it is propagated along the dendritic tree.

include collapsing the morphology of the neurons into a single point where the inputs are being integrated and transformed to discrete time events (representing action potentials) or a continuous activity value corresponding to the frequency of action potentials (firing rate). An illustration of such simplified models is shown in figure 1.1 (top).

While the models under such simplifications can express a wide range of dynamical behaviors that resemble several of the dynamical states observed in recordings [11, 12] and have found recent success in fields less concerned with understanding the true workings of the brain but more with the practical applications of artificial neural networks such as image or speech recognition [13, 14], they ignore the obvious effects of morphology on the input-output transformation of the neurons.

One of those effects is changing of the size and the shape of input signals as they reach the soma [15, 8]. Dendrites can be treated as electrical cables with bad insulation (leak conductance). As the signals are being propagated along the dendrites towards the action potential initiation zone (soma or axon initial segment) they are filtered, attenuating and broadening the otherwise sharp post-synaptic potentials (PSPs). The influence of the individual synaptic input will thus depend on the electrotonic distance between the synapse and the initiation zone.

Another way the morphology influences input integration is by electrotonically separating the input locations. Synaptic inputs are conductive – each signal is passed by a transient local increase in conductance (opening of the receptors) specific to certain ions with their respective reversal potential. The size of the input signal will depend on the amount of conductance increase and on the difference between the membrane and the reversal potential (driving force). This for example leads to a sublinear summation of the excitatory inputs, as each excitatory input will decrease the driving force for another excitatory input occurring close in time and space. The complex dendritic structure of neurons allows for a separation of the synaptic location and counter this sublinear effect.

Two illustrative examples of how morphology influences the input integration properties are presented in figure 1.2 where I perform a multi-compartmental numerical simulation of the input integration of exclusively excitatory conductive inputs on the layer 5 pyramidal neuron from somatosensory cortex of a rat (morphology shown in figure 1.1).

The top figure shows the effect on the morphology on the output spike times of a neuron. Each of the 20 rows of blue dots on the top plot represents the output spike times of the simulated neuron caused by the input to 500 excitatory synapses located

randomly on the dendritic tree of the neuron. For each row the locations of the synapses are redrawn from a uniform distribution while the input spike times remain the same for all the rows (a "frozen" Poisson train with the 4Hz firing rate for each synapse) so that if synaptic locations are fixed, repeating the stimulus yields the same output. The total input (averaged over 10 ms time window) is presented in the bottom of the plot (green). Although there is clear similarity among the spike trains, every case has a distinct set of output spike trains. Any type of the spike-time dependent code [16] will be affected by the locations of the synapses.

On the bottom plot I show how not just the spike times, but also the input-output spike frequency relationship is affected by synapse locations. Each curve represents a specific distribution of the 500 excitatory synapses on the dendritic tree. The synapses are either all located on the soma (blue), on the dendritic tuft (green) or uniformly distributed along the dendritic tree (red). As the input frequency at each synapse (input timings are Poisson trains with a target frequency) are changed, the output frequency of the neuron is recorded. The observed input-output relationships are very different for each distribution due to the attenuation of the inputs from the synapses further away from the soma.

Another way the morphology might play a role in neuronal computation is through the presence of voltage dependent channels on the membrane of the dendrites [9]. The distribution of those channels along the dendrites is often nonuniform and characteristic for specific neuron types and will lead to further nonlinearities in input integration [17]. While those nonlinearities are typically superlinear and their effect can partially counter the attenuation of the distal inputs, the effects are typically more complex [18, 19, 20].

Summary of Aims

So far the process of how the neuronal inputs are transformed into the membrane voltage and output action potentials was described. This thesis is mostly focussed at the inverse problem - given the recorded membrane voltage of the neuron, what can be said about its inputs?

One of the more difficult types of recording of the neural activity in the brain is whole-cell recording of the membrane voltage of individual neurons [21, 22]. They give us the insight not only in the output of the neurons (the action potentials) but also in the internal subthreshold membrane voltage fluctuations. Typically those recordings

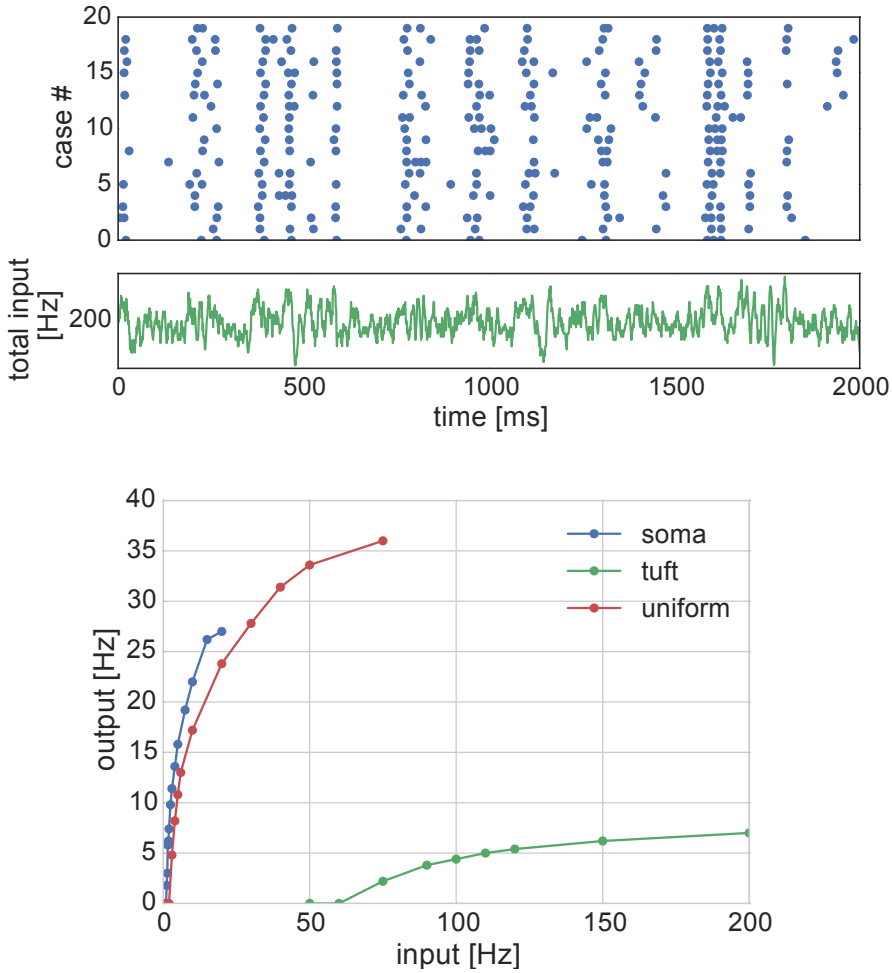

Figure 1.2: **The effect of synapse locations on the input-output characteristics of a neuron**

(top) Effect on the output spike times. Each row of blue dots represents the output of the simulated neuron caused by the input to 500 excitatory synapses located randomly on the dendritic tree of the neuron. For each row the locations of the synapses are re-drawn from a uniform distribution while the input spike times remain the same for all the rows (a "frozen" Poisson train with the 4Hz firing rate for each synapse). The total input (averaged over 10 ms time window) is presented in the bottom of the panel (green).

(bottom) Input-output frequency relationship for a neuron with different synapse locations. Each curve represents a specific distribution of the 500 excitatory synapses on the dendritic tree. The synapses are either all located on the soma (blue), on the dendritic tuft (green) or uniformly distributed along the dendritic tree (red). As the input frequency at each synapse (input timings are Poisson trains with a target frequency) is changed, the resulting change in output frequency of the neuron is recorded.

are performed at the soma (see figure 1.1). In chapter 2 of the thesis a method to estimate the statistics of the excitatory and inhibitory input based on those measurements is presented. The method builds up on the previously published methods focussed on the time-averaged inferences [23, 24] by including a temporal component. Specifically, we derive the analytical expression for the power spectral density of the membrane voltage of the post-synaptic neuron and apply the expression to estimate the rate and size of excitatory and inhibitory signals arriving to the soma. Those calculations are accompanied by numerical simulations. While the second order statistics of the membrane voltage has previously been used for the analysis [25], the full use of the power spectral densify for input estimation is novel. Finally the method is applied to recordings from the M1 cortex in awake mice during two conditions (voluntary movement and quiescence). The estimated change in the average excitatory and inhibitory conductance between the two conditions is not sufficient to explain the observed change in the power spectral density for a subset of the measured cells. Using single compartment neuron simulations we show that the added temporal correlation in the excitatory inputs could explain the observed power spectral density change.

As shown above (1), the neuronal morphology plays an important role in input integration. The method presented in chapter 2 ignores these effects and can thus only provide the estimations about the input events at the location of the recording (soma) and not about the synaptic inputs themselves. Chapter 3 aims to close this gap by examining the effects of neuronal morphology on the signals measured at the soma and how those effects influence the input estimations made under the point-neuron assumption. First the effects are analytically studied under the homogenous passive cable simplification [7, 8]. Finally the effects are studied for the actual neuronal morphologies using numerical simulations of input integration in the passive models of three morphologically distinct neuron types. While the underestimation of the input conductances due to the effects of neuronal morphology was a known and studied phenomena (for example see [26][7]), this chapter offers novel insights in how the morphology affects the estimation of the ratio between the excitatory and inhibitory conductance, which plays an important role in many findings and theories of information processing in the brain [27].

As we have shown in figure 1.2 the location of synapses is very important for the input integration and the output of the neuron. An attempt to determine the general region of the synapse location is presented in chapter 4. Using the simultaneous membrane voltage recordings from two different locations on the Layer 5 neuron from the

rat somatosensory cortex *in vitro* the inputs are classified as coming from the region closer to soma or the region closer to the main bifurcation (the tuft region in figure 1.1). The classification is performed based on the shape of the excitatory postsynaptic potentials (EPSPs) caused by the action potential of the presynaptic neuron stimulated by the dynamic photo stimulation (using the caged glutamate solution).

Appendix A presents a theoretical study in the intrinsic excitability homeostasis of neurons in neural networks which was a separate subproject within the PhD.

Chapter 2

Estimation of synaptic input from the intracellular recordings[1]

2.1 Introduction

The whole-cell patch clamp recording technique is a standard method for recording the membrane voltage of neurons [21, 22]. The method was initially applied *in vitro* to slices of brain tissue, allowing for the study of single or multiple ion channels within individual cells. Patch clamping also allows for the study of the synaptic inputs to the cell, which alter the membrane voltage and input resistance (figure 2.1 a). The membrane input resistance is measured indirectly, by injecting a current through the electrode and (with the same electrode) monitoring the response of the membrane voltage potential (figure 2.1 b). In recent years the method has also been applied *in vivo* with head-fixed, awake animals [28].

In the case of low input frequencies (e.g. in *in vitro* recordings in brain slices) it is possible to directly identify individual synaptic inputs, but under *in vivo* experimental conditions this is no longer possible since the individual inputs interfere with each other and mask individual contributions. Consequently, other approximate methods have been developed which attempt to estimate the levels of conductance under realistic *in vivo* conditions [29, 24, 30, 31] such as these.

One can ask: given the recorded membrane potential of a cell in two different neural states, what possible changes to the inputs can give rise to the observed differences

[1] All the experiments described in this chapter and the data analysis were performed by Paolo Puggioni from the University of Edinburgh. The paper describing the experiment and the thesis chapter is in review.

in the voltages? To answer this question, we developed a method for estimating the statistics of the inputs to the neuron based on the membrane voltage recordings which attempts to estimate the time-averaged firing rates of the excitatory and inhibitory inputs. Our method is based on the point neuron model approximation and is composed of two steps. First, we show how a change in time-averaged excitatory and inhibitory conductance between two states can be estimated by measuring the membrane voltage and the membrane input resistance, similar to [23, 24]. If the first state is a "silent" tissue state, where the measured neuron receives no inputs (*in vitro*), the estimated change corresponds to the input conductance levels in the second state. In the second step, the individual input sizes and frequencies are estimated using a novel approach based on the second-order statistics of the membrane voltage, namely its power spectral density.

Our underlying model is a single-compartment passive neuron ([32], for an overview of different neuronal model types see e.g. [8, 3, 4, 33]) and ignores the spatiotemporal properties of dendritic inputs or dendritic nonlinearities. What we estimate are thus the effects of the synaptic events to the soma after the processing by the dendritic nonlinearities and propagation along the dendritic tree. Despite the simplicity, such models were found to perform well in predicting the net effects of currents in the soma of a neuron [34, 12].

In the rest of the chapter, we first outline the analytical calculations, simulation details and data analysis methods which will be required for the estimation. Afterwards, the method is presented in detail and applied to real-data: recordings from pyramidal L5B cells in the mouse motor cortex. Here we also perform an additional step, where we adjust the timing statistics of the inputs to include the observed membrane fluctuations which go beyond the assumptions of our method.

In the final section of the chapter, the results are discussed and the underlying assumptions are revisited.

2.2 Methods

2.2.1 Analytical calculations

In order to infer any information about the input from the output of the neuron, we must have a model of the input/output transformation. In this chapter we use a passive, leaky integrate and fire (LIF) model. Such a model assumes the neuron is composed of a single electrotonically compact compartment with the capacitance C and receives

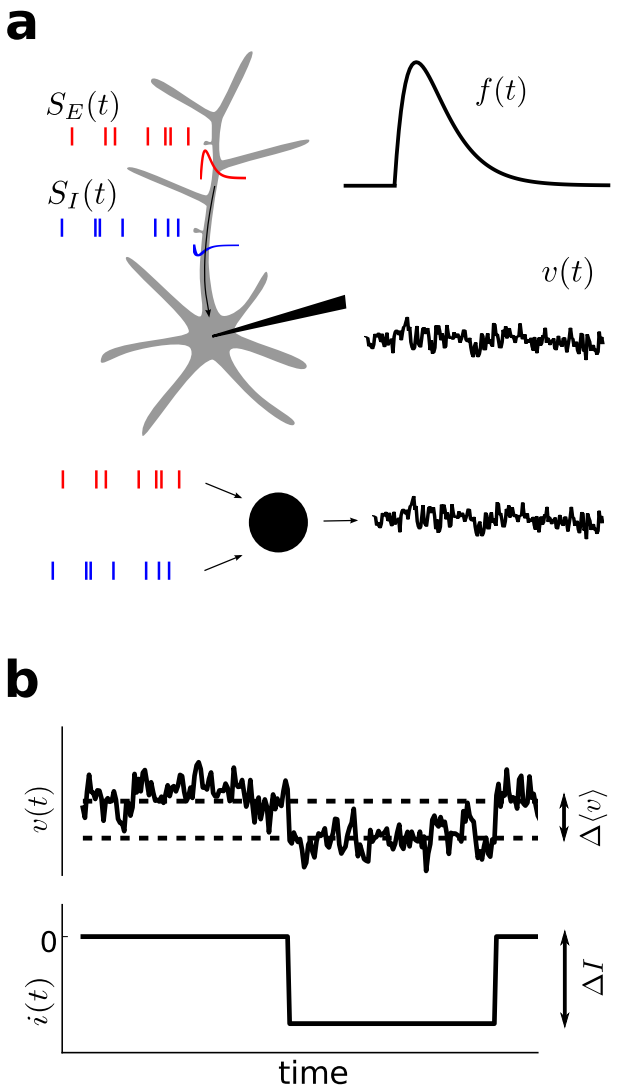

Figure 2.1: **(a)** The excitatory and inhibitory input spike trains ($S_E(t)$ and $S_I(t)$ respectively) are causing changes in the membrane voltage $v(t)$ of the neuron (top-left). We estimated the statistics of those inputs based on the measured statistics of the membrane voltage using a passive model of an electrotonically compact single-compartment cell (bottom). We assumed each presynaptic spike induces a change in the membrane conductance with time course $f(t)$ (α function, equation 2.14), scaled by different amplitudes (top-right). **(b)** The membrane conductance is measured by injecting a static hyperpolarizing current ΔI into the cell through the measurement pipette and observing the average deflection in the membrane potential $\Delta\langle v\rangle$.

as its input excitatory and inhibitory conductance changes ($g_E(t)$ and $g_I(t)$). The two input types have associated reversal potentials (V_E and V_I) which differ in their behavior. Excitatory inputs cause depolarization of the neuron's membrane potential ($v(t)$), whereas inhibitory inputs typically induce hyper-polarization. The dynamics of the membrane potential in such a system are described by the equation:

$$C\frac{dv(t)}{dt} = G_L(V_L - v(t)) + g_E(t)(V_E - v(t)) + g_I(t)(V_I - v(t)) + i(t), \tag{2.1}$$

where G_L and V_L are the intrinsic membrane conductance and membrane reversal potential in the absence of synaptic input, and $i(t)$ is the current input. The input is normally zero unless a current is injected into the cell through the measuring pipette (see next section).

Once the membrane voltage reaches the threshold value, the neuron emits an action potential. Since this is a relatively rare event relative to the duration of the measurement we do not include it in the analytical calculations (but see [35] for the possible misestimation in the cases of high firing rate).

First order statistics

To calculate the first order statistics of the input synaptic conductances, we consider the stationary case ($dv/dt = 0$) of equation (2.1):

$$0 = G_L(V_L - \langle v\rangle) + \langle g_E\rangle(V_E - \langle v\rangle) + \langle g_I\rangle(V_I - \langle v\rangle), \tag{2.2}$$

where the angle brackets denote an average over time, defined as

$$\langle x\rangle = \lim_{T\to\infty}\frac{1}{T}\int_0^T x(t)dt. \tag{2.3}$$

To estimate $\langle g_E\rangle$ and $\langle g_I\rangle$ *in vivo,* we use the measurements from the membrane conductance $\langle g\rangle$ and the mean voltage $\langle v\rangle$ for two cases: (1) *in vitro* with blocked synaptic inputs; (2) *in vivo* with the synaptic input present. The measurements are performed using the intracellular recording technique, where the membrane voltage is measured at the soma. To measure the membrane conductance, a current ($i(t)$ in equation 2.1) is injected into the cell and the conductance is estimated from the relationship between the injected current ΔI and the membrane voltage deflection $\Delta\langle v\rangle$ ($\langle g\rangle = \Delta I/\Delta\langle v\rangle$).

For the *in vitro* case expression (2.2) is simplified ($\langle g_E\rangle = \langle g_I\rangle = 0$) and mean total membrane conductance $\langle g\rangle$ and mean voltage $\langle v\rangle$ are

$$\langle g\rangle_1 = G_L, \quad \langle v\rangle_1 = V_L, \tag{2.4}$$

where subscript 1 (2) describes *in vitro (in vivo)* case. For the *in vivo* case with the non-zero input conductances we get

$$\langle g\rangle_2 = G_L + \langle g_E\rangle + \langle g_I\rangle, \quad \langle v\rangle_2 = \frac{G_L V_L + \langle g_E\rangle V_E + \langle g_I\rangle V_I}{G_L + \langle g_E\rangle + \langle g_I\rangle}. \tag{2.5}$$

Denoting the changes between the *in vitro* and *in vivo* cases as $\Delta\langle v\rangle = \langle v\rangle_2 - \langle v\rangle_1$ and $\Delta\langle g\rangle = \langle g\rangle_2 - \langle g\rangle_1$ we can write the expression for the input excitatory and inhibitory conductances as

$$\langle g_E\rangle = \frac{\Delta\langle v\rangle(G_L + \Delta\langle g\rangle) - \Delta\langle g\rangle(V_I - V_L)}{V_E - V_I}, \tag{2.6}$$

$$\langle g_I\rangle = \frac{\Delta\langle v\rangle(G_L + \Delta\langle g\rangle) - \Delta\langle g\rangle(V_E - V_L)}{V_I - V_E}. \tag{2.7}$$

Second-order statistics

Knowing the statistics of the synaptic inputs, we can analytically compute the power spectral density of the membrane potential by adopting some assumptions regarding the shape and the statistics of the inputs. Let $S_p(t) = \sum_{k_p} \delta(t - t_{k_p})$ be the train of presynaptic action potentials from the presynaptic neuron p firing at the times t_{k_p}

The time course of the conductance change caused by the inputs can then be written as a convolution of the action potential train with the conductance kernel

$$g(t) = \sum_p \int_{-\infty}^{\infty} B_p f_p(s) S_p(t-s)\, ds, \tag{2.8}$$

where $f_p(s)$ is the time course of the conductance change caused by a single action potential of the presynaptic neuron p, and B_p is the amplitude of the conductance change which can be a random value from a log-normal distribution [36] (as we see later the exact distribution is not important for our method). Here we assume a stable response to a presynaptic firing – the size of the postsynaptic potential caused by the specific presynaptic neuron is constant in time. The time courses of the excitatory and inhibitory conductance changes $f_p(s)$ are different due to the difference in the dynamics of the channel properties for each type of the inputs. If we further assume all excitatory conductances have the same time course $f_E(s)$, and similarly all the inhibitory inputs have the same time course $f_I(s)$ we can split the equation 2.8 into two parts:

$$g_x(t) = \sum_{p_x} \int_{-\infty}^{\infty} B_{p_x} f_x(s) S_{p_x}(t-s)\, ds$$
$$g(t) = g_E(t) + g_I(t),$$

where we substitute x with E or I for the case of excitatory or inhibitory inputs respectively. We will use this notation throughout the rest of the section.

To compute the power spectral densify, we first note that the Fourier transfer of the convolution of two functions is a product of the individual Fourier transforms of those functions

$$\tilde{g}_x(\omega) = \sum_{p_x} B_{p_x} \tilde{f}_x(\omega) \tilde{S}_{p_x}(\omega), \tag{2.9}$$

where the Fourier transform $\tilde{x}(\omega)$ of a function $x(t)$ is a transformation from the time domain, t, to the frequency domain, ω, defined as

$$\tilde{x}(\omega) = \int_{-\infty}^{\infty} x(t) e^{-i\omega t} dt.$$

The power spectral density is defined as the square of the Fourier transform

$$P_x(\omega) \equiv 2\tilde{x}^*(\omega)\tilde{x}(\omega) \tag{2.10}$$

where x^* indicates the conjugate of the complex value x. Inserting expression (2.9) into the definition (2.10) gives us the power spectral density of the conductance.

$$\begin{aligned} P_{g_x}(\omega) &= 2 \left(\sum_{p_x} B_{p_x} \tilde{f}_x(\omega) \tilde{S}_{p_x}(\omega) \right)^* \left(\sum_{p_x} B_{p_x} \tilde{f}_x(\omega) \tilde{S}_{p_x}(\omega) \right) \\ &= 2|\tilde{f}_x^2(\omega)| \left(\sum_{p_x} B_{p_x} \tilde{S}_{p_x}(\omega) \right)^* \left(\sum_{p_x} B_{p_x} \tilde{S}_{p_x}(\omega) \right) \\ &= 2|\tilde{f}_x^2(\omega)| N_x E\left[|\tilde{S}_x^2(\omega)| \right] E\left[B_x^2 \right]. \end{aligned} \tag{2.11}$$

Here, N_x is the total number of input trains contributing to the conductance. In the last step we summarize the average over all the trains - E[.] to denote the expected value. To do so we first assumed the input trains are uncorrelated ($\langle \tilde{S}_{p_x}^*(\omega)\, \tilde{S}_{r_x}(\omega) \rangle = 0, \forall p_x \neq r_x$) and then assumed the power spectra of an input train is uncorrelated with the amplitude of the individual conductance change for that presynaptic neuron.

We can expand 2.11 further by noting that $E[B_x^2] = E[B_x]^2 + \sigma_{B_x}^2$, with $E[B_{p_x}]$ and $\sigma_{B_{p_x}}$ being the mean and standard deviation of the probability distributions of the amplitudes. For a spike train generated by a Poisson process, the power spectra is simply $|\tilde{S}_{p_x}^2(\omega)| = \lambda_{p_x} + 2\pi\lambda_{p_x}^2\delta(\omega)$, where λ_{p_x} is the firing rate of the neuron p_x. For all the non-zero frequencies we can write 2.11 as

$$P_{g_x}(\omega) = 2|\tilde{f}_x^2(\omega)|N_{p_x}E[\lambda_x](E[B_x]^2 + \sigma_{B_x}^2).$$

To obtain the power spectra of the synaptic currents, $P_{I_x}(\omega)$, we multiply the power spectra of the conductances with the square of the driving voltage:

$$P_{I_x}(\omega) = P_{g_x}(\omega)(V_x - \langle v \rangle)^2.$$

Here we assume that the membrane voltage fluctuations are small compared to the driving voltage and thus keep the driving voltage stationary.

To get the power spectra of the total current ($I = I_E + I_I$), we need to sum the contributions of the excitatory and inhibitory currents

$$P_I(\omega) = 2\tilde{I}^*\tilde{I} = 2\,(\tilde{I}_E + \tilde{I}_I)^*(\tilde{I}_E + \tilde{I}_I) = P_{I_E}(\omega) + P_{I_I}(\omega) + P_{I_{IE}}(\omega) + P_{I_{EI}}(\omega),$$

where we define the cross-spectra

$$P_{I_{EI}}(\omega) \equiv 2\tilde{I}_E^*\tilde{I}_I = 2\left(\sum_{p_E} B_{p_E}\tilde{f}_E(\omega)\tilde{S}_{p_E}(\omega)\right)^*\left(\sum_{p_I} B_{p_I}\tilde{f}_I(\omega)\tilde{S}_{p_I}(\omega)\right)(V_E - \langle v \rangle)^*(V_I - \langle v \rangle),$$

and similar for $P_{I_{IE}}$. As before, we assume the excitation and inhibition are uncorrelated ($\langle \tilde{S}_{p_E}^*(\omega)\tilde{S}_{p_I}(\omega)\rangle = 0, \forall(p_E, p_I)$) and thus the cross-spectra terms $P_{I_{EI}}$ and $P_{I_{IE}}$ are zero.

Finally, to get the power spectrum of the membrane voltage we have to take into the account the membrane filtering, which in our model is simply a linear low-pass filter

$$Z(\omega) = \frac{R_{\text{eff}}}{1 + i\omega\tau_{\text{eff}}}, \tag{2.12}$$

where $R_{\text{eff}} = 1/(G_L + \langle g_e \rangle + \langle g_i \rangle)$ and $\tau_{\text{eff}} = C/(G_L + \langle g_e \rangle + \langle g_i \rangle)$.

We can write the full expression for the power spectrum of the membrane voltage under our assumptions as

$$\begin{aligned}|P(\omega) =& |Z(\omega)|^2(P_{I_E}(\omega)+P_{I_I}(\omega)) \\ =& 2|\tilde{f}_E^2(\omega)|N_{p_E}E[\lambda_E](E[B_E]^2+\sigma_{B_E}^2)|Z(\omega)|^2 \\ &+2|\tilde{f}_I^2(\omega)|N_{p_I}E[\lambda_I](E[B_I]^2+\sigma_{B_I}^2)|Z(\omega)|^2,\end{aligned} \tag{2.13}$$

where we took into account that $P_v(\omega) = |Z(\omega)|^2 P_I(\omega)$.

We approximate the time course of the conductance change resulting from a single input event as an α function [8],

$$f_x(t) = \frac{t}{\tau_x} e^{(1-t/\tau_x)} H(t), \tag{2.14}$$

where $H(t)$ is the Heaviside step function. The Fourier transform of the alpha function gives

$$|f_x(\omega)^2| = \frac{e\tau_x}{1+\omega^2\tau_x^2}. \tag{2.15}$$

The average total conductances for this shape of the pulse are

$$\begin{aligned}\langle g_E\rangle &= \sum_{p_E} B_{p_E}\lambda_{p_E}\int f_E(t)dt = eN_E E[\lambda_E]E[B_E]\tau_E, \\ \langle g_I\rangle &= \sum_{p_I} B_{p_I}\lambda_{p_I}\int f_I(t)dt = eN_I E[\lambda_I]E[B_I]\tau_I.\end{aligned} \tag{2.16}$$

Given our experimental observations, we have no way of estimating the number of inputs and their frequencies, i.e. N_x and $E[\lambda_x]$ separately. Instead we estimate the net-total exponential and inhibitory firing rate $\hat{\lambda}_x = N_x E[\lambda_x]$.

In the above calculations we keep the amplitude of the conductance change events following a presynaptic spike fixed for each of the presynaptic neurons. While we would not expect any changes of the amplitudes caused by longer term plasticity changes on the timescales of our recordings (less than an hour), the synaptic strength might be influenced by short term plasticity, which can both decrease or increase the amplitude of the conductance changes.

2.2.2 Simulations

We performed the simulations with the Brian simulator [37] using the conductance-based leaky integrate and fire (LIF) model with the adaptive threshold adopted from

[32]. Given the presynaptic firing times and their strengths (input) the simulator integrates the membrane voltage dynamics according to equation 2.1, where the excitatory and inhibitory conductances are a sum of the input spike trains convolved with the α-function kernel (equation 2.14). To get the comparable amount of repetitions to the data we did 10 simulations of 20 seconds of activity for each case, using randomized inputs described below.

Spiking threshold

The neuron elicits a spike at every time it crosses the threshold voltage, $\theta(t)$, but unlike the conventional LIF models it does not reset the membrane voltage. Instead it adopts the threshold value with the dynamics given by

$$\begin{aligned}\theta(t) =& \hat{\theta} + \sum_j K(t - t_j),\\ K(t) =& \Delta\theta\, e^{-t/\tau_\theta} H(t).\end{aligned}$$

Every time, t_j, a spike is elicited the threshold value is increased by $\Delta\theta$ and then exponentially decays with the time constant τ_θ towards the base value $\hat{\theta}$. After the spike, the neuron is prevented from spiking again during the refractory period with duration τ_{ref}. This type of model has not only been shown to be a good model for predicting the timing of the action potentials [34, 12], but also avoids the possible contamination of the power spectral density introduced by resetting the membrane voltage.

The parameters for the threshold dynamics were fitted by hand to match the observed firing rates from the recordings and are listed along with other default values for the model in table 2.1.

$C[pF]$	$G_L[nS]$	$V_L[mV]$	$V_E[mV]$	$V_I[mV]$	$\hat{\theta}[mV]$	$\tau_\theta[ms]$	$\Delta\theta[mV]$	$\tau_{\text{ref}}[ms]$
100	5.55 [38]	-62 [39]	0	-75	-44.5	10	2	2

Table 2.1: Table of neuronal model parameters.

Modulations of the firing frequency of inputs

For the modulations of the input firing rate, $\lambda_x(t)$, we use the combination of sinusoidal and Ornstein-Uhlenbeck (OU) processes [40] defined as

$$\begin{aligned}\lambda_x(t) =& \hat{\lambda}_x \left(1 + \frac{\alpha_x}{2} A(t) + \frac{\beta_x}{2} B(t)\right), \\ A(t) =& \sin\left(2\pi\left(\omega t + \mathrm{OU}(\tau_{\mathrm{OUsin}}, \sigma_{\mathrm{OUsin}})\right)\right), \\ B(t) =& \mathrm{OU}(\tau_{\mathrm{OUinp}}, 1),\end{aligned} \tag{2.17}$$

where the parameters α_x and β_x control the proportion of the sinusoidal and OU processes respectively and ω is a frequency of the sinusoidal process whose phase is modulated by a separate OU process. OU process [40] is a stochastic process satisfying the stochastic differential equation

$$dx_t = \frac{\mu - x_t}{\tau_{\mathrm{OU}}} dt + \kappa dW,$$

where dW denotes a Weiner process also known as the standard Brownian motion. We set $\mu = 0$ and chose κ such that we get the desired standard deviation of the OU process σ_{OU}, where

$$\sigma_{\mathrm{OU}}^2 = \kappa^2 \tau_{\mathrm{OU}}/2.$$

After some time ($T \gg \max(\tau_{\mathrm{OUinp}}, 1/\omega)$) the added fluctuations will average out and the mean input firing rates will not be changed.

2.2.2.1 Correlated spike trains

Correlated spike trains were created by first generating k independent discretised spike trains with a desired firing frequency modulation. For each time step of a correlated spike train, S, we randomly chose one of the k spike trains and copy its spiking value. The pairwise correlation (Pearson correlation coefficient) between the spike trains S_1 and S_2 in this case is

$$r_P(S_1, S_2) = \frac{\mathrm{cov}(S_1, S_2)}{\sigma_{S_1} \sigma_{S_2}} = \frac{\langle (S_1 - \langle S_1 \rangle)(S_2 - \langle S_2 \rangle) \rangle}{\sqrt{\langle (S_1 - \langle S_1 \rangle)^2 \rangle} \sqrt{\langle (S_2 - \langle S_2 \rangle)^2 \rangle}} = \frac{1}{k}.$$

2.2.3 Data analysis

2.2.3.1 Power spectral density

Analysis of the membrane voltage dynamics v was performed after clipping spikes from threshold to 3 ms after the peak. The spike threshold was defined as the maximum

of the second derivative of the voltage trace [41]. We computed the power spectral density of v with 75% overlapping triangular (Bartlett) 1 s windows.

2.2.3.2 Compound synaptic events

We were unable to isolate single synaptic events from the data. Instead we defined and *ad hoc* a measure we named compound synaptic events, by looking for an increase of the membrane voltage occurring in a time window shorter than the average membrane time constant (5 ms) and with a minimal detection threshold of 1 mV (Fig. 2.8b). Events that occurred within ± 10 ms of a spike were discarded from the analysis. This measure captures the frequencies of the fast changes of the membrane voltage most likely caused by a simultaneous occurrence of excitatory inputs not balanced by the inhibitory inputs. This measure was not directly used for the input estimation.

2.3 Application of the input estimation method

The input estimation is composed of two main steps. In the first step, we estimate the mean input excitatory and inhibitory conductances (or the conductance changes between two states) through the observations of the mean membrane voltage and the mean input conductance changes between the two states. In the second step, we take the second-order statistics and use the power spectrum density of membrane voltage to estimate the input sizes and following this the input frequencies. We assume the temporal structure of the inputs (Poisson train) and the shape of the inputs (α-function, equation 2.14) with specific time constants. The following section describes the method in more details through a concrete example.

2.3.1 The two states of activity in the motor cortex (data)

We applied the estimation method on whole-cell patch-clamp recordings of layer 5B neurons in the motor cortex of awake, behaving mice. The mice are positioned on a top of a cylindrical tread-mill in either quiet wakefulness or in voluntary movement (grooming, walking or running). During periods of forelimb inactivity, all layer 5B pyramidal neurons displayed large-amplitude membrane potential fluctuations and a moderate firing rate at about 5 Hz. During movement, layer 5B pyramidal neurons displayed diverse changes in firing rate. For further analysis we split neurons into two

groups based on whether spike output was suppressed ($L5B_{supp}$) or enhanced ($L5B_{enh}$) during movement (Figure 2.2).

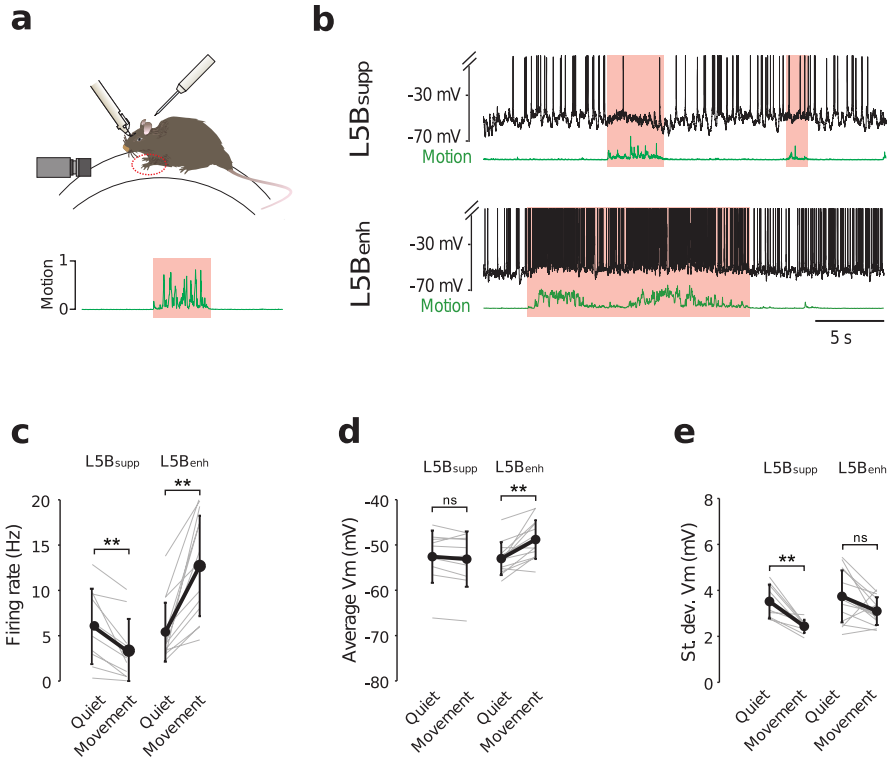

Figure 2.2: The two states of activity in the motor cortex **(a)** The recording configuration with the mouse positioned on a cylindrical treadmill. The animal's movement was recorded using a high frame-rate digital camera (top). The motion index was calculated offline and was used to identify periods of quiet and periods of voluntary movement (bottom). **(b)** Example traces of membrane voltage recordings for a neuron which decreases its firing rate during the movement (top) and a neuron which increases its firing rate during movement (bottom). **(c-e)** Average firing rate (c), average membrane voltage (d) and standard deviation of the membrane voltage (e) for the recorded cells in the quiet state and during movement. The cells are split according to whether their activity is suppressed during movement ($L5B_{supp}$) or enhanced ($L5B_{enh}$).

As there was no significant difference between the two groups in the quiet case, for the purpose of modeling we pooled this data.

2.3.2 Fitting the model

Given the observed differences in the activity among the two groups of neurons, we asked what the possible changes in the inputs are which give rise to those differences.

To do this we used a combination of analytical calculations and numerical simulations (see 2.2.1 and 2.2.2) to estimate the statistics of the inputs to the soma for the three groups (quiet, moving-suppressed, moving-enhanced).

In the section 2.2.1, we described a general method for input estimation that would involve two steps. Here we found a simple Poisson train model of the inputs is too simple and does not explain the observed dynamics, so we added an extra step to counter this.

The estimation used to fit the model involves three steps:

1. Calculation of the mean total levels of excitatory and inhibitory conductances.
2. Estimation of the average sizes and the frequency of the events at the soma.
3. Adjusting the input timing statistics (the added step).

1. Calculation of mean total conductance levels

The higher average membrane voltage in the $L5_{supp}$ cells during movement (Figure 2.2) could be caused by an increase of the excitation, decrease of the inhibition or the combination of the two. To distinguish between those options we first estimated the excitatory and inhibitory conductance averaged over time ($\langle g_e \rangle$ and $\langle g_i \rangle$) using the estimation method described in 2.2.1.

To demonstrate the method we first applied it to surrogate data (Figure 2.3). For each estimation we created two simulations, one without and one with the synaptic inputs. For the simulation with the synaptic conductances we insert the conductance-based excitatory and inhibitory inputs as a Poisson input train (2.14) with the α-function kernel (2.14). We recorded the mean membrane potential, $\langle v \rangle_1$ and $\langle v \rangle_2$, and mean membrane conductances, $\langle g \rangle_1$ and $\langle g \rangle_2$, which allow us to estimate $\langle g_e \rangle$ and $\langle g_i \rangle$ using equations 2.6 and 2.7. In all the simulations the spiking neuron was blocked from spiking. To obtain the mean membrane conductances $\langle g \rangle_1$ and $\langle g \rangle_2$ we used a depolarizing DC current injection and measured the mean membrane voltages before and after the current injection in each case.

In Figure 2.3 we compare the estimated values of the synaptic conductances using the recorded values of mean membrane voltages and conductances with the actual synaptic conductances recorded directly in the simulations and find there is a very good agreement.

Next, we applied the method to the measurements from the *in vivo* recordings, where we recorded the mean voltages and input conductances while the neuron is

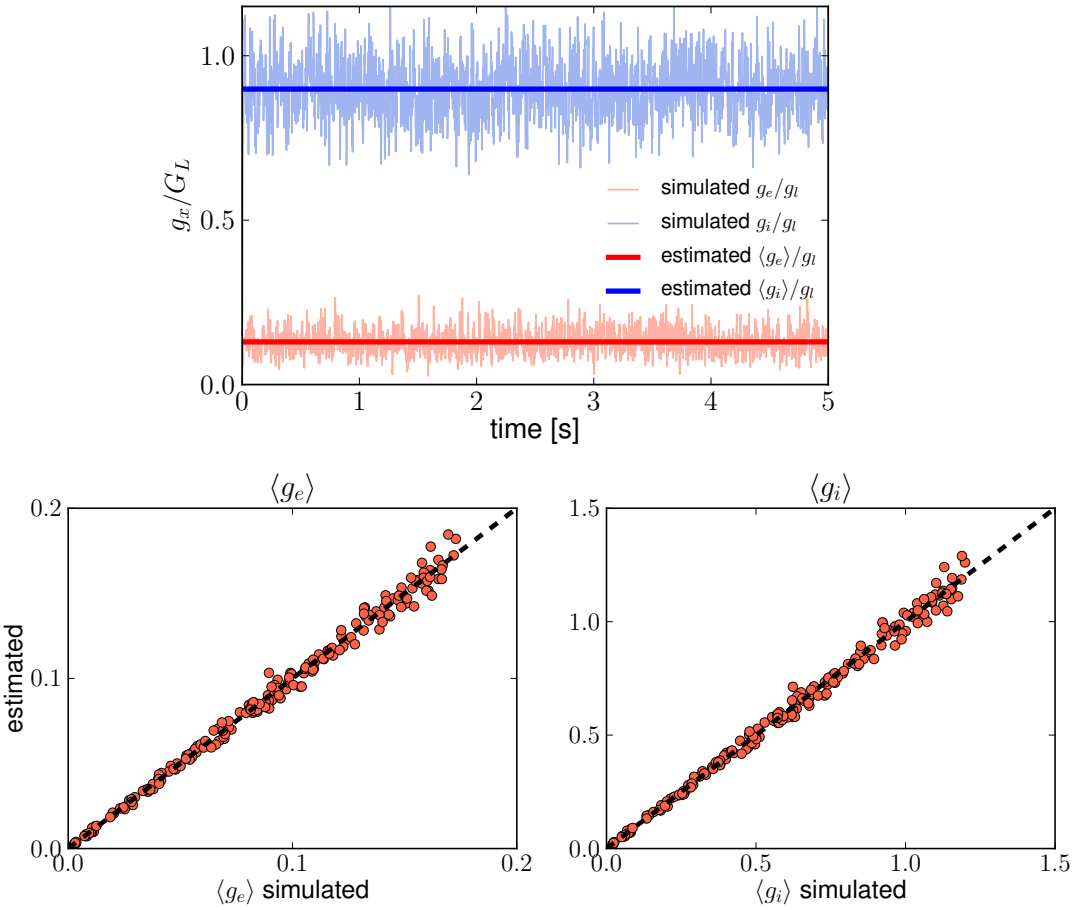

Figure 2.3: (top) An example of average input conductance estimations in a passive single compartment model. The thin lines represent the time course of the simulated input conductances (red for excitatory, blue for inhibitory). The thick lines represents the estimated average values of the excitation and inhibition.
(bottom) Comparing the actual simulation values (points) with the estimated mean (line) of the excitatory (left) and inhibitory (right) conductances.

exposed to the synaptic input. For the values when the presynaptic neurons are silent we took the input conductance and leak reversal potential values from the *in vitro* studies reported in the literature [38, 39]. Note that in contrast with the estimation of absolute input conductances the comparison between two *in vivo* states is independent of those values.

Figure 2.4 shows the results of the estimation. During quiet wakefulness we estimated $\langle g_e \rangle$ and $\langle g_i \rangle$ to be 2.2 and 3.0 nS, respectively similar to the values measured in primary visual cortex of awake mice [27]. During movement, the $L5B_{supp}$ neurons received a moderate increase in inhibition ($\Delta g_e = 0.0$ nS, $\Delta g_i = 0.4$ nS), while the $L5B_{enh}$ neurons received a moderate increase in excitation ($\Delta g_e = 0.7$ nS, $\Delta g_i = 0.1$ nS). The increase of the average membrane voltage in $L5B_{enh}$ cells is thus primarily caused by the net increase in excitation.

2. Estimation of the average event size and frequency

To estimate the average sizes of the events seen at the soma, B_X, and the firing rates, λ_x, we used the method described in subsection 2.2.1, which relies on the second-order statistics of membrane voltage—more specifically on its power spectral density. Figure 2.5 shows how the analytical calculations (2.13) fit with the simulated surrogate data. Note the deviations from the analytically calculated values at low frequencies—this is due to the probabilistic nature of the spike trains (in the case of simulation a pure Poisson process). The number of total wavelengths within a limited time sample is inversely proportional to the frequency and thus our "sample size" for lower frequencies is smaller.

When using the data from the recordings, we fit the model to the power spectral density of the recorded output in the δ frequency band (range between 15 and 30 Hz) which avoids the slow fluctuations. We set the synaptic time constants to τ_E = 2ms and τ_I = 10ms [42], while $\langle B_E \rangle = \langle B_I \rangle$ [43, 44]. We further set the ratio $\sigma_{B_E}/\langle B_E \rangle = 1.3$ (extracted from [45]) and $\sigma_{B_I}/\langle B_I \rangle = 1$ for all cases. We could then estimate the values of $\langle B_x \rangle$ and λ_x for all cases according to expression (2.13).

During the fitting process, we assumed the conductance change amplitude B_x corresponding to a specific presynaptic neuron does not change with time, and that the distribution of amplitudes did not change between the two behavioral states. As mentioned in subsection 2.2.1 short-term plasticity effects would violate the first assumption. Additionally, neuromodulation could change the distribution of the amplitudes between the two states, violating the second assumption.

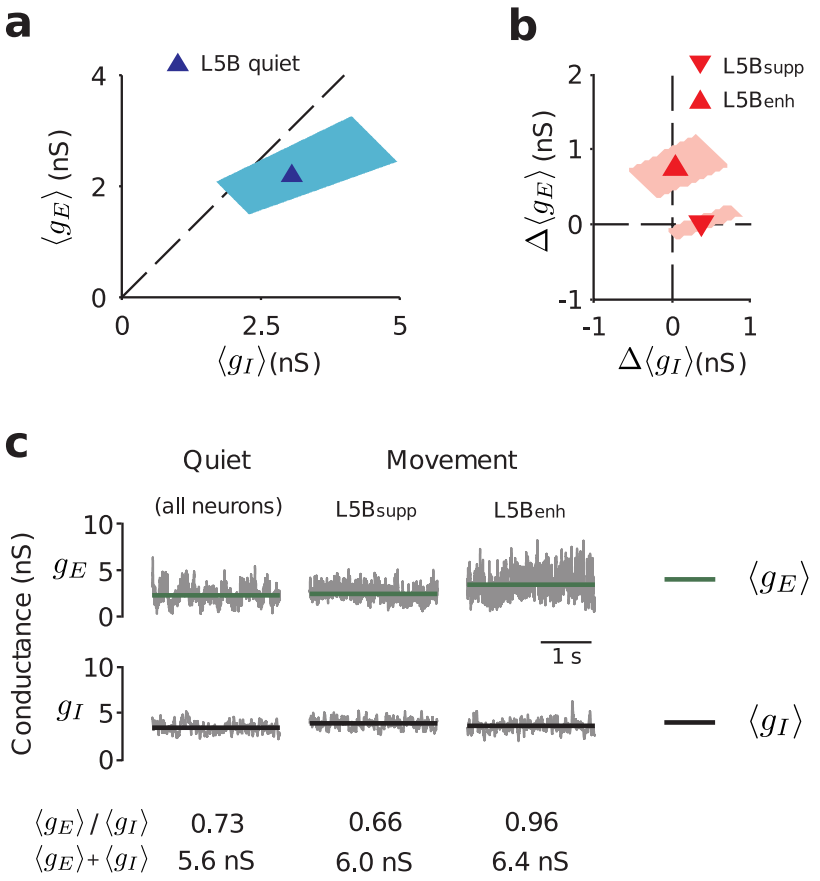

Figure 2.4: Mean conductance estimations **(a)** Average excitatory and inhibitory conductance during quiet wakefulness (n=24). The dashed line represents unity. The shaded region represents the 95% confidence interval. Each corner of the rectangle is calculated by using the values of the membrane voltage and input resistance measurements (Eq. 2.6 and 2.7) corresponding to the borders of the interval which includes the 95% of the measured traces (2-sigma assuming independent normal distributions of membrane voltage and input resistance). **(b)** Average changes in excitatory (Δg_E) and inhibitory (Δg_I) conductance in $L5B_{supp}$ (downward triangle, n = 10) and $L5B_{enh}$ (upward triangle, n = 14) pyramidal neurons during movement. **(c)** Representative traces for the total excitatory (top) and inhibitory (bottom) conductances. The traces were simulated using the model with the parameters obtained from the data.

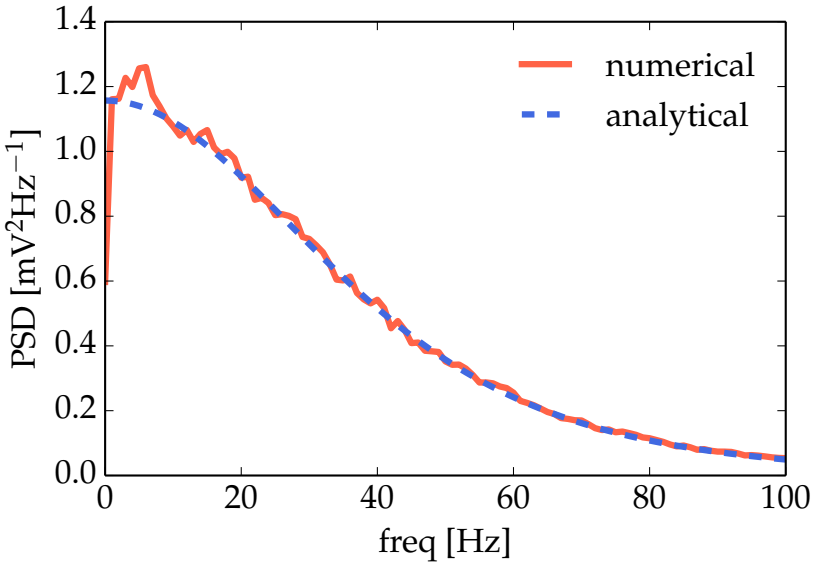

Figure 2.5: Comparison between the analytically computed and the simulated power spectral density of the membrane voltage. We simulated a membrane voltage dynamics for 500s during which the neuron was exposed to excitatory and inhibitory firing rates of 1000 Hz.

We fit the power spectral density for all three cases $C = \{L5B_{quiet}, L5B_{enh}, L5B_{supp}\}$ simultaneously, choosing a value of $\langle B_x \rangle$ (the same for each case) which minimizes the total estimation error Er (sum of squares error) within the frequency band used for fitting, summed over all the three cases (15-30 Hz)

$$B_x = argmin(Er(B_x)) = argmin(\sum_C \sum_\omega (PSD_{experimental}(\omega) - PSD_{analytical}(\omega, B_x))^2),$$

where ω is discretized frequency on the interval between 15 and 30 Hz and $PSD_{analytical}$ is the analytical calculation of the power spectral density given in equation (2.13). The optimization was done by simply finding a minimum of Er value for an array of equidistant values B_x around the global minimum (we have a simple convex optimization problem).

The estimated event rates given a $\langle B_x \rangle$ can be calculated as $\lambda_x = \langle g_x \rangle / (\langle B_x \rangle \tau_x e)$ (see Equation 2.16) specifically for each case. Note that the event rates λ_x are required to calculate the analytical PSD.

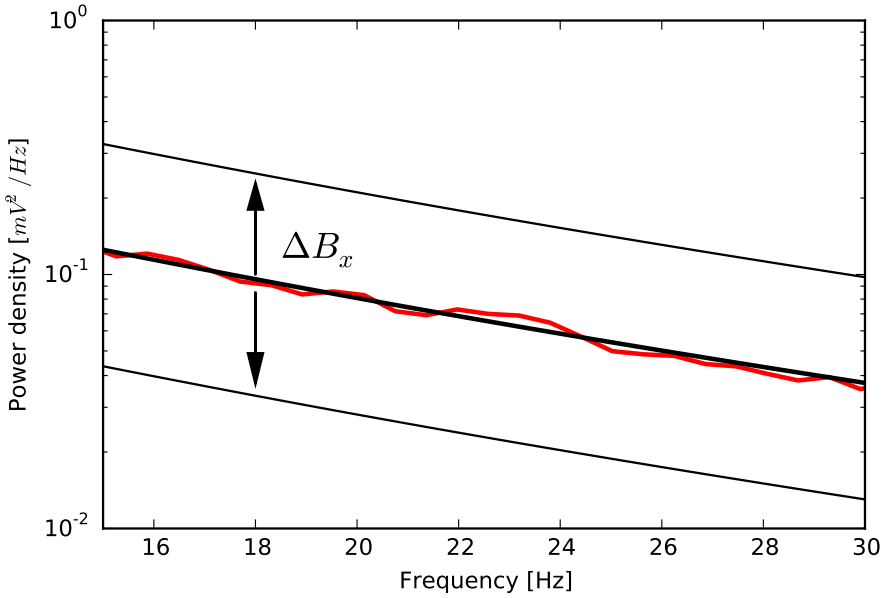

Figure 2.6: **Estimation of the event sizes:** Changing the average size of the input events at the soma modulates the PSD of the membrane voltage as expressed in the equation (2.13). Assuming the time constants of the events, equal mean event sizes for excitation and inhibition ($B_E = B_I \equiv B_x$) and a stable coefficient of variation of the event size distribution ($\sigma_{B_x}/\langle B_x \rangle$), we estimate the mean event size B_x by minimizing the difference (least square error) between the analytically calculated PSD (black line) and the measured PSD (red line) in the interval between 15 and 30 Hz.

3. Adjusting the input timing statistics

In the final step, we look at the changes of the power spectral density at the lower frequencies. Cortical state changes have been shown to regulate slow membrane fluctuations in layer 2/3 neurons in the awake cortex. We noticed a similar phenomena in the layer 5B cells of the motor cortex. Specifically we observed slow (1.5–4 Hz) amplitude fluctuations (Figure 2.8a).

These fluctuations are most likely caused by the temporal structure of the input such as slow time variations of the mean firing rates. To show this, we set the firing patterns of the input trains as a Poisson process with the mean rate, λ_x, modulated in time by sinusoidal and Ornstein-Uhlenbeck (OU) processes as described in the methods section 2.2.2.

2.3.3 Correlations in input spike trains

In the second step of the input estimation we noticed the differences in the PSD in the δ band (15 to 30 Hz) between the three cases were bigger than what could be expected from the differences in the estimated mean excitatory and inhibitory conductances. Specifically the $L5B_{enh}$ case has a 2-fold increase in the δ band compared to the quiet wakefulness state $L5B_{quiet}$ (figure 2.7). Only about half of that PSD increase can be explained by the increased excitatory input rates, which we predict from the increased total input excitatory conductance in the previous step (Figure 2.4).

One possible explanation of this effect is a change in the input timing statistics. For example if the input spike trains are correlated, the Fourier transform of the autocorrelation of the spike train (Wiener–Khinchin theorem) would change ($E[|\tilde{S}_x^2(\omega)|]$ in equation 2.11) increasing the PSD. For a more intuitive explanation of the effect we can imagine a difference in the PSD between two independent Poisson input spike trains versus the PSD between two perfectly correlated Poisson input spike trains all with the firing frequency $\lambda = \hat{\lambda}$ and an amplitude of conductance change $B = \hat{B}$. If we collapse the two spike trains into one, we get a process with an amplitude $B = \hat{B}$ and firing rate $2\hat{\lambda}$ for the case of uncorrelated trains and a process with the amplitude $B = 2\hat{B}$ and firing rate $\lambda = \hat{\lambda}$ for the case of the correlated trains. From the equation (2.11) we can write $PSD = \alpha B^2 \lambda$ and thus for the uncorrelated case we get $PSD_{uncorr} = 2\alpha\hat{B}^2\hat{\lambda}$ and for the correlated case $PSD_{corr} = 4\alpha\hat{B}^2\hat{\lambda}$. The PSD of the fully correlated input trains is thus twice as big as the uncorrelated input trains. Following the same line of reasoning it is easy to see that for N neurons the PSD is N times bigger.

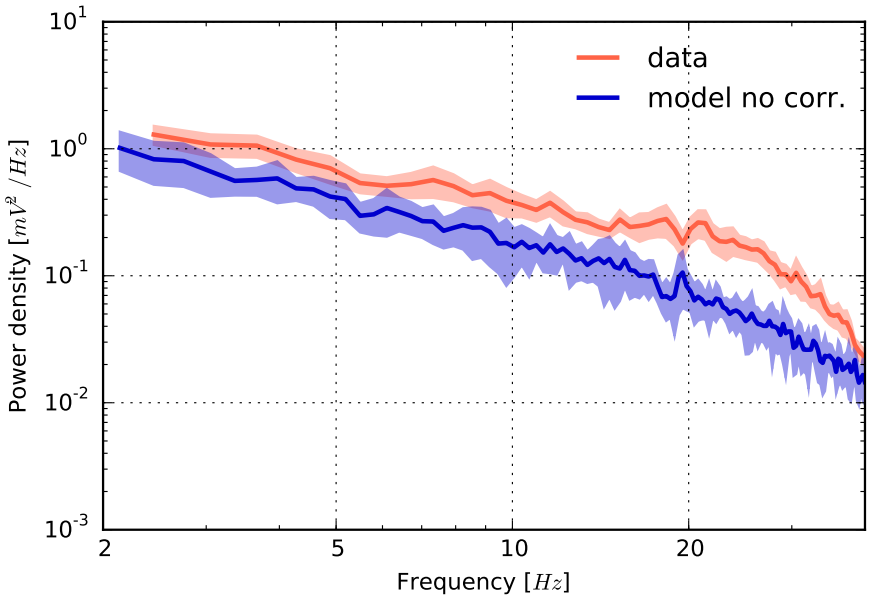

Figure 2.7: The misfit of the power spectral density between the recorded data and model without instantaneous correlations for the $L5B_{enh}$. To get the data for the model PSD we do 10 simulations of 20 seconds of the membrane voltage fluctuations. The lines correspond to the averaged PSD over the trials and the shaded area to 1 standard deviation from the average.

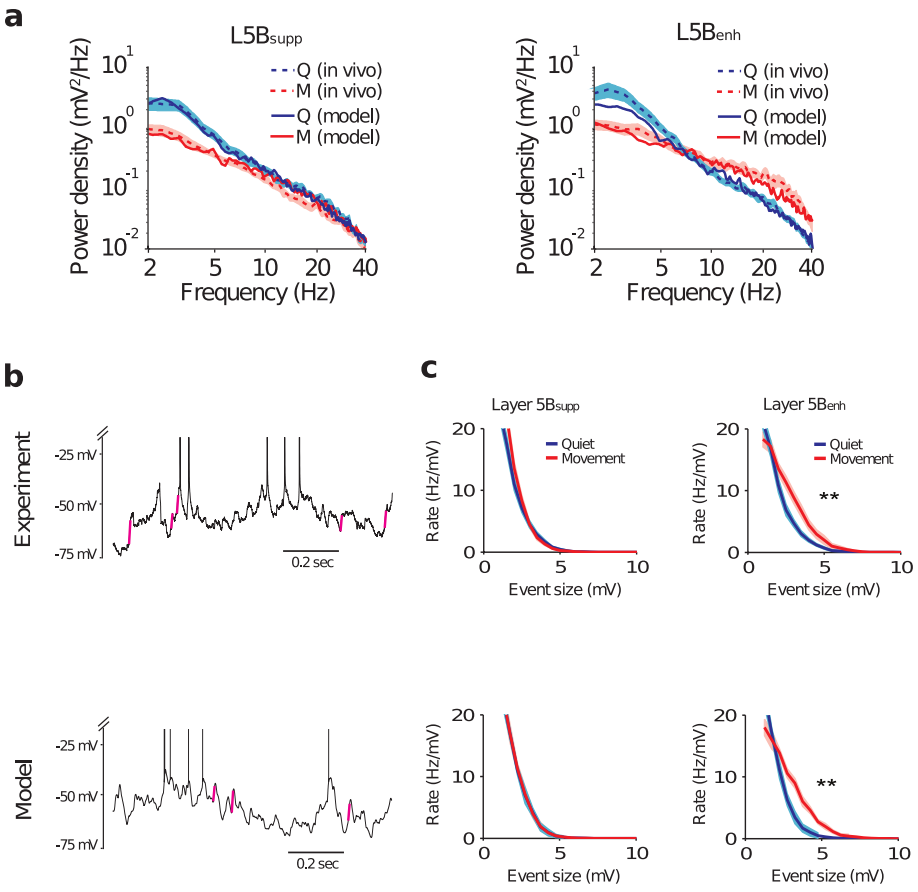

Figure 2.8: Fitting the model to the power spectral densities. **(a)** The measured power spectral densities of the membrane voltage fluctuations for the two groups (dashed lines) and the final model predictions (solid lines). **(b)** Representative voltage traces from an *in vivo* recording (upper panel) and model simulation (lower panel) of a $L5B_{enh}$ pyramidal neuron. For display purposes only compound synaptic events with amplitudes > 4 mV and rise-times < 5ms are highlighted in magenta. **(c)** The added correlations in the case of $L5B_{enh}$ during movement (red) can also explain the difference in the frequency of compound synaptic events compared to the state of quiet wakefulness (blue).

We tried to improve the model fit by adding correlations. Correlated input spike trains were generated with the process described in the methods (2.2.2). Adding the correlations to the excitatory subpopulation of the $L5B_{enh}$ case ($k = 325$, $r_{S_1,S_2} = 0.003$) was sufficient to reproduce the PSDs (Figure 2.8a).

Additionally the addition of correlations correctly predicted the frequency of the compound synaptic events defined in 2.2.3.2 (figure 2.8c).

Finally we obtain the parameter values presented in Table 2.2.

	$L5B_{quiet}$	$L5B_{enh}$	$L5B_{supp}$
$\hat{\lambda}_e$ [Hz]	4020±1890	5375±2525	4080±1920
$\hat{\lambda}_i$ [Hz]	1100±475	1120±525	1240±585
$\langle B_x \rangle$ [nS]	0.102	0.102	0.102
α_e	0.65	0.0	0.0
α_i	0.0	0.0	0.0
β_e	0.35	0.37	0.37
β_i	0.0	0.0	0.0
ω [Hz]	2.5	2.5	2.5
τ_{OUsin} [ms]	2000	2000	2000
σ_{OUsin}	0.6	0.6	0.6
τ_{OUinp} [ms]	80	80	80
k	∞ (uncorrelated)	325	∞ (uncorrelated)

Table 2.2: Table of parameters describing the inputs. The bounds on the rates are calculated from the bounds on the mean input conductances (see Figure 2.4).

2.4 Discussion

The goal of the work presented in this chapter was to infer the statistical properties of the synaptic inputs to a neuron given the *in vivo* intracellular measurements of its membrane voltage.

The membrane voltage measurements are typically performed at the soma of the neuron, while the synapses can be located far away from the pipette location. Thus we can only estimate the effects of the synaptic inputs at the soma. To be able to infer more about the actual synaptic inputs we would need to know how their effects on the neuronal membrane voltage are modified on the way between the synapse location

and the soma due to the active and passive membrane properties. This transfer is partially addressed in the next chapter. The effects at the soma are however interesting on their own, as they are likely to be translated in the neuronal output as the soma is electrotonically very close to the initial axon segment, responsible for the initiation of the output of the neuron.

We applied the inference method on the data recorded from layer 5B neurons in the motor cortex of awake behaving mice during quiet wakefulness ($L5B_{quiet}$) and during movement, where we split the neurons in two groups. One is the group of neurons which increases the mean firing rate during movement ($L5B_{enh}$) and the other is the group of neurons which decreases the firing during movement ($L5B_{supp}$). First we estimate the mean conductance at the soma by measuring the mean voltage and mean membrane conductances in both states and compare them with the literature data from the slices. Results presented in figure 2.4 show that the increased firing rates of $L5B_{enh}$ group can be attributed to the increase in net excitatory conductance, while the decreased firing rates in the $L5B_{supp}$ group are more likely caused by the small increase in the inhibitory conductance as compared to the quiet case. While the absolute value of conductance relies on the data from the literature, namely the input resistance and the resting voltage, the relative changes between groups can be estimated independently of those values [30].

The estimation of the mean global conductances relies on the simplification of the neuron model to a passive compartment model equivalent of an RC circuit. This simplification is particularly invalid at the times when the membrane voltage crosses the action potential threshold. While this might bias the estimates when the recorded neuron is firing at the high frequencies [35], the estimations at the frequencies in this study should be practically unaffected [30].

Next we went beyond the conventional mean value estimations of the global synaptic conductances and used the second-order statistics of the membrane voltage to infer the sizes and the frequencies of the inputs. The total net conductance values provided one constraint (2.16), while the power spectral density in the β frequency band (15–30 Hz) provided another (2.13). Still we were required to make a number of assumptions. First we assumed the amplitude of the effects of the synaptic events are constant for a specific presynaptic neuron. Short term plasticity (STP) effects, which have been reported in cortex *in vitro* [46], could either increase (short term potentiation) or decrease those amplitudes (short term depression), potentially changing the mean B_x and increase the standard deviation of the amplitudes σ_{B_x} which would affect the estimation

of the input sizes (e.g. the increased standard deviation would lead to underestimation of an average event amplitude and overestimation of the global input frequencies).

We further assumed that the spike trains from different neurons are uncorrelated and that the power spectra of a spike train is uncorrelated with the amplitude corresponding to that presynaptic neuron. Experimental measurements of correlations in the brain are contradictory and largely depend on what time-scale is considered [47]. When fitting the PSD of the data, we observed a bump in activity at low frequencies [1.5–4 Hz] which could be attributed to the correlation on longer time-scales. Our method would not allow us to detect the correlations on the time scales compared to the time scales of the individual inputs, as they would contribute to the PSD in the same frequency range. Positive correlations among the spike trains of the same synaptic type would increase the PSD and cause the underestimation of mean input sizes while the positive correlations between the excitatory and inhibitory inputs would have the opposite effect. As we learn more about the spike correlations in cortex from experiments (see for example [48, 49]), we can impose more constraints on the method.

We assumed a stable shape of the conductance changes $f_x(t)$ to be an α function (2.14) with the associated time constants for excitation and inhibition. We assumed the amplitudes of the excitatory and inhibitory conductances are the same for excitation and inhibition and took the value of coefficient of variation for those inputs from the literature. Finally we assumed the amplitudes and shapes of the conductance inputs are not changing between different behavioral states. Neuromodulation effects could be fast enough to differentially influence the amplitudes.

Relaxing those assumptions could lead to a better fit for the observed power spectral densities as both the time courses of excitatory and inhibitory input conductances as well as the different amplitudes of the conductive inputs shape the PSD of the membrane voltage. However the fit using the assumptions already lead to a good fit. If we tried to improve on this by relaxing more parameters we would likely fall into problems with over-fitting (having too many free parameters for the dimensionality of the problem). Furthermore, this would not explain away the observed increase of the PSD in the β frequency band unless we also allow for those parameter to change across different states (see the discussion about the plasticity of the inputs above).

Given those assumptions we were able to estimate the mean amplitudes and the frequencies of the events (see Table 2.2). Even though we have to make many assumptions the resulting estimated output frequency is of the reasonable order of magnitude. While it is currently not possible to directly measure the inhibitory and excitatory rates

we can resort to a "back-of-an-envelope" type estimation. Each L5 pyramidal neuron has 15000 $\pm$ 5000 synapses [50], with about one fifth of those synapses being inhibitory (3000) and the rest excitatory (12000) [51]. Taking into account that each neuron to neuron connection consists of 4–8 synapses with a mean of 5.5 (see [52] and the references within), we can estimate each neuron receives input from about 2200 excitatory (Ne) and 550 inhibitory (Ni) presynaptic neurons. Given the firing rate of the excitatory neurons (3$\pm$2 Hz, our data) we estimate a total excitatory input rate of 6600 Hz. If we assume a similar firing rate for the inhibitory neurons, we estimate a total inhibitory input rate of 1650 Hz. Such estimates for both synaptic types are slightly higher than the estimates of the rate of events coming from the estimation method presented in this chapter. This is not very surprising as our method does not predict the actual synaptic inputs but rather the events reaching the soma (see the next chapter).

During the quiet wakefulness we saw an increase in the power spectral density for the frequencies between 1.5–4 Hz. Similar oscillations have been reported in other cortical areas both from intracellular as well as extracellular recordings [53, 54, 55]. With our model we showed these can be explained by incorporating the temporal firing rate modulations in the excitatory inputs (equation 2.17 and table 2.2). Specifically we modified the mean firing rate of the Poisson spike trains by adding a sinusoidal component with a noisy phase and an Ornstein-Uhlenbeck (OU) process. The sinusoidal component is only present during the quiet wakefulness.

For the $L5B_{enh}$ case, the increase in the net firing rate alone could not fully explain the increase of the power spectral density in the β frequency band (15-30 Hz). One of the possible explanations which we explored was the introduction of instantaneous correlations in the excitatory inputs. Adding instantaneous correlations with Pearson coefficient of 0.003 between the two pairs of inputs was sufficient to match the PSD of the simulated membrane voltage to the PSD of the recorded membrane voltage (Fig. 2.8a). This addition also provided a qualitative match for the changes in frequency of the compound presynaptic events (Fig. 2.8c). However, we can not exclude other possible explanations, such as changes in the probability distribution of the difference in input amplitudes between the two states, which could be caused by a change in the amplitudes of the individual spike trains due to neuromodulation or by a selective increase in the frequency of the input trains with bigger amplitudes.

In the next chapter we attempt the step from estimating the inputs to the soma, to estimating the global inputs to the neuron by investigating the effects of the neuronal morphology on the recordings at the soma. The result of those effects is finally applied

to results of this chapter in the Overview chapter.

Chapter 3

The effect of morphology on the synaptic input

3.1 Introduction

Chemical synapses are primary elements in information-processing functions of the nervous system. An action potential of a presynaptic neuron will cause the opening of channels in the membrane of a postsynaptic neuron at the synapse. The resulting change in the membrane conductance will induce a synaptic current based on the reversal potential determined by the permeability of opened channels. This current causes a local change in the membrane voltage. Given sufficient levels of membrane depolarization caused by this process the opening of voltage-dependent channels will cause an action potential in the post-synaptic neuron. Most of those channels are located at the soma and the axon initial segment [8].

As the membrane voltage deflection is propagated from the location of the synapse towards the soma it is attenuated due to the leak conductance and membrane capacitance. This attenuation will influence the output of the neuron.

Similarly as the effects of the synaptic event on the membrane voltage will be felt throughout the neuron, the effects on the membrane input conductance will be propagated from the synapse to other parts of the neuron. This change in the input conductance is important as it dictates the level of membrane deflection caused by a subsequent, nearby input.

In the previous chapter we used the changes in the membrane voltage and input conductance to predict the input to the soma caused by presynaptic events. In this chapter I use a combination of the analytical calculations and numerical simulations

to study the attenuation of the membrane voltage and input conductance with a special focus on how the attenuation affects the estimation of excitatory and inhibitory inputs.

The work in this chapter builds on the seminal work of Wilfried Rall, a pioneer in establishing the integrative functions of neuronal dendrites through the development of cable theory [15, 56, 7, 8].

I first simplify the neuronal morphology and derive the analytical expressions for the attenuations of conductance change and voltage deflection for the case of a homogenous cable (see figure 3.1 for the illustration). I assume the voltages stay under the firing threshold where most of the voltage-dependent channels (active channels) are inactive and thus treat the cable as electronically passive. I then go on to show the conductance is attenuated more strongly than the membrane voltage and how this would cause a misestimation of the ratio between the excitatory and inhibitory synaptic input.

Finally I take a look at the realistic neuron morphologies and use numerical simulations to estimate the levels of attenuation for different cases of synapse distributions. I specifically look at the misestimation for the case of Layer 5 pyramidal cells.

3.2 Methods

3.2.1 Cable model calculations

First a neuron is approximated as a homogenous coaxial cable of length $l[m]$, diameter $d[m]$, axial resistivity $R_i[\Omega m]$, specific membrane resistance $R_m[\Omega m^2]$ and membrane capacitance $C_m[F/m^2]$. As the cable is considered to be of a constant diameter d, it is useful to express them as quantities per unit length

$$\begin{aligned} r_a &= \frac{4R_i}{\pi d^2}\ [\Omega/m] \\ r_m &= \frac{R_m}{\pi d}\ [\Omega m] \\ c_m &= \pi C_m d\ [F/m]. \end{aligned}$$

These units have the advantage that the cable equation now contains no explicit terms depending on the cable diameter. The cable equation describes the membrane voltage ($v(x,t)$) dynamics of the cable [8]

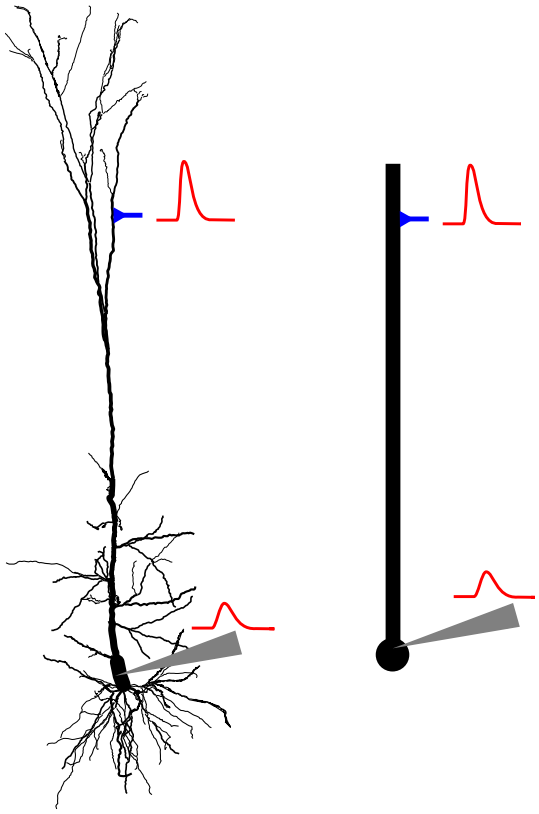

Figure 3.1: **Simplification of the full morphology into a cable.** (left) Morphology of a Layer 5 pyramidal cell [57] from the somatosensory cortex of a rat. An excitatory synapse (blue) locally causes a membrane voltage deflection (red, top left), which is attenuated as it propagates towards the soma (red, bottom left), where it is measured by an intracellular recording (gray). (right) A simplification of the system, reducing the full morphology to a cable so that it can be treated more generally.

$$\frac{r_m}{r_a}\frac{\partial^2 v(x,t)}{\partial x^2} = r_m c_m \frac{\partial v(x,t)}{\partial t} + v(x,t) - r_m I_{inj}(x,t). \tag{3.1}$$

$I_{inj}(x,t)$ is the input current. The membrane voltage $v(x,t)$ in the above equation is relative to the leak reversal potential and will decay to zero in case of no external inputs. The analytical analysis is restricted to the steady-state solution where the voltage is no longer changing with time ($\partial v(x,t)/\partial t = 0$), so that equation(3.1) can be simplified to

$$\frac{r_m}{r_a}\frac{d^2 v(x)}{dx^2} = v(x) - r_m I_{inj}(x). \tag{3.2}$$

3.2.1.1 Semi-infinite cable

In the case of a semi-infinite cable ($l = \infty$) with the current input at the sealed end of the cable ($x = 0$, $I_{inj} = I_0\delta(x)$), the steady-state solution for membrane voltage is [8]:

$$v(x) = V_0 e^{-\frac{x}{\lambda}}. \tag{3.3}$$

where $\lambda = \sqrt{\frac{r_m}{r_a}}$ and $V_0 = I_0 r_m/\lambda$. To derive this expression one needs to solve the steady-state equation (3.2) with $I_{inj} = 0$ (for $x \neq 0$) with a boundary condition $\frac{dv}{dx}(x = 0) = -r_a I_0$.

λ is the so-called *space constant* of the cable. $R_\lambda = \sqrt{r_a r_m}$ is the *characteristic input resistance* (the input resistance at the end of a semi-infinite cable [8]). I use these two quantities as a reference in the further calculations.

3.2.1.2 Finite-length cable with point synapses

To calculate the analytical values for membrane voltage deflections and the input conductance changes caused by synaptic inputs the steady-state cable equation (3.2) is solved for the cases of synaptic input being present or absent. In both cases I solved the system with and without injected current I_{inj} at the location of the soma to determine the change in input conductance (this process is described in more detail in section 3.2.1.4).

In the case of a finite number of synaptic inputs I treated them as point conductance inputs at the location of the synapse ($x_i = s_i l$, $s_i \in [0,1]$) where l is the length of the cable. The current injected into the cable due to one such conductive input at the

location s_i is $I_{inj}(x) = g_s(v - E_s)\delta(x - s_i l)$, where g_s is the injected conductance and E_s is the synaptic driving voltage relative to the leak voltage. We can then solve equation (3.2) by solving the cable equation in $N+1$ pieces split by the synaptic locations, where N is the number of distinct synapse locations. Each piece (i) describes a cable segment between two synapses and follows the spatial dynamics

$$\lambda^2 \frac{d^2 v_i(x)}{dx^2} = v_i(x), \tag{3.4}$$

with the following boundary conditions connecting the pieces

$$v_i(x = s_i l) = v_{i+1}(x = s_i l), \tag{3.5}$$

$$\frac{dv_{i+1}}{dx}(x = s_i l) - \frac{dv_i}{dx}(x = s_i l) = r_a g_{s_i}(v_i(x = s_i l) - E_{s_i}). \tag{3.6}$$

The first condition ensures the membrane voltage continuity along the cable and the second one accounts for the synaptic current introduced by the point conductances. For the case where we have several synaptic inputs at the same location the right side of the equation (3.6) becomes the sum over all those inputs.

Finally we consider the cables to be closed (no current flows out from the neuron at the ends of the cables) and thus add the following boundary conditions:

$$\begin{aligned} \frac{dv_0}{dx}(x = 0) &= 0. \\ \frac{dv_N}{dx}(x = l) &= 0. \end{aligned} \tag{3.7}$$

While the above is a description of a general solution for any number of discrete synapse locations on the cable, in this chapter I only use the case of one discrete synapse location, so we only have two pieces ($i \in \{0\}$).

3.2.1.3 Finite-length cable with evenly distributed synapses

The number of synapses distributed along the dendritic tree can reach tens of thousands. To approximate this in the cable model I introduced a continuous synaptic conductance-based current along the cable instead of using discrete point synapses. I represented this current by the synaptic current resistance per unit length $r_s(x)$ [Ωm], analog to the membrane resistance per unit length (r_m). I solved the system for the

case of evenly distributed synapses along the cable ($r_s(x) = r_s$) where the cable equation (3.2) now becomes

$$\frac{r_m r_s}{(r_m + r_s) r_a} \frac{d^2 v(x)}{dx^2} = v(x) - \frac{E_s r_m}{r_m + r_s}, \tag{3.8}$$

where as before E_s is the synaptic driving voltage relative to the leak voltage.

As we can see from the above equation the space constant shortens to $\lambda' = \sqrt{\frac{r_m r_s}{r_a(r_m+r_s)}}$ and accordingly the characteristic input resistance of the semi-infinite cable reduces to $R'_\lambda = \sqrt{r_a \frac{r_m r_s}{r_m+r_s}}$. The total input conductance g_s introduced in this way depends on the cable length $g_s = l/r_s$.

3.2.1.4 Calculating the input conductance at the soma

To calculate the input conductance g at the soma, first the voltage deflection at the soma, ΔV, caused by the injection of a steady current $I_{inj} = I_0 \delta(x)$ is calculated. For this the equations (3.4) and (3.8) are solved with the boundary condition (3.7) to get $v_1(x)$ and the boundary condition $\frac{dv_0}{dx}(x = 0) = -r_m I_{inj}$ to get $v_2(x)$. From this the voltage deflection at the soma is expressed as $\Delta V = v_2(x = 0) - v_1(x = 0)$. The input conductance at the soma can then be calculated according to Ohm's law as $g = I_{inj}/\Delta V$. This is done both for the case of the system without synaptic inputs ($g_s = 0$) as well as for the case with synaptic inputs to get the difference of the input conductances Δg.

3.2.2 Alternative representations of the morphology effects

The conductance-based synaptic inputs change both the membrane voltage as well as the input conductance, where the input conductance is defined as the ratio between the injected current and the resulting membrane voltage deflection. The change is local in space but spreads to the other parts of the neuron [8, 58]. We are mostly interested in the induced changes at the soma (ΔV and Δg for voltage and input conductance changes respectively) as this is the location most relevant to the neuron output, and is also the location where it is easiest to record from.

To study the effects of morphology on the measurements at the soma we first look at the case of a synapse located at a specific location on a neuron. At that location the synaptic current i_s is conductance-based and can be expressed as $i_s = g_s(E_s - v_s)$ where E_s is the reversal potential of the synapse, g_s is the conductive input at that location and v_s is the membrane voltage at the location of the synapse.

One way of describing the morphology effects at the soma is by imagining the input current being modified as it makes its way towards the soma. If we employ the same model to describe the membrane voltage dynamics at the soma as in the previous chapter (see equation(2.1)) we get

$$C\frac{dv(t)}{dt} = -g_L v(t) + i(v(t)). \tag{3.9}$$

where $i(v(t))$ is the modified synaptic input current and g_L is the leak conductance at the soma (conductance in the absence of synaptic inputs). Note that here all the voltages and reversal potentials are considered relative to the neuron leak voltage, so that $v = 0$ in the absence of inputs. In the remainder of this section we focus on the steady-state solutions ($\frac{dv(t)}{dt} = 0$).

When the synapse is located directly at the soma so that the synaptic current is not modified by morphology ($i = i_s$) we are dealing with the same system as in the previous chapter ($Cdv/dt = -g_L v + g_s(E_s - v)$). Solving this equation in the steady-state ($dv/dt = 0$) it is then easy to derive the corresponding observed changes in the voltage (ΔV) and input conductance (Δg) between the case of no synaptic input ($g_s = 0$, $v = 0$) and the case of synaptic input ($g_s > 0$, $v = E_s\frac{g_s}{g_s+g_L}$):

$$\Delta V = E_s\frac{g_s}{g_s + g_L}, \tag{3.10}$$

$$\Delta g = g_s. \tag{3.11}$$

In the case where the synapse is located away from soma the changes at the soma are affected by the morphology. For the case of a single synaptic type and location we can still simplify the system into an equivalent point model (Eq. (3.9)) using two alternative representations of the input current at the soma $i(v)$.

3.2.2.1 The modified reversal potential

In the first representation we write the input current as a conductive input with a modified input conductance ($\hat{g}_s$) and a modified reversal potential ($\hat{V}_s$)

$$i_s = \hat{g}_s\left(\hat{E}_s - v\right). \tag{3.12}$$

The full steady-state equation for the membrane voltage (3.9 with $dv/dt = 0$) is then

$$g_L v = \hat{g}_s \left(\hat{E}_s - v\right). \tag{3.13}$$

We introduce the index $k \in \{1,2\}$ to denote the case when the synaptic input is absent (1) and when the input is present (2) when talking about the membrane voltage (v_k) and membrane input conductance (g_k). In the absence of input ($i_s = 0$) the membrane potential $v_1 = 0$. The change of voltage is then $\Delta V = v_2 - v_1 = v_2 = \frac{\hat{g}_s \hat{E}_s}{\hat{g}_s + g_L}$. The change of input conductance ($\Delta g = g_2 - g_1$) can be calculated by separately calculating the input conductance for both cases. As in the case of the cable equation the input conductance is calculated as the ratio between the additional injected tonic current I_{inj} and the resulting change of voltage (3.2.1.4). It is easy to show $g_1 = g_L$ and $g_2 = g_1 + \hat{g}_s$ and therefore $\Delta g = \hat{g}_s$.

We can now express the newly defined parameters $\hat{g}_s$ and $\hat{E}_s$ as functions of the observed Δg and ΔV

$$\hat{g}_s = \Delta g, \tag{3.14}$$

$$\hat{E}_s = \Delta V \frac{\Delta g + g_L}{\Delta g}. \tag{3.15}$$

3.2.2.2 Conductance-based and current-based input - the $\tilde{\alpha}$ factor

Another way to represent the effects of the morphology is to split the input to the soma into conductance based and current based contributions to the synaptic current [59]

$$i_s = \tilde{g}_s \left(\tilde{\alpha}(E_s - v) + (1 - \tilde{\alpha})E_s\right). \tag{3.16}$$

Conductance based contribution ($\tilde{g}_s \tilde{\alpha}(E_s - v)$) depends on the voltage, whereas the current based contribution ($\tilde{g}_s(1 - \tilde{\alpha})E_s$) is independent of it. $\tilde{\alpha}$ lies in the interval $[0,1]$ and represents the proportion of the input of conductive nature. In the case when the synapse is located at the soma, the input is fully conductive and $\tilde{\alpha}$=0.

As before we can express the change in the membrane voltage and input resistance between the case of with or without input. The change of membrane conductance is $\Delta v = \frac{\tilde{g}_s E_s}{g_L + \tilde{g}_s \tilde{\alpha}}$ and the change of input conductance is $\Delta g = \tilde{g}_s \tilde{\alpha}$.

We can now express the new parameters $\tilde{g}_s$ and $\tilde{\alpha}$ as the function of the observed changes at the soma or the function of the parameters ($\hat{g}_s$, $\hat{E}_s$) defined in the previous section

$$\tilde{g}_s = \frac{\Delta V(g_L + \Delta g)}{E_s} = \frac{\hat{E}_s \hat{g}_s}{E_s}, \tag{3.17}$$

$$\tilde{\alpha} = \frac{\Delta g E_s}{\Delta V(g_L + \Delta g)} = \frac{E_s}{\hat{E}_s}. \tag{3.18}$$

3.2.3 Simulations

Simulations were performed using NEURON simulation environment [60]. Unlike the Brian simulator which is developed with the goal of facilitating the simulations of neural networks, where neurons are simple point models (such as the one described in chapter 2), the NEURON is designed with the aim of constructing and applying empirically-based models of single neurons and neural networks, where the single neuron models are typically more morphologically realistic (complex). It uses a numerical solver for the linked differential and algebraic equations representing the parts of the morphology (dendrite segments, synapses). The numerical integration method used was the default NEURON Backward Euler integration method [61].

3.2.3.1 Cable simulations

The synaptic input was simulated as a point process injected at a certain location on the cable. Each presynaptic event causes a transient onset of the input conductance in the shape of an α function ($\alpha(t) = \frac{t}{\tau_s} e^{(1-t/\tau_s)}$; $t > 0$) with a time constant $\tau_s = 2.5ms$ and a synaptic reversal potential $E_s = 0mV$ leading to the synaptic current.

3.2.3.2 Full neuron simulations

The neuron morphologies were selected to represent different types of neurons. As the basis I took the Layer 5 pyramidal cell from the somatosensory cortex of a rat, for which a full model, including the biophysical properties of the cell optimized to best match a variety of the measured stimuli responses, was available in the online database of neuron models ModelDB [57]. In the simulations performed to create figure 3.8 I used the passive biophysical properties of the model with the values described in table 3.1. The other two morphologies, the Stellate cell [62] and the Bitufted cell [63] (both from rat neocortex) were taken from the NeuroMorpho.org database [64]. For the passive properties I used the same values as for the Layer 5 pyramidal cell.

Each cell morphology is split into smaller computational units - compartments. For all three cells the same compartmentalization procedure was used, which splits

Parameter description	Symbol [unit]	default value
Leak reversal potential	$E_L[mV]$	-65
Axial resistivity	$R_i[\Omega m]$	1
Specific membrane resistance in soma	$R_m^{soma}[\Omega m^2]$	2.96
Specific membrane resistance in basal dendrites	$R_m^{basal}[\Omega m^2]$	2.14
Specific membrane resistance in apical dendrites	$R_m^{apical}[\Omega m^2]$	1.70
Specific membrane resistance in the axon	$R_m^{axon}[\Omega m^2]$	3.08
Specific membrane capacitance in soma and axon	$c_m^{soma,axon}[\mu F/cm^2]$	1
Specific membrane capacitance in the dendrites	$c_m^{basal,apical}[\mu F/cm^2]$	2

Table 3.1: Table of parameters for the simulations on the full passive neuronal morphologies (Stellate cell, Bitufted cell, Layer 5 pyramidal cell).

the morphology sections (cables between two branching points) into compartments no longer then 40 μm. The split resulted in 642 compartments for the Layer 5 pyramidal cell with the mean compartment length of 19.3μm, 171 compartments with 16.6μm mean compartmental length for the Stellate cell and 51 compartments with 22.1μm mean compartmental length for the Bitufted cell.

Each simulation included 5000 synapses of the same strength (max. conductance input $0.01nS$) and same frequency of presynaptic action potentials (Poisson train). The time course of the conductance increase following an individual presynaptic action potential was an α function with the time constant $\tau_e = 2.5ms$. The reversal potential causing an input current due to the synaptic conductance was set to $E_E = 0mV$.

In the simulations for figure 3.9 I used the morphology of the Layer 5 pyramidal cell with both excitatory and inhibitory synaptic inputs. The synaptic time constants used were $\tau_e = 2ms$ and $\tau_i = 10ms$ [42] and with reversal potentials $E_E = 0mV$ and $E_I = -75mV$ for excitatory and inhibitory inputs respectively, while the leak reversal potential was set to $E_L = -62mV$ [39].

3.3 Results

The measured voltage and conductance changes at the soma are a combination of the synaptic inputs and the morphology effects. In the previous chapter I introduced a method for the estimation of the synaptic input effect at the soma. For this I used measurements of the time-averaged changes of the membrane voltage $\Delta\langle v\rangle$ and the input

conductance $\Delta\langle g\rangle$ at the soma and then used a point-model of a neuron to infer the effective conductive inputs (see equations (2.6) and (2.7)), thus ignoring the morphology effects.

In order to investigate those effects I first looked at the commonly-used simple extension of a point-model - a homogenous cable of a length l, representing the dendrite with the soma at one end.

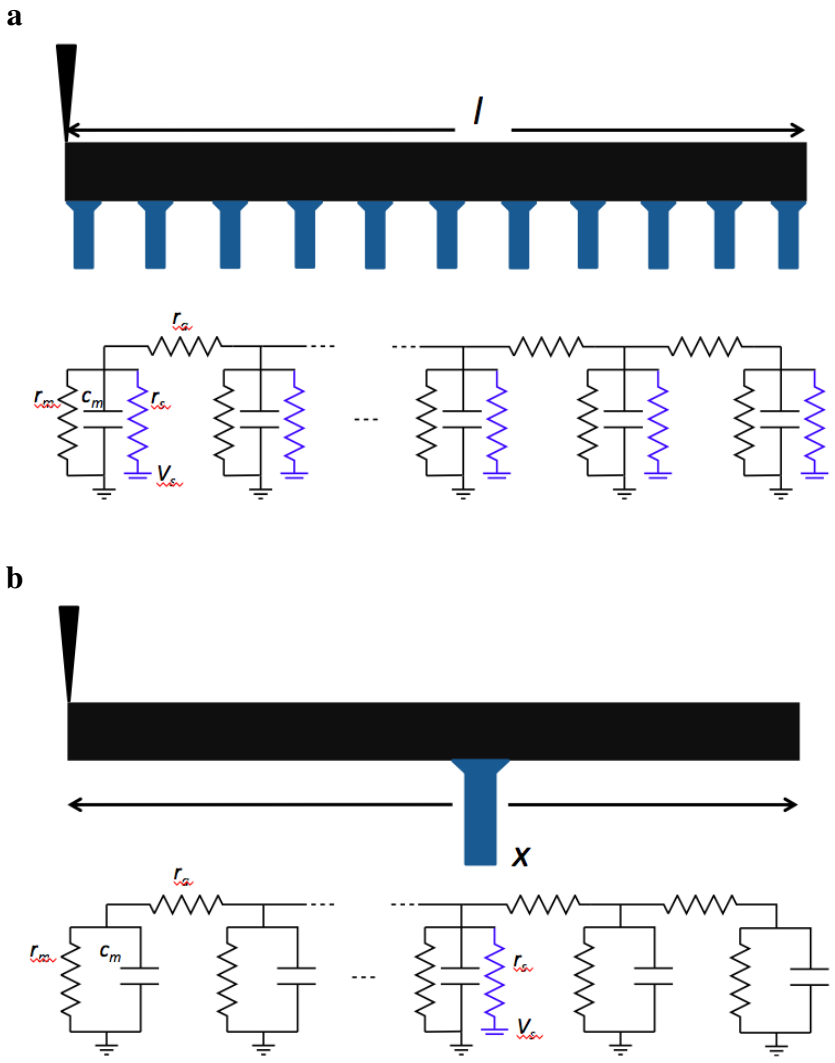

Figure 3.2: **The cable setup. (a):** Single synapse on a cable of the length l at a position $x = sl$; $s \in [0,1]$. The voltage and input conductance changes are measured at one end of the cable ($s = 0$). The corresponding electrical circuit is shown below. **(b):** Distributed synapses on a cable of a length l. The corresponding electrical circuit is shown below.

3.3.1 Conductance attenuates faster than the voltage in cables

3.3.1.1 Finite-length cable with point synapse

I first studied the case of a single synapse located at the position $x = sl$ on the cable, where $s \in [0,1]$. If $s = 0$ the synapse is located at the soma $x = 0$.

It is possible to analytically calculate the change of membrane voltage and the change of input conductance at the soma between the case of no input ($g_s = 0; V = E_L$) and the case of a single synapse with the input conductance $g_s(t) = g_s$ by solving the cable equation (3.4) in the stable state. The solutions of the cable equation are generally hyperbolic geometric functions and depend on the boundary conditions (see section 3.4). The exact derivations were performed using Mathematica [65].

Solving the cable equation in the steady state yields $v(x)$ for $x \in [0,l]$. We can use this to can express the input induced difference in the membrane voltage at the soma ($x = 0$) as

$$\Delta V = \frac{2g_s R_\lambda E_s \cosh(L(1-s))}{g_s R_\lambda \cosh(L) + g_s R_\lambda \cosh(L(1-2s)) + 2\sinh(L)}, \tag{3.19}$$

where $L = l/\lambda$ is the relative length of the cable normalized by its characteristic space constant and R_λ the input resistance of a semi-infinite cable (see 3.2 Methods). Following the procedure outlined in 3.2.1.4 we can also calculate the difference in the input conductances felt at the soma

$$\Delta g = \frac{2g_s \cosh^2(L(1-s))\mathrm{sech}(L)}{2\cosh(L) + g_s R_\lambda (\sinh(L) - \sinh(L(1-2s)))}. \tag{3.20}$$

Setting $s = 0$ in the equations (3.19) and (3.20) gives us

$$\Delta V = E_s \frac{g_s}{g_s + \frac{\tanh(L)}{R_\lambda}}, \tag{3.21}$$

$$\Delta g = g_s, \tag{3.22}$$

which corresponds to the point-neuron case (See equations (3.10) and (3.20) and take into account the leak conductance of a finite-length cable in the absence of any conductive inputs is $G_L = \tanh(L)/R_\lambda$ [8]). If all the synapses were located at the soma, morphology effects could be compressed into the effective leak conductance and neglected when it comes to the estimations of inputs.

If the synapse is located away from the soma, we would expect both the changes in voltage and changes in the input conductance to be smaller compared to the case when the synapse is located at the soma, as the cable is leaky and we lose the synaptic current when it travels along the cable. In figure 3.3a I show the dependence of both the voltage and the conductance change on the location of the synapse according to the analytical results. For the ease of comparison, both are plotted relative to their respective changes in the case when the synapse is located at the soma. Although both changes are indeed reduced with the distance of the synapse from soma, the change in the input conductance is being reduced faster than the change in the membrane voltage.

To verify that the analytic calculations, which assume a constant synaptic input, also hold for the case of the more realistic time varying conductive input I performed a numerical simulation of the system, where the synaptic input is a Poisson-like spike train of unitary conductance events (see 3.2 Methods). Figure 3.3a shows the analytical calculations match the numerical simulations exactly.

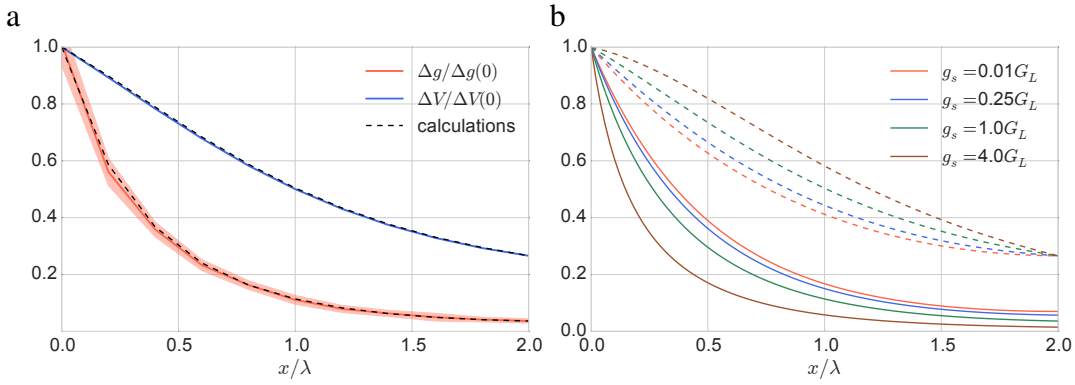

Figure 3.3: **The attenuation of voltage and input conductance changes based on the location of the synapse on the cable (a):** The relative attenuation of the voltage change (blue) and the input conductance change (red) as a result of the synaptic input at various locations of the cable from the simulations on a cable of relative length $L = 2$. The are corresponds to one standard deviation from the mean using the results of 10 repetitions (for each synapse location). The dashed black lines denote the values obtained by the calculations (Eq. 3.19 and Eq. 3.20). **(b):** The derived ratio between the conductance change attenuation (solid lines) and membrane voltage deflection change attenuation (dashed lines) depends on the input strength.

Figure 3.3b shows how the morphology effects change with the size of the input. While the voltage difference is always reduced slower than the conductance, this difference is only increased by the increased synaptic input.

Knowing the changes of the voltage and the input conductance, we can express the parameters for the alternative representation of the morphology effects (see 3.2.2) as

$$\hat{g}_s = \Delta g, \tag{3.23}$$

$$\hat{E}_s = E_s \frac{\cosh(L)}{\cosh(L(1-s))}. \tag{3.24}$$

$$\tilde{g}_s = \frac{2g_s \cosh(L(1-s))}{2\cosh(L) + g_s R_\lambda (\sinh(L) - \sinh(L(1-2s)))}, \tag{3.25}$$

$$\tilde{\alpha} = \frac{\cosh(L(1-s))}{\cosh(L)}. \tag{3.26}$$

Note how the modified reversal potential ($\hat{E}_s$) and the α factor do not depend on the strength of the synaptic input but only on the location of the synapse.

3.3.1.2 Finite-length cable with evenly distributed synapses

A neuron will typically have several synaptic locations on the dendritic tree. In the previous section I showed how each of those inputs causes not only a local, but also a geometrically spreading change in the membrane voltage and the input conductance. Those changes will influence the synaptic inputs at other locations.

To investigate this interaction among the synaptic inputs at different locations I next studied the case of geometrically uniformly distributed synapses on a cable of length l. The synapses are represented with a uniform synaptic input resistance per unit length r_s and the reversal potential E_s. The introduction of this uniform synaptic input changes the space constant and the characteristic input resistance of the cable. I define λ' as the effective space constant, R'_λ as the effective characteristic input resistance denote $L' = l/\lambda'$. Finally I define γ as the ratio between the effective and the base values

$$\gamma := \lambda'/\lambda = L/L' = R'_\lambda/R_\lambda = \sqrt{\frac{r_s}{r_m + r_s}}.$$

We can see that in the case where there is no synaptic input ($\lim_{r_s \to \infty}$), the effective values are the same as the basis ones ($\gamma = 1$).

Solving the cable equation in the static form with and without the synaptic current resistance per unit length r_s makes it possible to analytically calculate the change of membrane voltage at the soma (see subsection 3.2.1.3)

$$\Delta V = E_s \frac{1}{1+\frac{r_s}{r_m}} = E_s(1-\gamma^2). \tag{3.27}$$

Similarly I calculated the difference in the input conductance

$$\Delta g = \frac{\tanh(L')}{R'_\lambda} - \frac{\tanh(L)}{R_\lambda}. \tag{3.28}$$

As in the case of the single synapse, we can now express the parameters for the alternative representation of the morphology effects (see the Methods) as

$$\hat{g}_s = \Delta g, \tag{3.29}$$

$$\hat{E}_s = \frac{E_s \tanh(L')}{(1-\gamma^2)\tanh(L') - \gamma\tanh(L)} \tag{3.30}$$

$$\tilde{g}_s = \frac{1-\gamma^2}{R'_\lambda}\tanh(L'), \tag{3.31}$$

$$\tilde{\alpha} = \frac{1-\gamma\coth(L')\tanh(L)}{1-\gamma^2}. \tag{3.32}$$

3.3.2 Misestimation of excitatory and inhibitory conductances

In chapter 2 we described a method for input estimation in the point neuron model based on the measurements of changes in the mean input conductance ($\Delta\langle g\rangle$) and mean membrane voltage ($\Delta\langle V\rangle$) between the case with no conductive inputs and the case of conductive inputs (see equations (2.6) and (2.7)). When we consider more realistic neurons with more complex morphology than a single compartment, the location of the synapse would typically be located away from the soma, where we measure the membrane voltage and input conductance ($s \neq 0$). This means that both the measured voltage deflection and the measured change in the input conductance caused by the synaptic input are smaller than they would be if we measured them at the location of the synapse. Figure 3.3 shows the relative attenuation based on the location of the synapse from the soma where I simplified the morphology to the case of a cable. This effect causes the method to underestimate the net input conductance. What is less obvious, is that the method will cause a misestimation in the ratio between the excitation and inhibition in the cell, as it is assuming the synapse is located at the location of our measurement ($s = 0$).

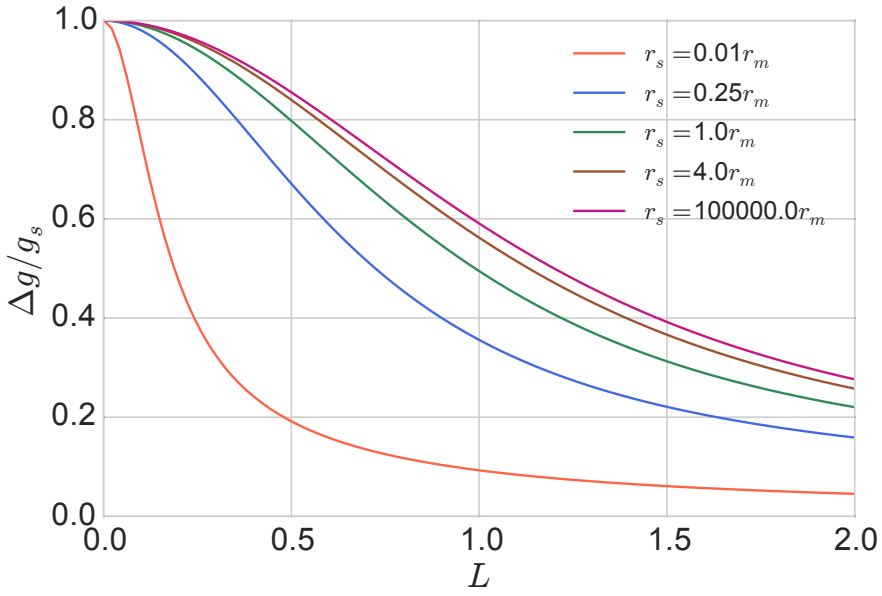

Figure 3.4: The relative input conductance change for a cable with uniformly distributed synapses as a function of the cable length for different synaptic input sizes. For a very short cable the change in the conductance is the same as the input synaptic conductance, while as we increase the cable length, the change in the measured input conductance at the soma no longer reflects the injected synaptic conductance. This effect is bigger for larger input conductances.

To better understand this misestimation consider the case where we only inject the excitatory conductance at the location away from the soma ($s \neq 0$). The method for the input estimation assumes two types of conductive inputs, excitatory and inhibitory (g_E and g_I respectively), the effects of which on the membrane voltage are determined by their reversal potential (E_E and E_I). It expects that an amount of excitatory conductance G_E^i will increase the membrane voltage by ΔV^i. In our example of only an excitatory input conductance at a location away from the soma, both the actual measured change in the input conductance Δg and the measured change in the membrane voltage at the soma ΔV will be smaller than what would be expected in the point model. However, as seen in Figure 3.3, the relative attenuation of input conductance change is bigger than the attenuation of the voltage increase. As far as the point model based method is concerned, the observed voltage increase ΔV cannot be explained by the input excitatory conductance even if all of the input conductance is excitatory ($G_E^{est} = \Delta g$). As the model does not limit the conductances to positive values, the result of the conductance estimation is a physically impossible combination of a negative inhibitory conductance with a positive excitatory conductance.

Excitatory and Inhibitory synapse

Typically the input to the cell consists of both excitation and inhibition. To explore the misestimation in the presence of both, I studied a simplified cable case with one excitatory and one inhibitory input both at the same location s. Treating the problem in the same way as for the case of a single input on a cable, but with changing the boundary condition (3.6) to include both inputs, I derived the solutions for the induced change of the membrane voltage and input conductance at the soma,

$$\Delta V = \frac{2R_\lambda(g_E E_E + g_I E_I)\cosh(L(1-s))}{(g_E+g_I)R_\lambda\cosh(L) + (g_E+g_I)R_\lambda\cosh(L(1-2s)) + 2\sinh(L)},$$
$$\Delta g = \frac{(g_E+g_I)\cosh^2(L(1-s))\mathrm{sech}(L)}{\cosh(L) + (g_E+g_I)R_\lambda\cosh(L(1-s))\sinh(Ls)},$$

where g_E and g_I are the induced excitatory and inhibitory input conductances and E_E and E_I are the excitatory and inhibitory reversal potentials respectively.

We can again use the alternative modified reversal potential representation and express its parameters as

$$\hat{g}_s = \Delta g, \tag{3.33}$$

$$\hat{E}_s = \frac{(g_E E_E + g_I E_I)\cosh(L)}{(g_E + g_I)\cosh(L(1-s))}. \tag{3.34}$$

When the input locations are at the soma ($s = 0$), the modified reversal potential is a weighted average of the excitatory and inhibitory reversal potentials ($\hat{E}_s = \frac{(g_E E_E + g_I E_I)}{(g_E + g_I)}$). However when $s > 0$ the apparent reversal potential increases.

We can now take the calculated changes in membrane voltage and conductance at the soma caused by the synaptic input, use them to estimate the input synaptic conductance (see equations (2.6) and (2.7)) and then compare the estimated values (G_E^{est}, G_I^{est}) with the actual ones (G_E, G_I). In Figure 3.5 I plot the misestimation in cases where excitatory and inhibitory synapses are present at the same location on the cable away from the soma.

As expected due the attenuation of voltages and conductances we underestimate the input conductances (Figure 3.5a-c). Figures 3.5 a and b show the levels of misestimation in the cable of length $L = 2$ in the case when the input locations are at the location $x/\lambda = sL = 0.5$ for varying levels of excitatory and inhibitory input conductance. We can see how for the cases when one type of the input, excitation or inhibition, is much stronger than the other type, the estimated conductances can even be negative, because the estimation method can not explain the extent of voltage change with an amount of observed conductance change (voltage is attenuated less than the conductance).

Misestimation of the ratio between excitation and inhibition

Already in figures 3.5a and 3.5b we see how the inhibition is underestimated more than the excitation. This is shown more clearly in figure 3.5c, where I used the same setup as for the previous two figures ($x/\lambda = 0.5$), but always varied the level of input conductance while keeping it the same for both excitation and inhibition ($G_E = G_I$). We see not only how the conductances are more underestimated when we increase the input strength (relative to the membrane input conductance in the case of no synaptic inputs G_L), but also how the ratio between the two is perturbed. While the actual input conductances are the same for all strengths, the estimated inhibition (red line) is always smaller than the estimated excitation (blue line).

I further explored this misestimation of the ratio between the excitation and inhibition as a function of the synapse location in figure 3.5d. Here I kept the input

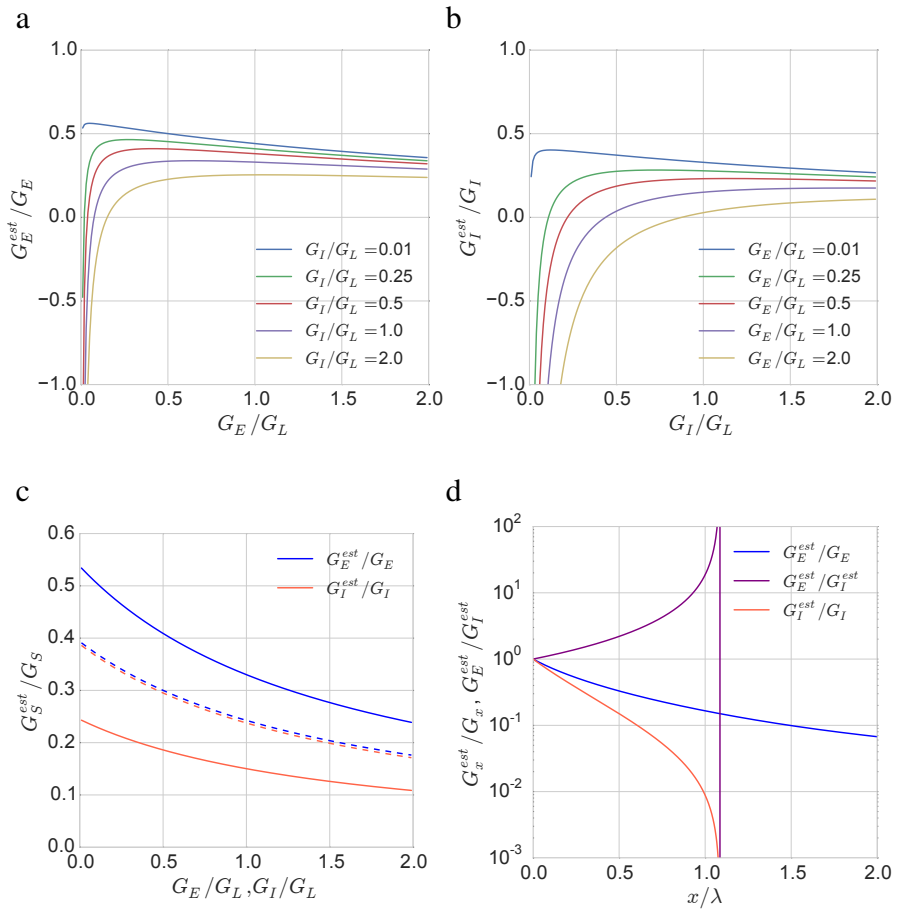

Figure 3.5: **Misestimations for a cable with both excitatory and inhibitory input at the same location. (a)**: The excitatory and inhibitory inputs are located at the same position $x/\lambda = 0.5$ away from soma on a cable of length $L = 2$. The plots are showing the analytical results of the estimation of excitatory inputs for different excitatory input strengths (x axis) with each line representing a different level of inhibitory input. **(b)**: Same as (a) but for the misestimation of inhibitory conductances. **(c):** Same setup as in the panels (a) and (b) but now the excitatory and inhibitory inputs are always equal ($G_E = G_I$). The plot shows the estimation of excitatory (blue solid line) and inhibitory (red solid line) conductances as we vary the input strengths. The dashed lines present the case where we change the excitatory and inhibitory reversal potential so that the absolute difference between the excitatory/inhibitory reversal potential and the leak reversal potential is the same. The lines are completely overlapping but drawn slightly apart for visualization purposes. **(d):** Same setup as in (a) but now with fixed input strengths ($G_E = G_I = G_L$) and varying synapse location. The purple line represents the ratio between the estimated excitatory and estimated inhibitory conductance. For the synaptic locations above $x/\lambda > 1.07$ the estimated inhibitory conductance becomes negative.

conductances constant at the level of the membrane input conductance in the absence of inputs ($G_E = G_I = G_L$) and varied the synaptic location along the cable. When the inputs are located at the soma, we get the correct ratio between the excitation and inhibition (purple line) while as the input is further away from the soma, the estimated inhibition (red line) starts decreasing faster than the estimated excitation (blue line) to the point at around $x/\lambda = 1.07$ where the estimated inhibition becomes negative.

The cause for the misestimation of the ratios is in the difference of relative reversal potential of the different types of inputs. The absolute difference between the excitatory reversal potential ($V_E = 0mV$) and the leak reversal potential ($V_L = -65mV$) is bigger than the absolute difference between the inhibitory reversal potential ($V_I = -80mV$) and the leak reversal potential. Because the change in voltage attenuates less than the change in conductance, when the inputs are located away from the soma the ratio between the voltage and conductance changes at the soma will be bigger than it would be if the input was located at the soma. As the estimation method is expecting a smaller ratio between the change in voltage and the change in conductance, it will favor the type of the input with the higher absolute difference between the leak reversal potential and the synaptic input reversal potential.

Indeed if we look at the artificial case where we change the reversal potentials so that the reversal potential of excitatory input is $V_E = -25mV$ and the reversal potential of inhibitory inputs is $V_I = -105mV$ while keeping the leak reversal potential at $V_L = -65mV$ and repeat the same setup as in 3.5c we see that the ratio of the estimated conductances is unperturbed (figure 3.5c, dashed lines).

3.3.3 Effect of attenuation on the power spectral density

So far we have only considered the effects of the morphology on the steady-state solutions. In the method for estimating the synaptic input effects at the soma from the previous chapter I have used power spectral density as one of the constraining factors.

In order to see how the morphology effects the power spectral density I studied the cable system of length l with one type of synaptic input at the location $x = sl$ on the cable, where $s \in [0,1]$. I expressed the power spectral density in the same way as for the point model but changed the membrane filtering factor (complex impedance) $Z(\omega)$ (Eq. 2.12) with the one I derived from the cable equation (3.1). The derivation follows the same process as the derivation of the input resistance for a finite-length cable with point synapses in the steady-state case where the differential equation we are solving

becomes

$$\frac{\lambda^2}{1+i\omega\tau}\frac{d^2v_i(x)}{dx^2} = v_i(x). \tag{3.35}$$

where ω is the input frequency and $\tau = r_m c_m$ is the characteristic time constant of the cable. The above equation follows from applying a Fourier transfer in the time domain on the original cable equation.

The resulting complex impedance is

$$Z(\omega) = \frac{2R_\lambda\lambda\beta e^{sL\beta}\left(e^{2sL\beta}+e^{2L\beta}\right)}{\langle g_s\rangle R_\lambda\lambda\beta\left(e^{2sL\beta}+e^{2L\beta}+e^{4sL\beta}+e^{2L(1+s)\beta}\right)+2(1+i\omega\tau)\left(e^{2L(1+s)\beta}-e^{2sL\beta}\right)},$$

where $\beta = \sqrt{1+i\omega\tau}$.

Figure 3.6 shows the comparison between the analytically derived values of the power spectral density (the dashed lines) and the power spectral density of the simulated membrane voltage on the cable of length $L = 2$ with the excitatory synaptic input ($V_E = 0mV$, $\tau_E = 2.5ms$) at various locations sl (solid lines, each color representing a specific location) simulated for 200 seconds. The timings of the inputs were drawn from a Poisson process. Beside a good match between the analytical solutions and the simulation results we see how the power spectral density is reduced for the inputs further away from the soma. This effect is much more pronounced for the higher frequencies (note that the y axis is logarithmic).

3.3.4 Attenuation effects on the full morphology

Attenuation effects for different types of morphologies

I studied the effects of the attenuation on the cases of real morphologies of neurons. Specifically I looked at the morphologies of three different neuron types - the Stellate cell, the Bitufted Cell and the Layer 5 Pyramidal cell. The cells were selected as their characteristic morphologies are fairly distinct (see figure 3.7). The stellate cell is small with a bushy dendritic arbor while the Bitufted cell is of similar size but with specific two-sided dendritic arbor. The Layer 5 pyramidal cell is bigger than the previous two with several dendritic branches around the soma (basal dendrites) and a fairly barren dendritic trunk extending to a secondary dense dendritic part (apical dendrites) further away from the soma.

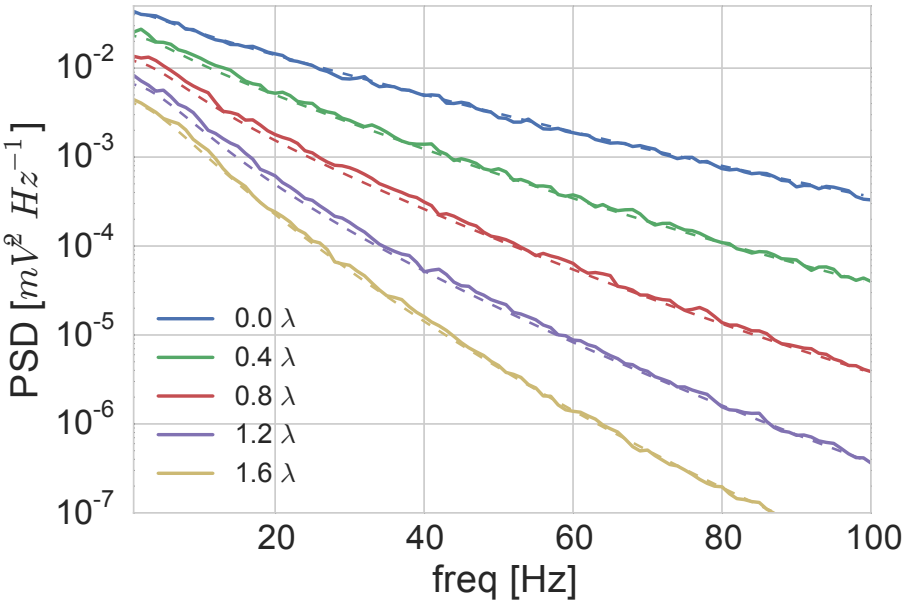

Figure 3.6: **The effects of morphology on the power spectral density** Power spectral densities of the membrane voltage for the cable with a synaptic input at different locations. The dashed lines represent the results of the analytical calculations and the solid lines represent the results from the simulations (the timings of the inputs were drawn from a Poisson process). The power spectral densities are reduced due to the attenuation effects of the morphology.

To investigate the effects of the attenuation I considered the case where the neurons are subjected to presynaptic activity from one type of synaptic input (excitatory) from (N=5000) synapses with the locations of the synapses chosen in four different configurations. In first configuration (soma) all the synapse are at the soma; In the second configuration (proximal) the synapses are located closer to the soma than one half of the maximum distance from soma; In the third configuration (uniform) the synapses are uniformly distributed along the dendritic tree; Fourth configuration (distal) is the one where all the synapses are located further than one half of the maximum distance from the soma. In the proximal, uniform and distal cases the actual locations of the synapses are distributed so that the probability that the synapse is located on a certain section of the dendrite is proportional to its length. The distribution of the synapses for all those cases (except the soma case) and all three cells are shown in figure 3.7. Due to the complexity of the problem I addressed the questions using numerical simulations as specified in the methods section (3.2.3.2).

Figure 3.8 shows the results of the simulations for all three cell morphologies (each morphology type in its own column) and all four synapse distributions (x axis). The top three plots show the ratio between the measured membrane input conductance change at the soma after the synaptic inputs of various strengths have been presented to the cell and the actual input conductance presented locally at the synapses. The input was changed by varying the input frequency of N=5000 synapses with a common strength and frequency (input times are drawn from the Poisson distribution) and was normalized to the input conductance at the soma when the input is not present for all three cell morphologies. I performed 10 simulations for each case and plotted the mean values (dots) along with error bars of 2 times the standard deviation. First we can see how the attenuation in the two smaller cell types (Stellate and Bitufted) have a considerably smaller level of conductance attenuation than the L5 Pyramidal cell. The attenuation is of course biggest for the synapse distribution where all the synapses are located away from the soma (distal) for all the cells. Also as expected from the results of the single synapse on the cable (see figure 3.3 b), the bigger the input conductance, the bigger the attenuation.

The bottom three plots show the the calculated α factor (Eq. 3.18). As we can see for the smaller cell types the calculated factor is always close to 1, which means the input to the soma is really mostly conductance based. For the L5 pyramidal cell this is not necessarily the case, as specially for the distant synapses with a strong level of input, the alpha factor drops to around 0.5, making those synaptic inputs a mixture of

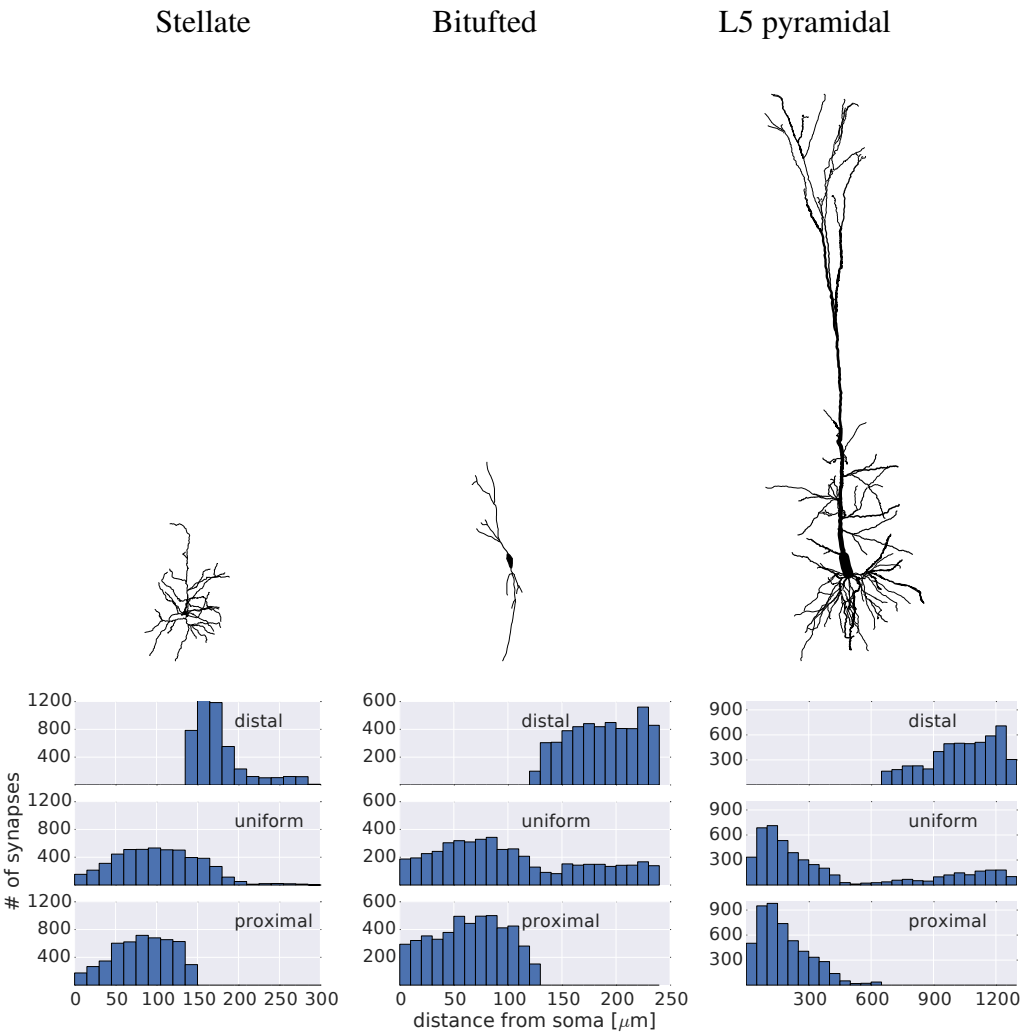

Figure 3.7: **Morphologies and synapse distributions:** (top) The morphologies of three types of cells examined. (bottom) The three distribution of synapses used in the simulations as a function of the distance from the soma (distal, uniform and proximal case). See the simulation methods section for the detailed explanation on how the synapses locations were chosen. Besides those three cases I also examined the case where all the synapses are located at the soma.

current and conductance based synapses. This means that the synaptic input delivered to the apical tuft of the pyramidal cells would increase the membrane voltage at the soma while at the same time not proportionally increasing the cell input conductance at the soma.

As I have shown before we can expect this to influence the synaptic input estimations based on the measurements obtained from the soma.

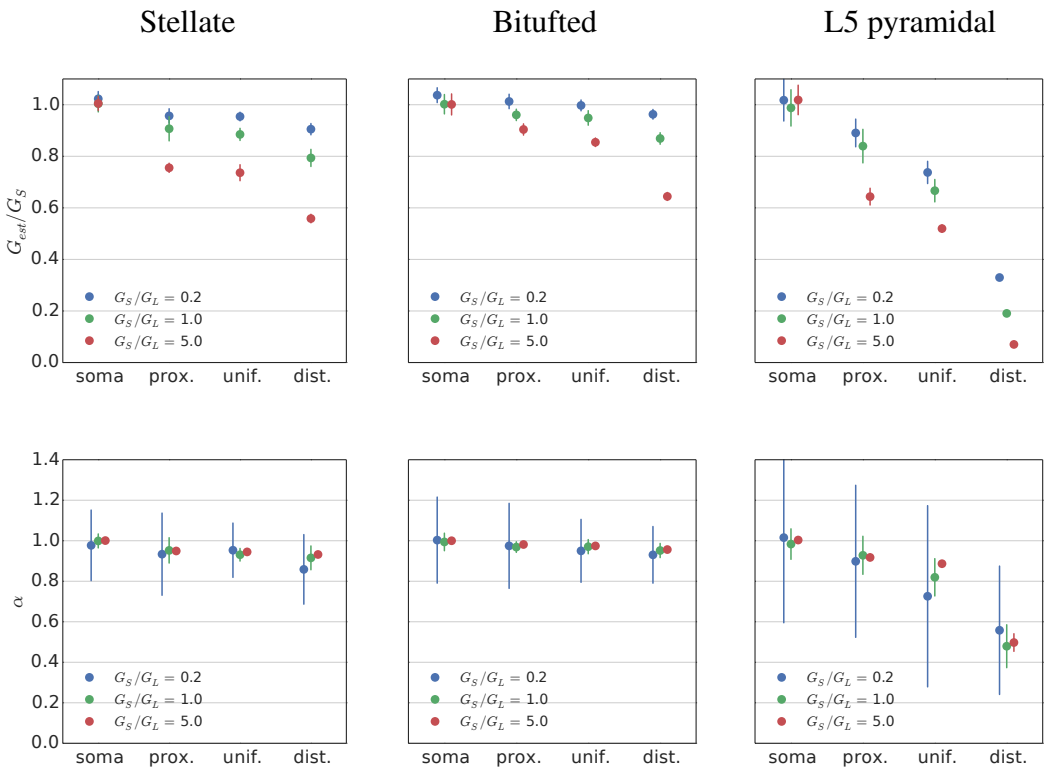

Figure 3.8: **The effect of morphology on the estimation of the conductance:** (top) The ratio between the measured membrane input conductance change at the soma for all three cell morphologies after the synaptic inputs of various strengths have been presented to the cell (for four different synapse distributions). The underestimation of the input conductance is expectedly bigger for the cases with the larger average distances of the inputs from the soma. It is also larger for stronger inputs. The effect is most obvious for the Layer 5 pyramidal cell. (bottom) Same as top, but for the calculations of the factor α. Here we see the factor only significantly changes in the Layer 5 pyramidal cell.

The excitatory and inhibitory misestimations for the case of a L5 pyramidal cell

Estimations of global excitatory and inhibitory input conductances based on the measurements from the soma are often reported in experimental studies (e.g. [24, 23, 27]). To determine how much those estimations can underestimate the actual synaptic input to the whole neuron in the case of the Layer 5 pyramidal cell, I performed a set of simulations including excitatory ($N_E = 5000$) and inhibitory ($N_I = 1000$) synapses. Again all the synapses of their respective type have the same properties as described in the methods section (3.2). The input strengths were scaled so that the time averaged total excitatory conductance was the same as the total inhibitory one.

As I have shown before (equations 3.19 and 3.20, figure 3.3), the effects on the soma will be dependent on the location of the synapses. First I looked at the case where the synapses of both types are distributed uniformly (same synapse probability per the unit of dendrite section length). The results for the varying strength of the synaptic conductance are presented in the top plots of figure 3.9. The simulation for each case was repeated 10 times with the synaptic locations and the exact times of presynaptic action potentials being randomly selected for every simulation. The plots show the mean value along with the confidence interval of one standard deviation. On the left plot we can see both conductances are underestimated. The excitatory conductance is estimated to be between 0.45 and 0.7 times of the true value while the inhibitory conductance is estimated to be between 0.55 and 0.35 times the real value, depending on the actual strength of the inputs, where the stronger the input, the more it is underestimated (figure 3.5). As expected from the results from the cable example with the excitatory and inhibitory synaptic input (section 3.3.2) the ratio between the estimated excitation and inhibition is above the real value for all cases.

Lastly I studied the more realistic synapse distribution [5]. While the excitatory synapses are still distributed uniformly, the inhibitory synapses are distributed proximally (all synapses closer to the soma than the one half of the maximum distance). The results are presented in the bottom part of the figure 3.9. This does not change the excitatory input estimation much, but the inhibitory conductance is now less underestimated (between 0.7 and 0.5 of the real value), leading to the ratio between the excitation and inhibition now switching in the favor of the inhibition for the strong inputs.

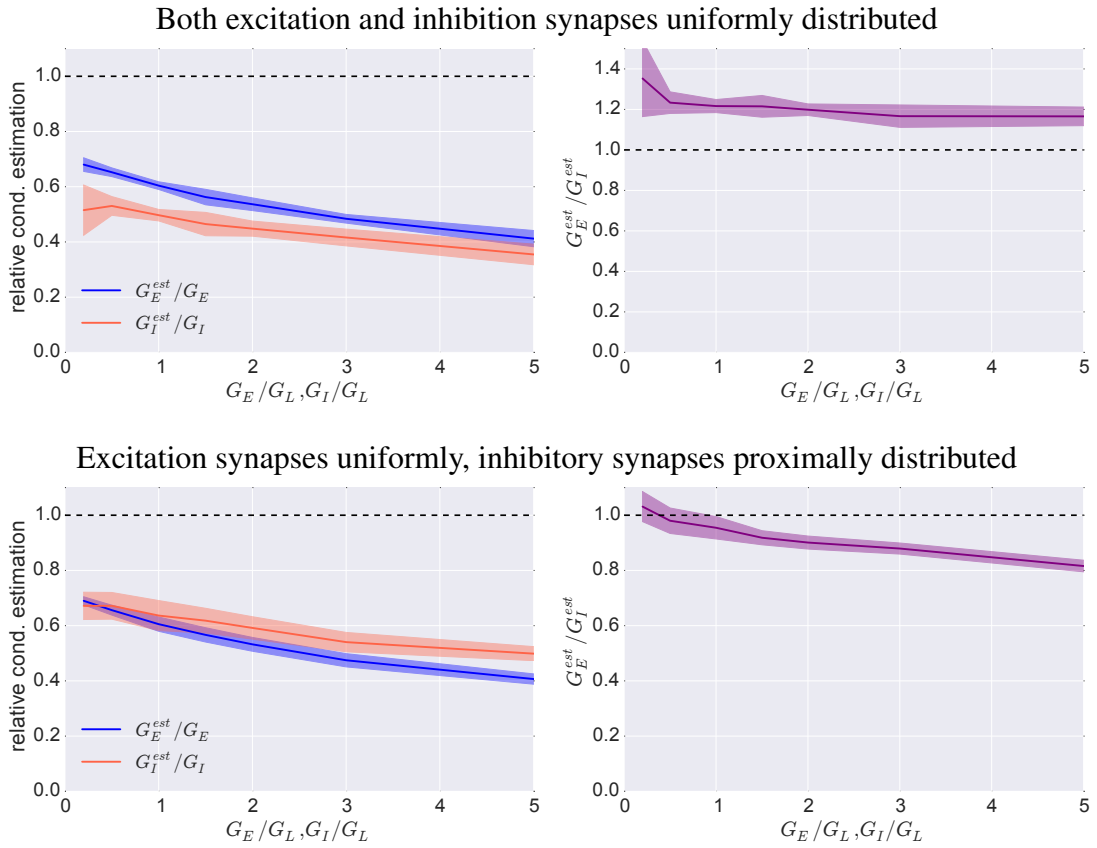

Figure 3.9: **Misestimations of the input conductances on the Layer 5 Pyramidal cells:** (top) The relative estimations of the excitation (blue) and the inhibition (red) for the simulations on L5 pyramidal cell morphology where the locations of the excitatory synapses ($N_E = 5000$) and the inhibitory synapses ($N_I = 1000$) are distributed uniformly across the dendritic tree. I vary the input conductance by changing the frequencies of the synaptic input events in a way that the average excitatory input conductance (G_E) is always same as the inhibitory input conductance (G_I). The left plot shows the relative estimations of excitation and inhibition as a function of the total synaptic conductance ($G_S = G_E + G_I$). If there was no bias due to the morphology, then we would expect all the values to be 1 (the dashed black line). The right plot shows the ratio between the estimated excitation and estimated inhibition. (bottom) Same as on the top but for a more realistic distribution of synapses where the excitatory synapses are again distributed uniformly while the inhibitory synapses are distributed proximally (see figure 3.7, bottom right).

3.4 Discussion

The fact that the synaptic inputs to the neuron are spatially separated from the soma leads to the modification of their effects as they are propagated along the dendritic tree to the soma. Both the membrane voltage change as well as the effect of the input conductance change are reduced. Those changes are important to synaptic input integration in neurons and also affect estimation of inputs based on intracellular recordings at the soma.

To examine this effect I first studied the simplified model of a homogeneous cable. This is a common reduction making it possible to treat the problem analytically and has been shown to be effective in capturing the electrotonic properties of passive neurons in the presence of synaptic background activity [7, 66]. I derived the expressions for the steady-state solution of the cable equation for two cases:

1. Single synaptic input at an arbitrary location on the cable;

2. A cable of length l with homogeneously distributed synapses.

As expected both the voltage and the conductance changes are attenuated in both cases and the attenuation increases with the input distance from the soma (1) or the total length of the cable (2). Interestingly the attenuation of the voltage change is weaker than the attenuation of the input conductance (only applicable for case 1). This difference is even more pronounced as we increase the input conductance, as the relative attenuation of voltage change is reduced while the conductance attenuation increases.

The effects of the morphology on the modifications of the steady-state values of membrane voltage and input conductance can be represented by the modified point models. One way to do so is to represent the synaptic input with the modified reversal potential. The absolute value of the new synaptic reversal potential relative to the leak reversal potential will always be higher than the value of the real synaptic reversal potential (Eq. 3.24). This is explained by the fact that the input conductance is attenuated more strongly than the membrane voltage change. The same amount of input conductance change is thus associated with a higher change of the membrane voltage as the synapse is further away from the soma. For case 1 the reversal potential only depends on the location of the synapse on the cable and not on the actual size of the input. As expected the modified reversal potential is equal to the real reversal potential when the synapse is located at the soma ($lim_{s\to 0}$ of equation 3.24).

Given that conductance change is more attenuated than the membrane voltage

change we can also present the synaptic input as a combination of a pure conductive input with the real synaptic reversal potential and the current based input (directly injected current only changing the membrane voltage but not the membrane input conductance) where a factor $\tilde{\alpha}$ represents the proportion of the conductive current. This split was initially proposed by Vogels et al. (COBA Vs. CUBA - COnductance Vs. CUrrent based synapses)[67, 59], where he demonstrates the importance of how synapses modified in this way influence the activity of the network of neurons. The further the synapse is from the soma (case 1) or the longer the cable with homogenous synapse distribution is (case 2), the smaller α is - the synapse becomes more current based. Interestingly in case 1, but not in case 2, $\tilde{\alpha}$ does not depend on the synapse reversal potential or on the synapse strength but only on the location of the synapse on the cable.

The point model representation of the morphology effects helps to form a better intuition of what are the effects at the soma and provides the basis for the more realistic neuron model simplification which can be then further used in the studies of the dynamics of single neurons [4, 68, 6] and neural networks [69, 70, 59, 71].

The attenuation not only affects steady-state values of the membrane voltage but also temporal aspects of the input integration. Observing the change of the power spectral density due to the attenuation we can see the change is more complex than the simple frequency independent reduction we would expect if the effect of the morphology were a simple time-independent reduction of the amplitudes of the post synaptic potentials. The higher frequencies are attenuated more strongly than the lower frequency.

Using numerical simulations I evaluated the steady-state effect of the morphology on the input integration for three different types of cell morphologies. While the effects for the smaller cell types (Stellar and Bitufted) were fairly small ($\tilde{\alpha} > 0.8$), the effects in the bigger cells such as L5 pyramidal cell were more pronounced, specifically for the more distal inputs ($\tilde{\alpha} \approx 0.5$). The inputs in the apical tuft of the layer 5 pyramidal cells are seen from the soma as a mix of conductance and current based inputs. This will affect the integration properties of the cell and needs to be considered in the theories of the cortical input processing specifically since we know that the input from other cortical regions is primarily located on the dendritic tuft of those cells.

We could notice how the attenuation leads to the misestimation of the input conductances when estimating the input by measuring the membrane voltage and input conductance differences at the soma. Not only does the attenuation cause an underes-

timation of the excitatory and inhibitory conductances but it can also lead to misestimation of the ratio between the excitatory and inhibitory conductance. I first studied this in the case of a cable with an inhibitory and excitatory synapse located at the same point on the cable, for which I derived an analytical expression. We saw how the naive input estimation could even lead to negative estimations of input excitation or inhibition in extreme cases.

Finally I assessed the estimation error for the case of a real morphology (Layer 5 pyramidal cell) using numerical simulations. When the actual synaptic input conductances were of the same strength for both types of inputs, each was estimated to be about one half of the real value with the excitatory conductance being less underestimated. The relative underestimation is bigger the stronger the input. When I looked at the case with the synapse distributions more like what is observed in the brain, I found a similar effect. The difference here was that the ratio between the estimated conductances now favored the inhibition. In the Chapter 5 the specific implications of this findings to the estimation results of the previous chapter are discussed.

The results of this chapter are relevant both for the experimental as well as the modeling community. As Vogels showed, the mixture of the conductance and current based synapses defines the behavior of the neural networks and the right mixture of conductance and current based input should be used when devising simplified models [59]. Given the information on the preferential location of the inputs on the dendritic tree my results give a way to adjust those mixtures, where the ratio between the current and conductive part could be different for the same postsynaptic neuron for the inputs coming from different locations.

For the experimental community the results here give a better idea of how the inputs to the neurons are underestimated given the intracellular recordings from the soma and application of the standard estimation techniques [23, 24, 30]. Additionally the results show how the excitation and inhibition are underestimated differently so that their ratio can be misestimated. I discuss the implications of this study on the experimental estimations from the previous chapter in the final chapter of the thesis (chapter 5).

Experimentally estimated differences of global input excitation or inhibition can not only result from the actual changes in the global amount of excitation or inhibition, but also from the change of the location of those inputs on the dendritic tree. This shows the importance of the synapse location which is a topic of the next chapter.

Chapter 4

Input location estimation from EPSP shape measurements[1]

4.1 Introduction

Determining the connectivity between the neurons is widely believed to be a crucial ingredient in understanding the workings of the brain. As I have shown in the previous chapter the location of the synapse on the dendritic tree plays an important role in the way the synaptic inputs are integrated. It is thus not only important which neurons are connected to each other, but also where specifically on the dendritic tree of the post-synaptic neuron the synapses forming those connections are located.

Voltage-dependent synaptic receptor channels (e.g. NMDAs [20]) make this even more important. These are channels which open in the presence of neurotransmitters only if the membrane voltage is high enough. This can lead to non-linear responses in the input, and several proposals for more complex input integration mechanisms based on those non-linearities have been proposed [17, 72], suggesting the neuron can be a more complex information processing unit than a simple non-linear integrator. For example, each dendritic branch of a neuron could be doing a specific type of computation [9, 73]. Specifically, Larkum et al. [17] suggest a two-stage input integration in Layer 5 pyramidal neurons, where in the apical tuft of the cell inputs are first integrated and can cause a calcium spike at the calcium initiation zone, which is then integrated together with the excitatory inputs at the soma or basal dendrites in the second step.

Experimentally determining the exact synaptic locations is a challenging task. One

[1] All the experiments described in this chapter were performed by Mihael Zohar from Freiburg University.

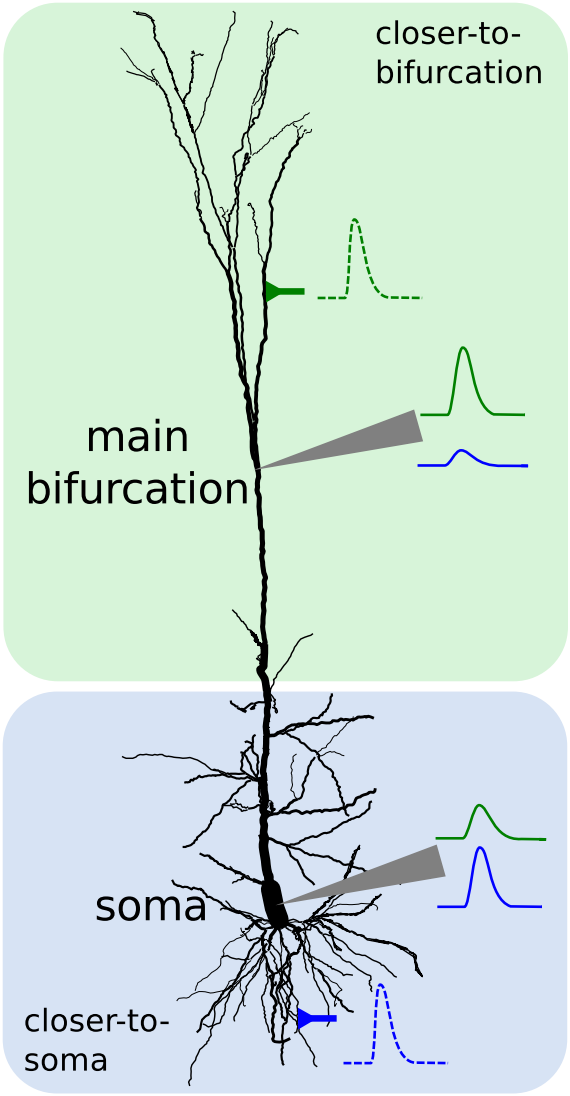

Figure 4.1: **EPSP attenuation in a cell:** A morphology of the Layer 5 pyramidal cell [57] from a somatosensory cortex with intracellular recordings at two locations (gray triangle). The membrane voltage is simultaneously measured at the soma and at the main apical bifurcation to detect the membrane deflection caused by a synaptic input (EPSP - excitatory post-synaptic potential). As the EPSPs are attenuated as they propagate along the dendritic tree, the recordings at the two locations are different (blue and green traces). Based on those differences we aim to determine whether the synapse causing the EPSP is located in the region close to soma (blue shade - closer-to-soma) or in the region closer to the main apical bifurcation (green shade, closer-to-bifurcation).

method of doing it is by recording from the presynaptic and postsynaptic neuron, filling them with a dye and then determining the connectivity by examining morphological reconstructions after fixating the tissue [74, 75]. As the probability of the connectivity between two random cells can be very low, this method requires patching from many cell pairs to find a connected pair. Combining this with a time-consuming manual morphological reconstruction makes this method less appealing (but not impossible, see [76, 77]). Another possibility is to employ volume electron microscopy techniques to image slices of the neural tissue with high spatial resolution and then reconstruct the full axons, dendrites and synapses within the imaged volume [78, 79, 80]. While this gives a full connectivity profile within the volume, the volume reconstruction technique is very difficult and time consuming and has thus mostly only been applied to small volumes of tissue.

In this chapter I describe an alternative attempt to determine the location of the synapse on the dendritic tree of layer 5 pyramidal cell using the excitatory postsynaptic potential (EPSP) shapes, measured from two different locations on the neuron – soma and the main apical bifurcation (see figure 4.1). EPSPs change their shape as they propagate along the dendritic tree due to filtering so the difference of the shapes at the two locations is informative of the location of the synapse.

The change of EPSP shape is presented on a simplified three compartment model in figure 4.2. We introduce a conductive change mimicking the synaptic input at one compartment (either soma or tuft) and measure the membrane voltage deflection at both compartments. As the EPSPs propagate along the dendritic tree their size is decreasing (it attenuates). This attenuation is typically not symmetric as we can see in the bottom part of the figure 4.2 where EPSP propagation is simulated on a simplified morphology. The size of the compartment will determine the input resistance so that the same input conductance will cause a bigger or smaller EPSP resulting in an apparent smaller or bigger attenuation in one or the other direction.

The method of comparing the EPSPs from two locations typically does not allow to exactly localize the synapse but rather to determine the region in which the synapse is located. In this chapter I construct and evaluate the performance of an automatic classifier which classifies the synaptic location either as belonging to a region closer-to-soma (blue background in figure 4.1) or to the region closer-to-bifurcation (green background in figure 4.1). I build the classifier based on the recorded EPSP pairs which were labeled as either closer-to-soma or closer-to-bifurcation by the experimenter using his domain specific expert knowledge. Finally, I construct another classifier using

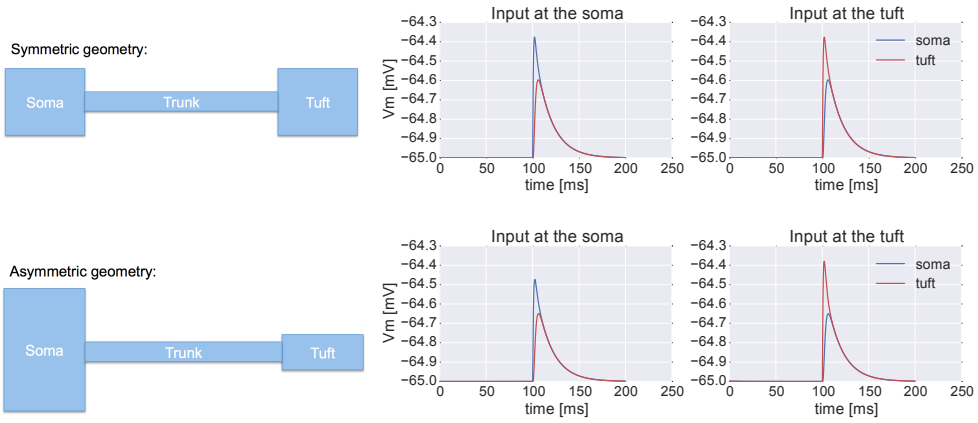

Figure 4.2: **Asymmetric attenuation:** Simplified morphology with three compartments (soma, apical trunk and apical tuft) shows how the measured attenuation can be asymmetric.

(top) In the case of symmetric morphology (somatic compartment is the same size as the apical tuft compartment) the size of EPSP caused by the injection of excitatory conductance at the soma measured at the tuft is the same as the size of the EPSP originating from the tuft and measured at the soma.

(bottom) Same as above but with altered morphology. The radius of somatic compartment is increased 2-fold while the radius of tuft compartment is reduced 2-fold. Given the same size of input conductances this change leads to a smaller EPSP measured at the soma when the input is located at the soma and the bigger EPSP measured at the tuft when the input is located at the tuft (due to changed input resistances). The apparent attenuation of the EPSP is then asymmetric.

a collection of simulated EPSP pairs on a general model of a layer 5 cell and compare the classification results with the classification of the expert.

4.2 Methods

4.2.1 Experimental setup

All experiments were performed by Mihael Zohar. The experimental data comes from *in vitro* whole-cell patch-clamp recordings combined with presynaptic dynamic photo stimulation [81] (Figure 4.3) in parasagital slices of the somatosensory cortex of young adult rats (P-18 - P-36). The slices in the setup are bathed in caged glutamate solution. The focused UV laser light beam cleaves the caging group off the glutamate and thus frees it. The freed glutamate can then bind to the nearby neurons and drive them above threshold to fire an action potential.

A chosen layer 5 pyramidal cell is patch-clamped at the soma and the apical trunk (the postsynaptic cell). Targeted laser stimulation is then used to excite the tissue around the patched postsynaptic cell. Membrane voltage response of the postsynaptic cell is recorded at the soma and at the main bifurcation simultaneously. The aim of stimulations is to excite presynaptic excitatory cells while avoiding direct stimulation of the patched postsynaptic neuron (either a synapse or the neurites). The recorded voltage responses in those cases are excitatory synaptic potentials (EPSPs). They allow us to study the relation between the synaptic properties and the location of the presynaptic neuron which can be in any of the cortical layers. A response to the direct stimulation would be uninformative as it would be shaped by the dynamics of the glutamate uncaging (instead of the glutamate release from a presynaptic neuron) and could be at least partially evoked by the opening of extrasynaptic receptors (which could differ from the synaptic receptors).

Stimulation locations where a presynaptic neuron would be excited are chosen to cover the area around the postsynaptic neuron avoiding the stimulation locations where the postsynaptic neuron would be directly stimulated (scanning of the slice). The setup allows fast switching between the focus location of the beam (up to 300 locations per second) which allows 2-5 recordings at the same stimulation location before the quality of the recording setup decreases. More details about the method including control experiments are described in [81, 82, 83].

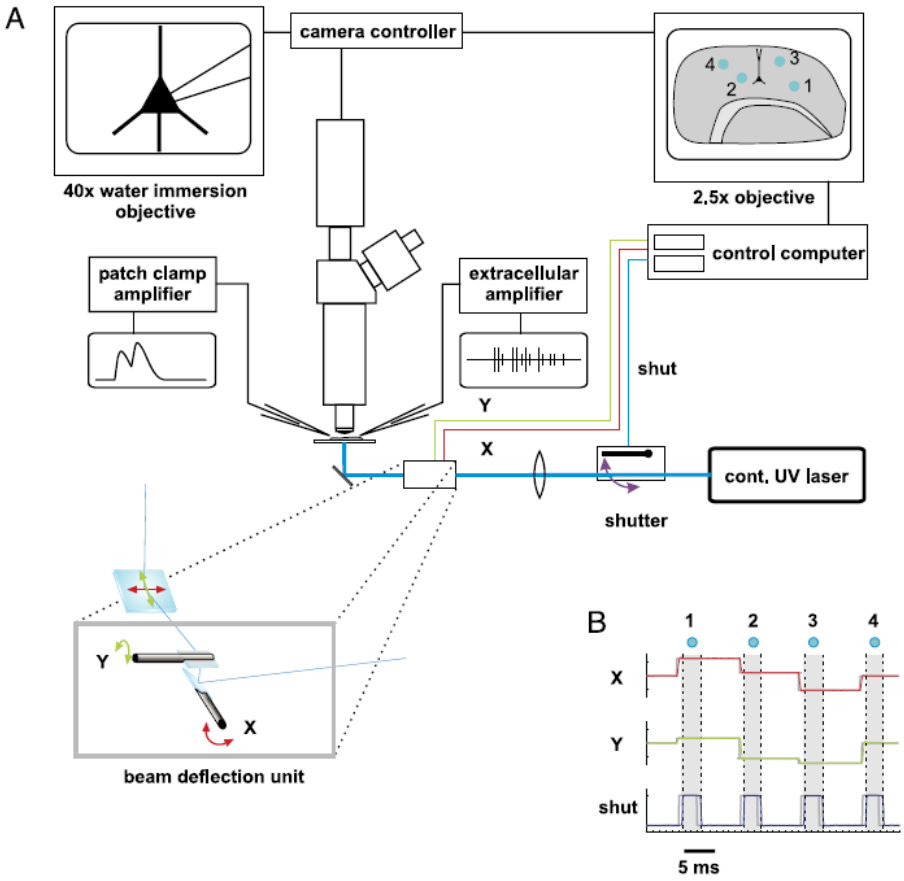

Figure 4.3: A: schematic diagram of the setup for dynamic photo stimulation. A conventional fixed-stage upright microscope is equipped with an *in vitro* recording chamber that has a UV-light permissive quartz-glass bottom, through which the laser beam for photolytic release of the caged compound is projected onto the tissue. Beam deflection is achieved through 2 scanning mirrors (inset). A 3rd mirror is used to redirect the laser beam into the recording chamber and replaces the condenser required for high magnification IR video microscopy to establish the single-cell recording. During dynamic photo stimulation, the slice can be observed through a long distance, low magnification objective (2.5). Light pulse duration is controlled by means of a programmable shutter. The membrane voltage is recorded at two locations - at the soma and the main apical bifurcation (not shown). B: time-course of mirror and shutter movements. A feedback control signal provided by each of the galvanic scanner elements allows a precise online monitoring of the actual target position X (red) and Y (green) and of the open and close times of the shutter (blue). Gray curves represent the respective command signals issued by the control computer. Numbers refer to different stimulated target positions during 4 completed duty cycles, as symbolized in the low magnification sketch in the top right corner of A. Figure taken from [81] and does not exactly represent our experiment where instead of the extracellular pipette shown in the figure another patch-clamp pipette is used.

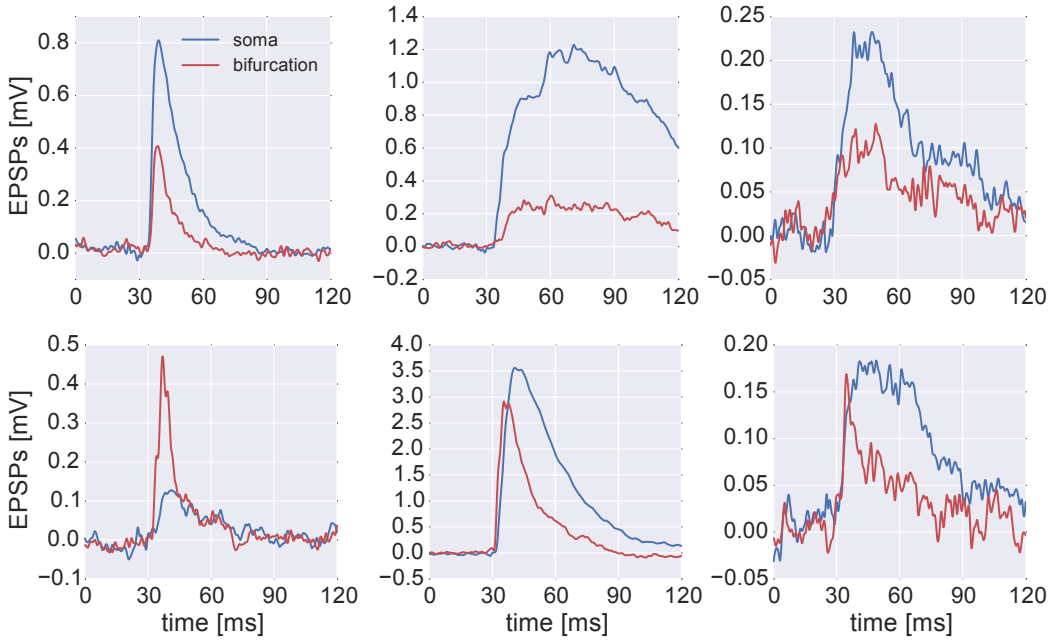

Figure 4.4: **EPSP pairs obtained from the recordings**: Examples of the averaged membrane voltage response at the soma (blue) and at the main apical bifurcation (red) to stimuli at 6 different locations around the recorded post-synaptic neuron. All 6 responses were identified as synaptic responses by the experimenter with the top three labeled as the responses belonging to a synapse located in closer-to-soma region and the bottom three to a synapse located in closer-to-bifurcation region. Note that the y scale is different for each case so the responses exhibit a variety not only in shapes but also in sizes.

4.2.2 Data processing and manual classification

Voltage traces recorded at location of the soma and main bifurcation of the apical dendrite (see figure 4.1) following a photo stimulation at a certain stimulus location are low-pass filtered with a cut-off frequency of 500Hz. Each individual stimulation location response trace is recorded 3 times and then averaged to obtain the pair (soma/bifurcation) corresponding to a specific presynaptic location. Example response pairs are shown in Figure 4.4.

For the dataset used to develop an automated classification method the recorded response trace pairs were manually labeled by the experimenter as either:

- **unconnected** - the stimulation produced no response in the recorded neuron.
- **direct stimulation** - the photo stimulation has hit the postsynaptic neuron di-

rectly so the response is not a synaptic EPSP.

- **closer-to-soma synapse** - the photo stimulation has elicited an action potential in a presynaptic neuron which forms a synapse with the recorded neuron at the location likely closer[2] to the soma than the main bifurcation on the apical dendrite. This includes the soma, basal dendrites and part of the apical trunk.
- **closer-to-bifurcation synapse** - the photo stimulation has elicited an action potential in a presynaptic neuron which forms a synapse with the recorded neuron at the location likely closer[2] to the main bifurcation on the apical dendrite than the soma. This includes the apical tuft and part of the apical trunk.

Labeling is done based on the experimentalist's domain knowledge assessing the EPSP features such as the relative EPSP onsets, rise times, peaks. In particular, we have no ground truth about the actual synaptic location in this experiment.

4.2.3 Classification using linear support vector machines

Linear support vector machines are designed to find the optimal separating hyperplane between the two classes of multidimensional vectors of dimension m.

Given a set of n instance-label pairs $(\mathbf{x}_i, y_i)$, $\mathbf{x_i} \in \mathbf{R^m}$; $i = 1,2,\ldots,n$; $y_i \in \{-1,1\}$ it aims to find weights and bias ($\mathbf{w} \in \mathbf{R^m}$, $w_0 \in R$ respectively) such that

$$\mathbf{w}^T\mathbf{x}_i + w_0 \geq 1 \quad \text{if} \quad y_i = 1, \tag{4.1}$$

$$\mathbf{w}^T\mathbf{x}_i + w_0 \leq -1 \quad \text{if} \quad y_i = -1, \tag{4.2}$$

which can be rewritten as

$$y_i(\mathbf{w}^T\mathbf{x}_i + w_0) \geq 1. \tag{4.3}$$

It tries to find a hyperplane that separates the two classes in a way that maximizes the margin between the hyperplane and the instances closest to the hyperplane. In this way it is defined only by the subset of instances closest to the hyperplane.

In the case when there exists no linear separation (it is impossible to find a hyperplane exactly separating the instances of both classes), the problem is redefined to an

[2]Here the word closer corresponds to the electrotonic distance rather than to the actual geometric distance.

optimization problem that minimizes the separation error. This is achieved by solving the following unconstrained optimization problem

$$\min_{\mathbf{w}} \left[\frac{1}{2}\|\mathbf{w}\| + C \sum_{i=1}^{n} \xi_i(\mathbf{w}, w_{0,}\mathbf{x}_i, y_i) \right], \tag{4.4}$$

where the second term is the error term and C is the error coefficient ($C > 0$) and ξ is the loss function. While different loss functions can be defined in this chapter I used the square loss function $\xi_i(\mathbf{w}, w_{0,}\mathbf{x}_i, y_i) = \left(\max(1 - y_i(\mathbf{w}^T\mathbf{x}_i + w_0), 0)\right)^2$.

In situations when the training set used in the optimization is unbalanced – the number of instances belonging to one class is bigger than the other – we can introduce the class-based weights ($c_{y_i} > 0$) to the error term to balance the contribution of each class to the error term. The optimization problem 4.4 then becomes

$$\min_{\mathbf{w}} \left[\frac{1}{2}\|\mathbf{w}\| + C \sum_{i=1}^{n} c_{y_i}\xi_i(\mathbf{w}, w_{0,}\mathbf{x}_i, y_i) \right]. \tag{4.5}$$

In the testing phase, we predict an instance $\mathbf{x}_i$ as belonging to class $y = 1$ if $\mathbf{w}^T\mathbf{x}_i + w_0 \geq 0$, and to the class $y = -1$ otherwise. Although it is possible to use the same set of instances for training the classifier (solving the optimization) as for evaluating it (doing the prediction), it is better to split the two to test the true quality of the classifier as we are interested in how good it is in predicting the unseen instances.

In this chapter I used the C implementation of the method from the LIBLINEAR library [84] as a part of the Scikit-learn package [85], using the square loss function, $C = 0.1$ and c_y in a way that $c_y \propto \frac{1}{n_y}$ where n_y is the number of training instances for each class y (balanced error).

4.2.4 Cross-correlation

To calculate a cross-correlation of two traces a discretized form of the expression

$$cc(\tau) = \int_{-\infty}^{\infty} \hat{f}_{bif}(t)\hat{g}_{soma}(t+\tau)dt \tag{4.6}$$

is used, where cc is the cross correlation and $\hat{f}_{bif}$ and $\hat{g}_{soma}$ are normalized traces recorded at the bifurcation and the soma respectively. The normalization is a z-score

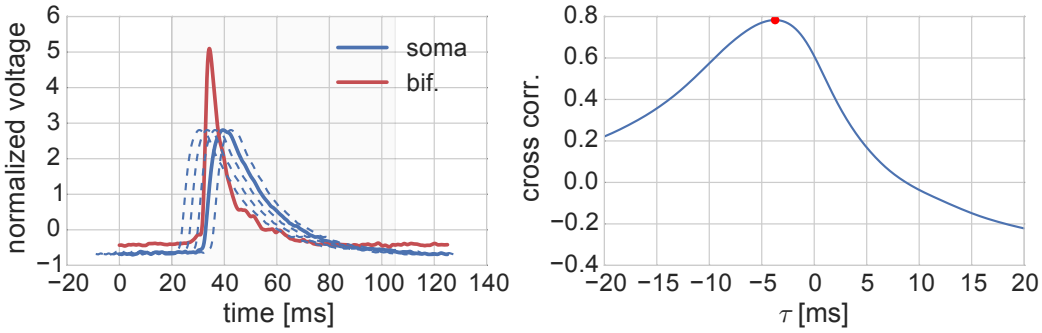

Figure 4.5: **Cross correlation example:**
(left) An example pair of recordings. The trace measured at the main apical bifurcation (red solid line) and the trace measured at the soma (blue solid line) are normalized. To calculate the cross-correlation we introduce a time lag (τ) to the somatic trace and integrate the product of the two traces in the time range of [20ms - 105ms] (gray area). (right) The cross correlation as a function of the time lag τ. The red dot shows the maximum of the cross correlation function (at $\tau = \tau_m$). Time lag corresponding to the maximum of the cross correlation (τ_m) is the indication of whether the synaptic location was in a closer-to-soma or a closer-to-bifurcation region. We would expect the closer-to-bifurcation location to have lesser τ_m than the closer-to-soma one, with a certain value separating them.

($\hat{f}_{bif}(t) = (f_{bif}(t) - \langle f_{bif}(t) \rangle)/std(f_{bif}(t))$, where $\langle . \rangle$ is the average and $std(.)$ is the standard deviation over the 125 ms of the trace).

More specifically we are interested in the τ_m - a time lag of the somatic trace at which the cross correlation reaches the maximum value ($\tau_m = \text{argmax}(cc(\tau))$. As I expect to see the maximum close to $\tau = 0$, I constrain the calculation to the limit within ± 20 ms. I truncate the bifurcation trace for 20 ms on both sides, let the lag of the somatic trace (τ) run in the range of [-20ms, 20ms] and integrate the product of the traces in the truncated interval (See figure 4.5).

The truncation ensures that both traces are defined in the full integration interval. Alternatively I could avoid truncation of the bifurcation trace and integrate over the full length of the trace by substituting the undefined time-points on the somatic trace by zeros (zero-padding). This would however introduce a bias towards $\tau_m = 0ms$ where the zero padding is not needed.

4.3 Results

In this study, we looked at the relation between the location of the presynaptic neuron and the location of the synapse on the patched postsynaptic neuron. The location of the synapse is not known directly from the experiment but must be estimated based on the membrane voltage responses at the two recording locations (at the soma and at the main bifurcation). Our goal was to construct an automatic classifier which would be able to determine whether the location of the synapses is in the region closer to the soma or the region closer to the apical tuft of the patched layer 5 neuron.

4.3.1 Problem definition

Due to the attenuation during the propagation of the EPSPs along the dendrites, the measured shape of a specific EPSP is different in different locations. Given recordings at two locations, one at the soma and the other at the main bifurcation of the apical dendrite, we tried to infer the general location of the synapse. To characterize the shapes I defined a set of features which are automatically extracted from each EPSP trace. The set includes the size and timing of the peak, the onset and offset times of the EPSP, the rise time and the slope and area under the EPSP curve (the detailed definition of the features is listed in section 4.3.2).

The EPSPs caused by different synapses are expected to have different shapes due to the attenuation (e.g. see figure 4.2). Due to this we can expect that a difference in the EPSP shapes recorded at two different locations would give an informative measure as to the location of the synapse. If we knew that the synaptic inputs at different locations on the neuron are distinguishable (e.g. that the synaptic inputs at the soma would have a characteristic temporal features), we could use it to infer the locations. However, to our knowledge there is no such distinguishable characteristic so we have to rely on the difference in EPSP shape measured at different locations.

However, it is unrealistic to expect to be able to determine the exact synaptic location by the difference in the shapes due to the fact that the dendritic trees are branched. This for example means that even in theory we are not able to distinguish between the synapse located on two different branches of the apical tree which have the same attenuation profile on the path to the main bifurcation (and same for the branches of basal dendrites). We can however expect to be able to detect the difference between the synapses at the apical tuft and the synapses at the basal dendrites. Our realistic task is then to construct a way of classifying the synaptic contacts indirectly detected by the

experimental setup into either the **closer-to-soma** (located at the basal dendrites, soma or on the apical trunk close to the soma) or **closer-to-bifurcation** synapses (located at the apical tuft or apical trunk close to the main bifurcation).

4.3.2 Feature extraction

An excitatory postsynaptic potential (EPSP) has a characteristic shape. Starting from the baseline voltage the membrane potential initially increases rapidly until it reaches peak membrane voltage. After that the voltage slowly returns back to the baseline value. The exact shape of the measured EPSP depends on the synapse properties (neurotransmitter release and diffusion properties, receptor density and dynamics), on the input impedance properties of a postsynaptic neuron at the location of the synapse and on the filtering by the propagation of the EPSP from the initiation location to the recording location. The difference between the shape of the EPSP initiated by the same presynaptic action potential measured at the two different locations can thus be attributed only to the change caused by the propagation along the dendrites. We can thus use the difference in the EPSP shapes to infer the approximate location of the synapse.

One way of describing the shape of the measured EPSP is to define a set of features describing it and extract those features for each recording. I define the following features depicted in Figure 4.6:

- **The EPSP peak voltage**: The maximum value of the recorded membrane potential in the period of 30 ms after the stimulus onset relative to the mean voltage in 25 ms before the stimulus onset. Peak voltage must be significantly higher than noise fluctuations in the recording to be considered as a good EPSP (bigger than 3 times the value of the standard deviation of the membrane voltage in the 25 ms before the stimulus onset). Note that this condition will remove the smaller EPSPs, specially in the recordings which are particularly noisy.

- **The EPSP peak time**: Time of the EPSP peak (relative to the photo stimulation onset).

- **The EPSP onset time**: Time at which the membrane voltage reaches 20% of the peak value (relative to the photo stimulation onset).

- **The EPSP offset time**: Time at which the voltage returns to 20% of the peak value after reaching the peak (relative to the photo stimulation onset).

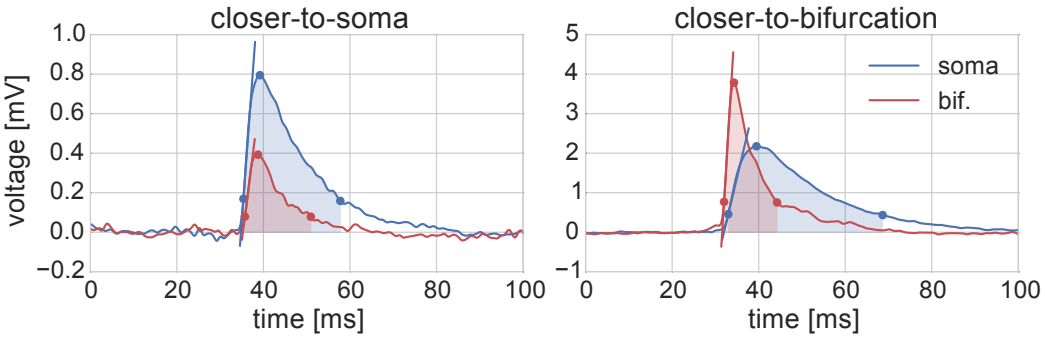

Figure 4.6: **EPSP features:** Two stimulation response measurements where the responses were either labeled as closer-to-soma (left) or as closer-to-bifurcation (right). For each pair the blue trace is the average of membrane potentials recorded at the soma and the red trace is the average of membrane potentials recorded at the main bifurcation at the beginning of the apical dendritic tuft (see figure 4.1). The dots represent automatically extracted onset, peak and offset times. The lines represent the estimated EPSP rise slope and the shades under the traces define the EPSP area feature.

- **The EPSP rise time**: The time between the EPSP onset time and the moment the membrane potential reaches 80% of the EPSP peak voltage value.
- **The EPSP rise slope**: A linear approximation of the EPSP rise slope in the time interval between the time 20% and the time 80% of the peak voltage was reached (rise time); It is calculated as 60% of the EPSP peak voltage divided by the rise time.
- **The EPSP area**: Area under the EPSP in the time between the EPSP onset and EPSP offset calculated as a numerical integral of the EPSP potential between the onset and offset time.

The process of feature extraction on the experimental dataset was automated. EPSP pairs were excluded from the further analysis if for the EPSP at either location:

- the peak was too small (below 3 times the value of the standard deviation of membrane voltage in 25 ms before the stimulus onset).
- it was not possible to estimate the offset time (the voltage does not drop under the 20% of the peak value in 100ms after the stimulation).
- it was not possible to estimate the rise slope as the estimated rise time was 0 (the voltage value of the first data point after the stimulus onset was over 80% of the

peak value).

4.3.3 EPSP features in surrogate data

In order to understand how EPSP features could be distributed I performed simulations on a detailed morphological model of a layer 5 somatosensory cell of a rat. I chose 300 random locations on the dendritic tree and stimulated the neuron with a conductance-based excitatory input.

As in the previous chapter the simulations were performed using the NEURON simulation environment [60] with the default Backward Euler integration method. Specifically I used a neuron model of a Layer 5 pyramidal cell from the somatosensory cortex of a rat [57] including the passive membrane properties only (described in more detail in the chapter 3), since all the simulations stay in the voltage regime under the firing threshold where most of the voltage-dependent channels (active channels) are closed.

A simulator is solving the cable equation on the morphology of the cell depicted in Figure 4.1. 300 different locations on the neuron were selected and used to stimulate the neuron (one synaptic input at the time) by injecting a conductance-based input in a shape of an double exponential function with time constants $\tau_1 = 0.2$ ms $\tau_2 = 1.7$ ms [42]. I varied the amplitudes of the stimulations to produce the EPSPs of a size up to 6mV at the soma and up to 9 mV at the apical bifurcation.

Figure 4.7 shows the spreads of the differences of EPSP features between the traces recorded at the soma and the traces recorded at the main apical bifurcation. Each point corresponds to a specific pair of recordings (specific synaptic location) and is colored according to the location of the synapse with respect to the soma or the main apical bifurcation. If the synapse is closer to the soma than to the main apical bifurcation (in closer-to-soma region), the corresponding point is blue, otherwise the point is green (in closer-to-bifurcation region).

The distributions of EPSP feature differences between the closer-to-soma and closer-to-bifurcation groups are fairly distinct for most of the features, which is promising for using them as the features of the classification algorithm that we apply to the dataset recorded from the experiment.

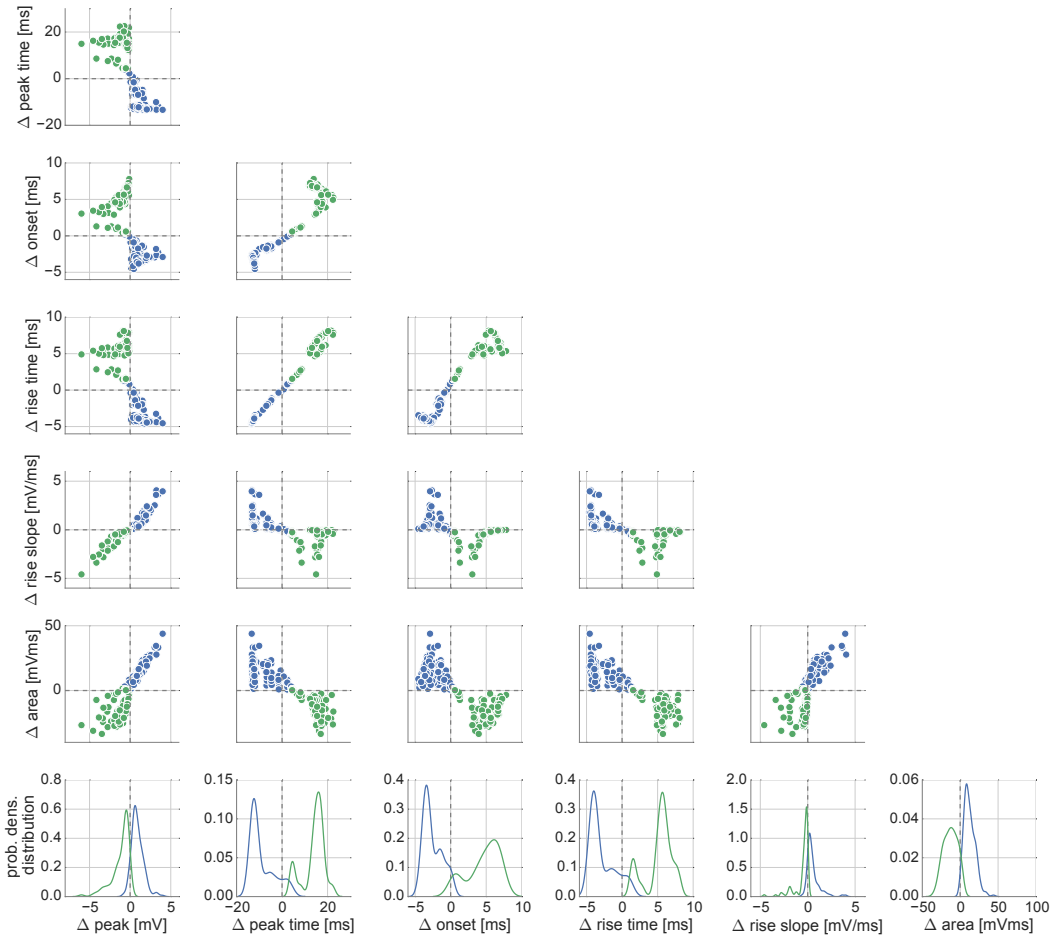

Figure 4.7: **EPSP feature differences in the simulated set:** Scatter plots of the differences in EPSP features between the EPSP recorded at the soma and the EPSP recorded at the main apical bifurcation for a case of the simulated model. Each point represents a simulated conductive input at a specific location on the dendritic tree. If the location is closer to the soma than to the main bifurcation (in closer-to-soma region), the point is blue, otherwise the point is green. The plots in the bottom row present the kernel density estimation-based distributions for all the feature differences in both groups.

4.3.4 EPSP features in the labeled dataset

In order to construct and test the classification methods we used an example from a single recording session where the EPSP pairs were labeled by the experimenter. Our dataset includes 556 pairs of recordings averaged over 3 trials, each corresponding to a different presynaptic stimulation location. 342 of those were labeled as unconnected by the experimenter and 5 as direct stimulation – the stimulation location corresponds directly to a location of one of the dendrites of the recorded neuron and the uncaged glutamate directly opens the glutamate receptor channels (which could be synaptic or extra-synaptic).

The remaining 209 pairs are thought to be the result of a true synaptic excitation, where the presynaptic neuron fires an action potential as a result of a stimulation with the uncaged glutamate. Those pairs were split in two groups based on the visual differences between the response trace measured at the soma and the response trace measured at the main bifurcation at the beginning on the dendritic tuft. 193 of the response pairs were labeled as **closer-to-soma**, suggesting the synapse is located closer to the soma and 16 as **closer-to-bifurcation**, suggesting the synapse is located close to the main bifurcation.

A further 11 closer-to-soma pairs were removed from the dataset as they did not pass the criteria for the feature extraction (see feature extraction section in the methods for details) leaving us with a dataset of 182 closer-to-soma and 16 closer-to-bifurcation EPSP pairs.

Figure 4.8 shows the distribution of the EPSP feature differences in the labeled dataset. Differences in the distribution for all the features are much less distinct between the two cases compared to the simulated data. Furthermore we can see some distinct outliers, specifically for the onset time and rise slope features. Those are the features most susceptible to noise in the recordings. As we will see later, specially for the small EPSPs the signal to noise ratio can become very small.

4.3.5 Spontaneous apical EPSPs

Another source of information on the attenuation of EPSPs in the neuron can be obtained from the spontaneous EPSPs measured during the experiments. Those are the EPSPs which occur in the absence of any stimulation. They are either the result of spontaneous activity present in the tissue or the result of spontaneous neurotransmitter release from a single synaptic vesicle in the presynaptic neuron in the absence of an

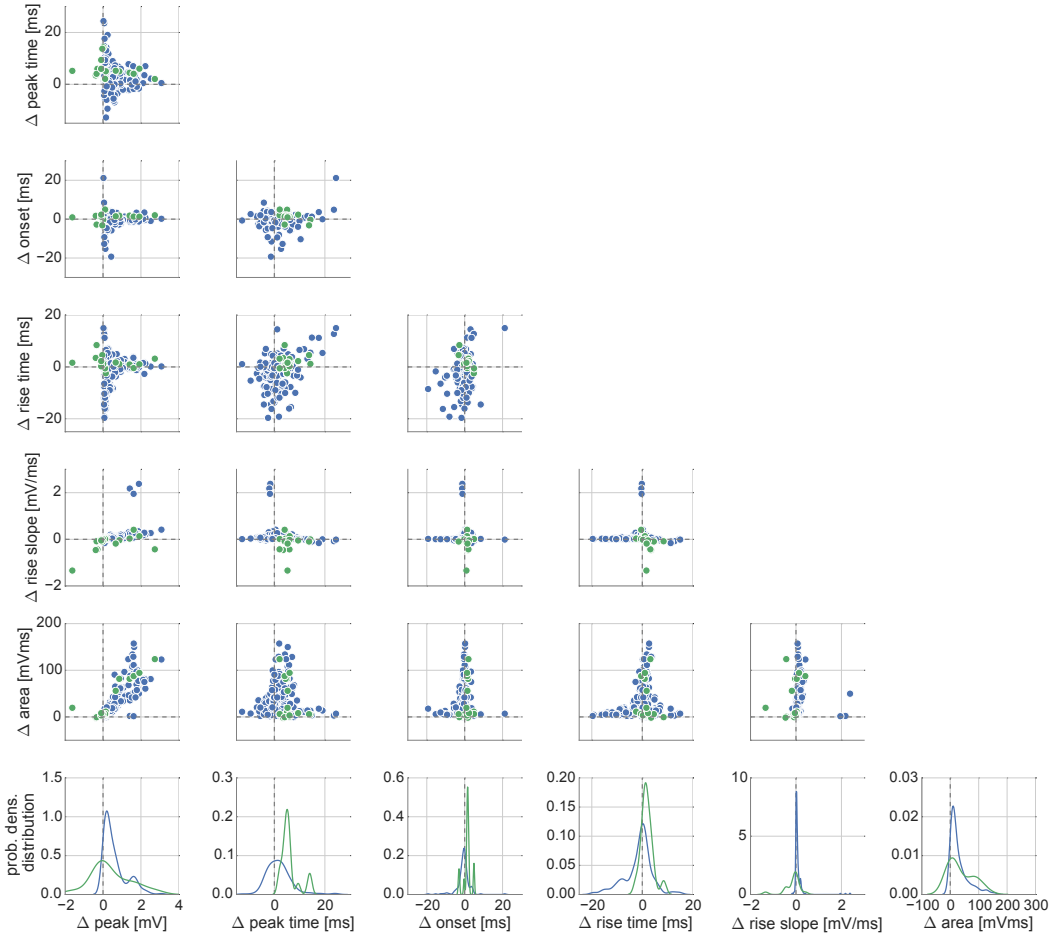

Figure 4.8: **EPSP feature differences in the labeled dataset:** Same as figure 4.7, but this time presenting the results from the experimental dataset with labels (closer-to-soma / closer-to-bifurcation) provided by the experimenter. We can also see how the distributions of closer-to-soma and closer-to-bifurcation groups are very much overlapping, especially compared to the simulated cases.

action potential (which is unlikely due to the large EPSP peak sizes).

We used a dataset of spontaneous EPSP pairs, which had large EPSP peaks (>1mV) recorded at the main bifurcation and would intuitively be classified as closer-to-bifurcation. They were extracted from the recordings in the absence of the photo-stimulation. As the onset of those EPSPs is not known in advance, an alternative criterion for detection is required. A threshold of 1mV above the baseline voltage of the main apical bifurcation trace was chosen. This arbitrary criterion will cause a bias towards large EPSPs caused by the spontaneous presynaptic action potentials rather than spontaneous single vesicle release (minis) or smaller EPSPs. It also offers no guarantee that the identified EPSPs will indeed be originating from the closer-to-bifurcation location.

Spontaneous EPSPs are not extracted from the same recording sessions (different cell, different animal) as the ones following stimulation in the labeled dataset.

Figure 4.9 shows the detected EPSPs from three subsequent recording sessions of the same cell. We see that for practically all detected pairs, the EPSP recorded at the main bifurcation has a higher peak than the one recorded at the soma, suggesting it is indeed originating from the closer-to-bifurcation region, either from the apical tuft or the apical trunk close to the main bifurcation. This is further justified by comparing the relationship between the size of the EPSPs at the main bifurcation and the difference in the peak values for EPSPs recorded at two locations (main bifurcation and soma). This relationship is positive and nearly linear. If we compare this with the same analysis performed on the simulated dataset (where we know the locations of the synapses) we see the same positive near-linear relationship corresponds to the synaptic locations located on apical tuft. It should be noted that any spontaneous EPSP originating from the apical trunk or closer-to-soma region will cause an underestimation of the real ratio (as defined in the case of simulated dataset).

We can also notice how the recording quality is decreased in the last recording set (right) resulting in EPSP recordings of smaller sizes and a decreased ratio.

4.3.6 Classification based on the difference of individual parameters

Since attenuation of the EPSPs as they propagate along the dendritic tree implies the reduction of peak size, we expect to be able to discern between the closer-to-soma and closer-to-bifurcation groups by looking at the difference of the peak potentials. For example, if we look at the example of the two pairs of recordings in figure 4.6 we see

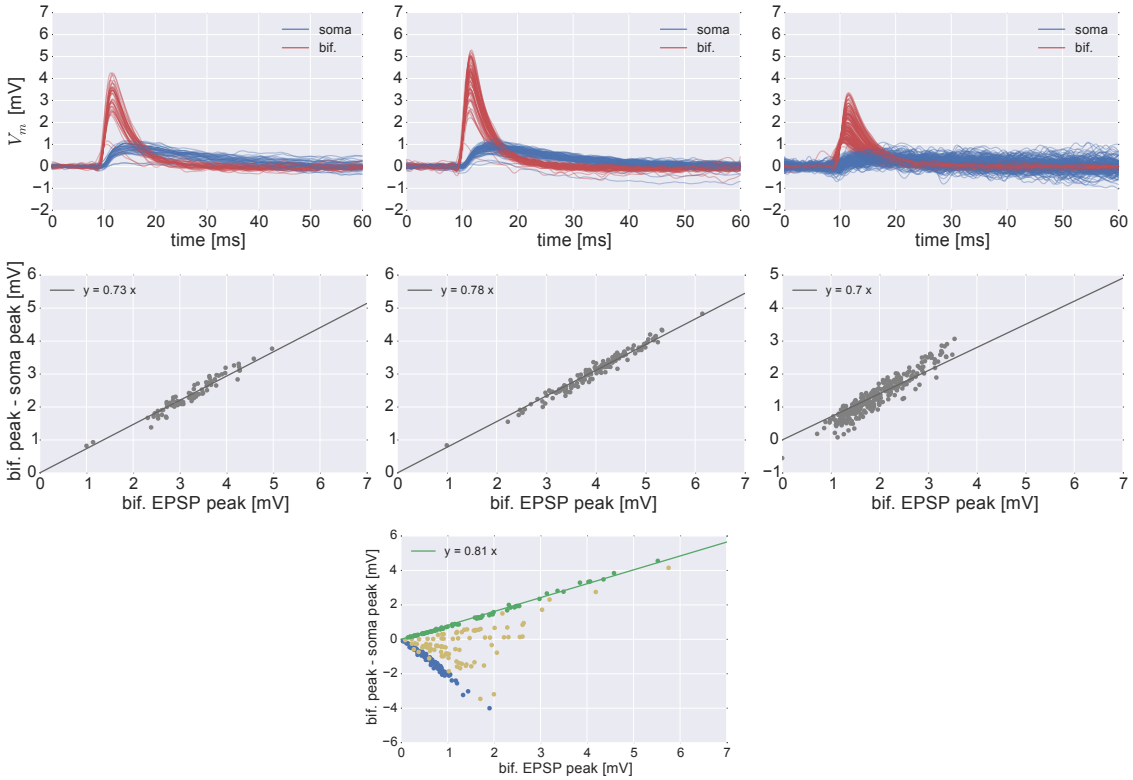

Figure 4.9: **Spontaneous apical EPSPs:** (top) Spontaneous EPSP pairs detected by applying 1mV threshold on the voltage trace recorded at the main apical bifurcation. Each of the three plots represents the EPSPs from the same cell in 3 different recording sessions (all within one hour). Visually all of the pairs seem to correspond to the closer-to-bifurcation region. Recording quality in the last session (the top right plot) is decreased judging by the baseline variability. The EPSP peaks are also decreased.
(middle) Scatter plot of the EPSP peak sizes at the bifurcation vs. the difference of the EPSP peaks. Each point corresponds to a specific spontaneous EPSP. The gray lines show the linear fit of the ratio between the peak sizes.
(bottom) Same as the middle but for the surrogate data presented in figure 4.7. The three colors correspond to different regions on the neuron. Green points represent synapses located on the apical tuft, yellow are synapses on the apical trunk and blue are synapses on the basal dendrites or soma. The linear fit is performed on the data points corresponding to the synapses located located on the apical tuft. Comparing the recoded spontaneous EPSPs (middle) with the simulated ones (bottom) suggests that the synaptic locations in the recorded case are indeed closer-to-bifurcation and could be used for calibrating the model as they form a near-linear relationship.

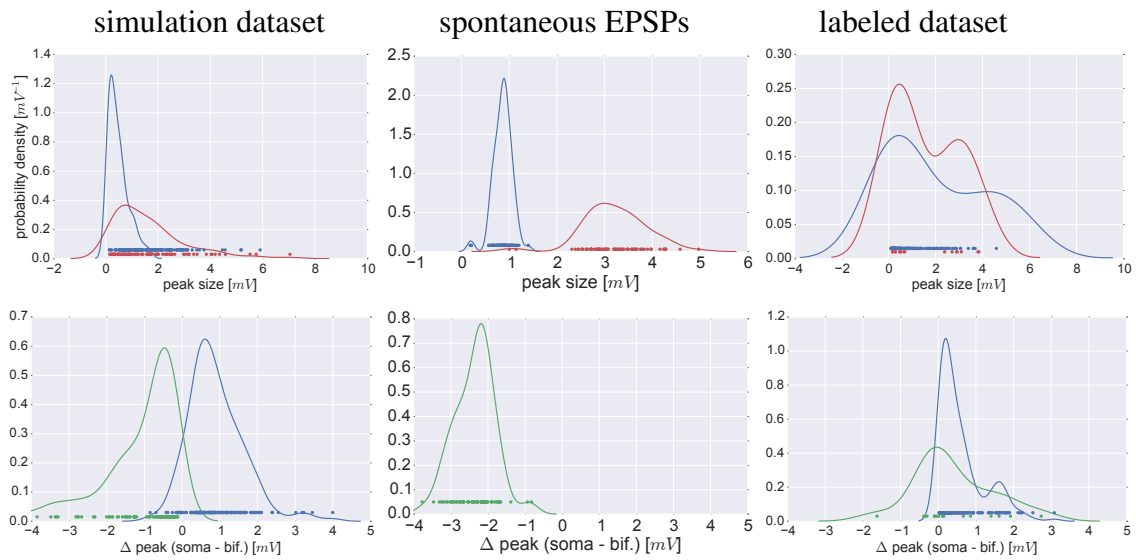

Figure 4.10: **EPSP peak distributions:** (top) Distributions of the EPSP peaks for recordings from the surrogate simulated dataset (top-left), spontaneous EPSPs dataset (top-middle) and the labeled recorded dataset (top-right) The dots represent individual EPSPs (blue measured at the soma, red measured at the main bifurcation) while the lines are the estimated probability densities using a gaussian kernel. (bottom) Distributions of the EPSP peak differences for the closer-to-soma (blue) and closer-to-bifurcation (green) groups.

that for a closer-to-soma location, the peak of the EPSP measured at the soma is about twice as large as the peak of the EPSP measured at the main apical bifurcation.

Unfortunately looking at the distribution of the EPSP peak differences (figure 4.10) we can see that, while in the case of the simulated dataset, the peak differences indeed separate the closer-to-bifurcation from the closer-to-soma synapse locations (although not completely), the closer-to-bifurcation and closer-to-soma distributions of the differences are strongly overlapping in the case of the labeled experimental dataset. A simple classification where we classify all recordings with a bigger EPSP peak at the main bifurcation than the soma as closer-to-bifurcation and the opposite as closer-to-soma would have classified 9 out of 16 examples, for which the experimenter concluded they are closer-to-bifurcation, as closer-to-soma.

As we could see in Figure 4.8 the situation is similar for other parameters. To explore which of the features would be most suited to be used for the classification I trained a linear support vector machine classifier (see the methods for the details) based on each individual feature difference.

The aim of the classifier is to find the hyperplane in the space of all the features which best separates the two classes (closer-to-soma and closer-to-bifurcation). In the case of a single feature this is a single value (threshold) for the feature. For example, for the difference in peaks we would intuitively imagine zero to be the threshold value as it separates cases where soma-measured EPSP peak is bigger than bifurcation measured peak (presumably closer-to-soma class) from the opposite case (presumably closer-to-bifurcation). If we vary the threshold for the classification, we can draw an ROC (receiver/relative operating characteristic) curve which is created by plotting the true positive rate (proportion of all correctly classified cases for a target class, also known as sensitivity or recall) against the false positive rate (proportion of incorrectly classified cases also known as 1 - specificity) corresponding to a specific threshold. Area under the ROC curve is an indicator of the predictor's quality. A predictor at chance level would have the area of 0.5 while the perfect predictor will have the area of 1.

Once the "optimal" threshold (generally a hyperplane) is selected by the classifier, we can construct a confusion matrix which shows the proportions of correctly and incorrectly classified cases for both classes. Note that the optimal value will depend on specific parameters of the classifier which are described in the methods section.

Figure 4.11 shows the performance of the classifier trained using a 2-fold cross-validations on the experimental data set averaged over N=100 trials. In each trial we randomly split the data set in two parts of equal size (with the same proportion of samples from both classes) and use one for training and the other for testing purposes. The top plot shows the ROC curves for the feature differences and in the bottom the confusion matrices for all the 6 feature differences are shown.

We see that some of the feature differences seem better suited to predict the class of the EPSP pair (e.g. Δ rise slope or Δ peak time) than the others (e.g. Δ area or Δ peak size). Even for the best performing feature differences the error rates are above 10% for both closer-to-soma and for closer-to-bifurcation locations (e.g. for Δ peak time about 20% of the closer-to-bifurcation pairs are predicted as closer-to-soma and about 30% of the closer-to-soma are predicted as closer-to-bifurcation).

4.3.7 Adding a cross-correlation feature

One way to improve on the classification can be to look for new features, which would be more informative than the EPSP feature differences. Looking at the performance of the EPSP feature differences we could see that the time-based features (peak time,

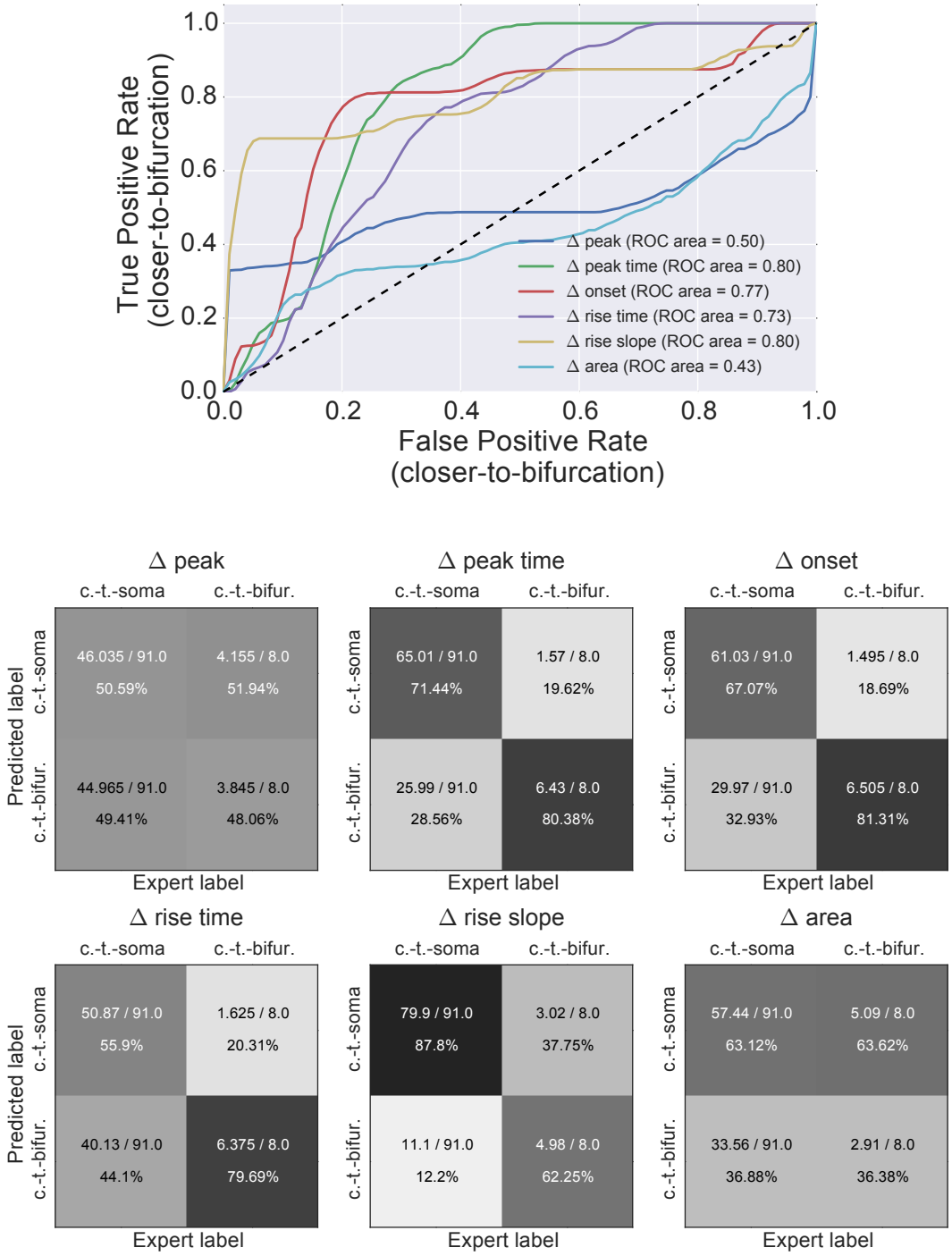

Figure 4.11: **Classification based on individual feature differences:** Top figure shows the ROC analysis of the classifiers based on the individual feature differences. For each feature the results from 100 classifiers trained on a random half of the dataset and tested on the other half (2-fold cross-validation) are averaged. The bottom plots are the averaged confusion matrices for those classifiers.

onset time, rise slope) outperformed the size-based features (peak size, area).

Since most of the EPSP features we looked at so far depend on the single recording point (e.g. peak time) and the recordings can be very noisy, we can try to look at a measure which spans several recording points where we would hope the recording noise would be averaged out.

To combine the idea of using the time-based information and the aggregate recording information we introduce the cross-correlation (cc), more specifically the time lag τ_m at which the cross-correlation between the EPSP measured at the soma and the EPSP measured at the bifurcation is the greatest. This time lag can be loosely thought of as a delay in the EPSP time course due to the propagation along the dendritic tree – if the synapse is further away from soma than the main bifurcation, the EPSP measured at the soma will be "late" as compared to the EPSP measured at the main bifurcation (the time lag will be bigger, so τ_m will be positive).

This is no longer a feature of a single EPSP but rather the feature that combines both EPSPs. The exact definition of the cross-correlation and the extraction process is given in the methods section (4.2.4).

Figure 4.12 shows how the τ_m separates the closer-to-soma and closer-to-bifurcation pairs in the simulations. Each point corresponds to an EPSP pair. The group of blue points with the biggest τ_m belong to the synaptic locations at the basal dendrites and the group of green points on the left to the synapses located at the apical tuft. The ones in the middle are located at the trunk.

The same plot for the experimental dataset is shown in figure 4.13. We can again see that there is no clear separation between two classes, although the difference seems to be more pronounced than in the case of peak sizes. Brightness of the points corresponds to the maximum magnitude of the cross correlation which is an indication of the cross-correlation measure quality for the individual EPSP pair. The magnitude will be small when the shapes of the EPSPs are significantly different in which case the cross-correlation measure is less reliable. We can indeed see that for the more extreme cases the magnitudes are smaller.

4.3.8 Using the combinations of features

Another way to improve the classification would be to look to the combinations of the differences, trying to combine the informativeness of the feature differences.

In figure 4.14 I show the ROC curves and the confusion matrices for classifiers

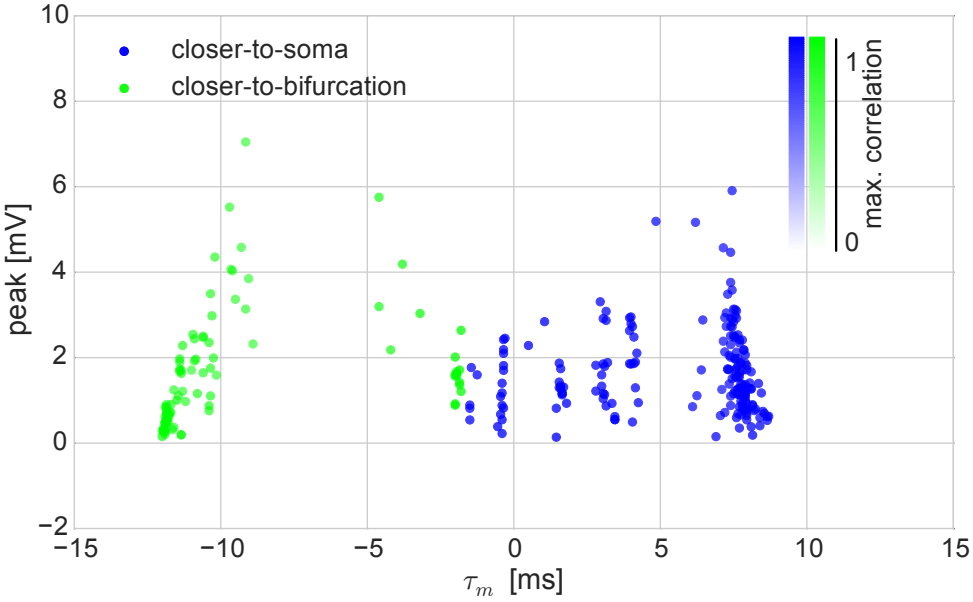

Figure 4.12: **Cross-correlation analysis on the surrogate dataset (from simulations):** Time lags for different synaptic locations on x axis vs. the size of the peak for the EPSP (at the main bifurcation for the closer-to-bifurcation and at the soma for the closer-to-soma EPSPs) on y axis. Each dot represents a pair of the recorded EPSPs from the simulated dataset. The blue dots correspond to the closer-to-soma input locations and the green ones to the closer-to-bifurcation locations. The magnitude of the correlation at $\tau = \tau_m$ (max. correlation) is always close to one (denoted by the opacity of the dots). Time lag at which the correlation is maximum (τ_m) divides the two groups. Notice that the divide is not exactly at the $\tau_m = 0$.

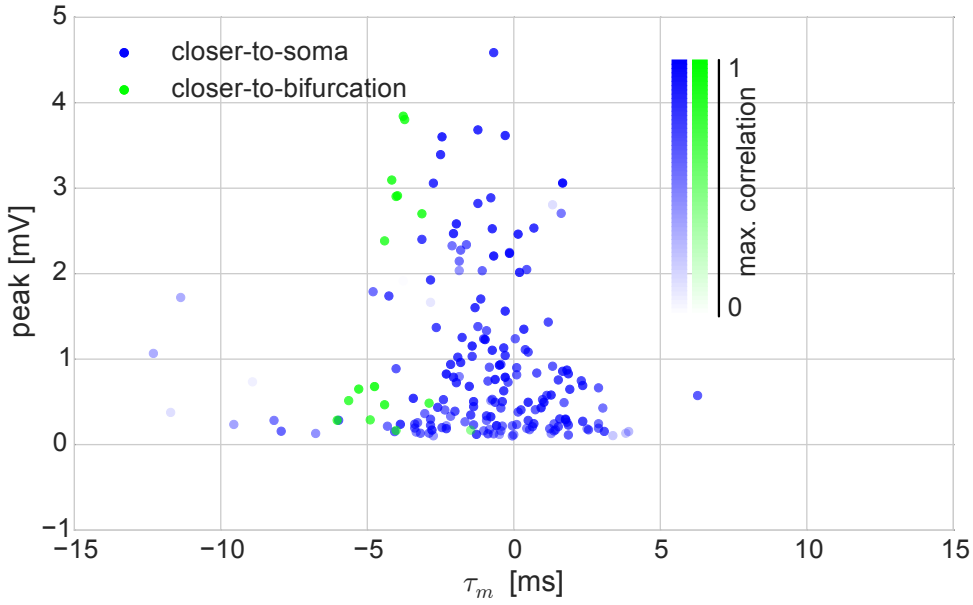

Figure 4.13: **Cross-correlation analysis on the experimental labeled dataset:** Same as 4.12 but for the experimental dataset. The distinction between the two groups is much less pronounced with a large amount of overlap. We can also see that for the cases where a labeled closer-to-soma locations have extremely negative time lags τ_m, the magnitudes of those cross-correlations are small, indicating a noisy measurement.

using the combination of all the previously tested EPSP feature differences, the new cross-correlation measure, and the combination of the two (either using all differences or just the most informative difference - difference in peak times).

Looking at the area under ROC and comparing it to the results for individual feature differences (figure 4.11) we can see a couple of things.

First, the cross-correlation measure indeed seems to outperform all of the individual feature differences. Second, the combination of individual feature differences is only slightly outperforming the best individual feature difference (difference in peak time). Lastly, we see that adding the cross-correlation measure to the combination of all feature differences indeed improves the classification with the respect to the case of using only the differences, but it performs worse than a classifier only using the cross-correlation measure.

While this result might seem counter-intuitive as we might expect that using more features will yield more information and thus better prediction, it follows from overfitting of the classifier in the case of many features (with a limited amount of training data). In those cases the classifier performs very well on the training case, but it uses information specific to the training case which does not generalize to the testing case and thus performs worse when tested with the cases it has not been trained on.

Looking at the confusion matrices we can see that even with the improved classification using the cross-correlation measure we still have significant discrepancy with respect to the manual label. Specifically about 20% of the closer-to-soma pairs are classified as closer-to-bifurcation, meaning that only about 1/4 of all the cases classified as closer-to-bifurcation were indeed labeled closer-to-bifurcation by the experimenter (due to the unbalanced distribution). Only adding one of the individual difference features to the cross-correlation measure does not seem to make a big difference in one way or the other.

4.3.9 Training using the simulated data set

We want to use the classifier for the recordings from an arbitrary cell and also arbitrary animal. We know there is a big variety of cell shapes, even within a certain cell type such as layer 5 pyramidal cell which we are using here. Can the classifier trained on the results of the specific cell (the one we have the labeled dataset for) generalize to other cells (and species)?

To investigate this I took a different approach. I used the simulated EPSP pairs to

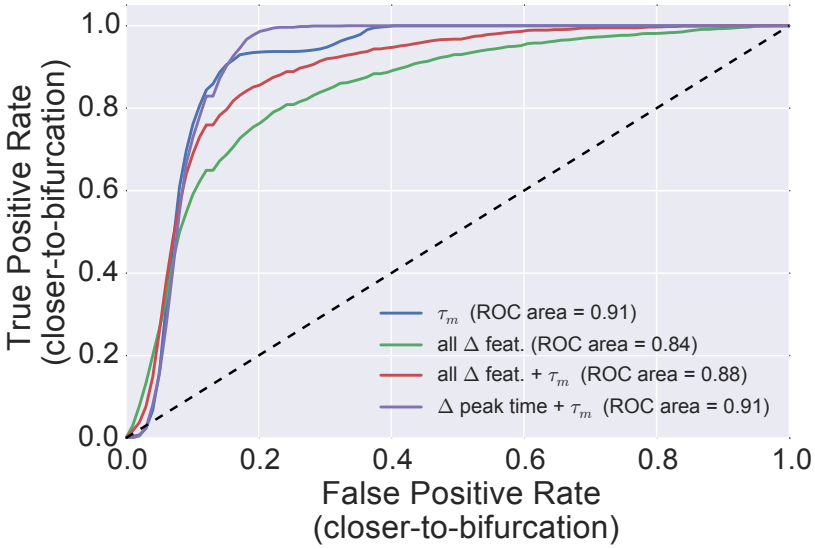

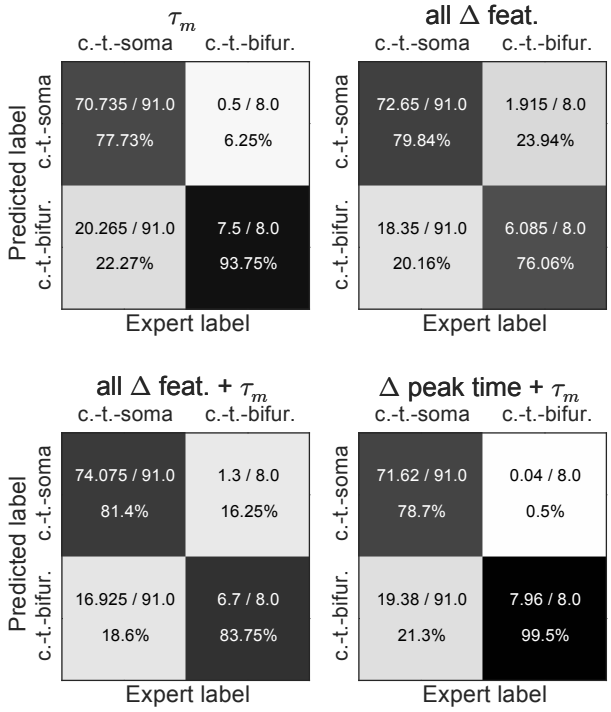

Figure 4.14: **Classification based on the combinations of individual feature differences and the cross-correlation time lag:** Same as figure (4.11), but this time the classifiers are either trained on all the feature differences, on the cross-correlation time lag (τ_m), the combination of the two or the difference in peak time and τ_m. We can see the cross-correlation time lag is a superior classification feature.

train the classifier and tested it on the labeled experimental dataset using the same set of features as in figure 4.14. As the testing and training set are clearly split in this case I do not need to do cross-validation and a repetition of several splits, but only run one training and one prediction using the full simulation dataset for the training and the full experimental labeled dataset for validation.

We see that for classifiers using all feature differences the performance is far worse than it was before. The reason for this can be that as we could see from the feature distribution figure 4.7 in the case of the simulated dataset, the feature differences are always clearly separating the two classes. The classifier trained on that dataset is thus relying on the feature differences which are not really informative in the experimental dataset.

On the other hand for the classifiers using the cross-correlation and cross-correlation in the combination with just the peak time difference, the performance of the classifier is at about the same level as the performance of the classifier trained on the labeled experimental dataset.

4.3.10 Cases with the mismatch in classification

There is a significant proportion of the pairs labeled closer-to-soma by the experimenter which are being classified as closer-to-bifurcation by the trained classifier. I show six of those pairs in figure 4.16. For some of the cases we see that the EPSPs have small peaks so the signal to noise ratio is poor. For some of the others the shapes are either not really compatible (e.g. top left) or the shapes of both measured EPSPs have an unusual shape. This can happen due to several reasons:

- When the excitatory presynaptic neuron is photo-stimulated, another inhibitory (top left) or excitatory presynaptic neuron is stimulated.
- The stimulated presynaptic neuron is connected to our target neuron via several synapses, possibly located in both regions of the post-synaptic dendritic tree.
- The averaging of the EPSPs over several trials might cause deformations as the delays in photo-stimulation induced excitation as well as synaptic transmission delays can be different from one case to another.

Those cases will be very hard to classify automatically.

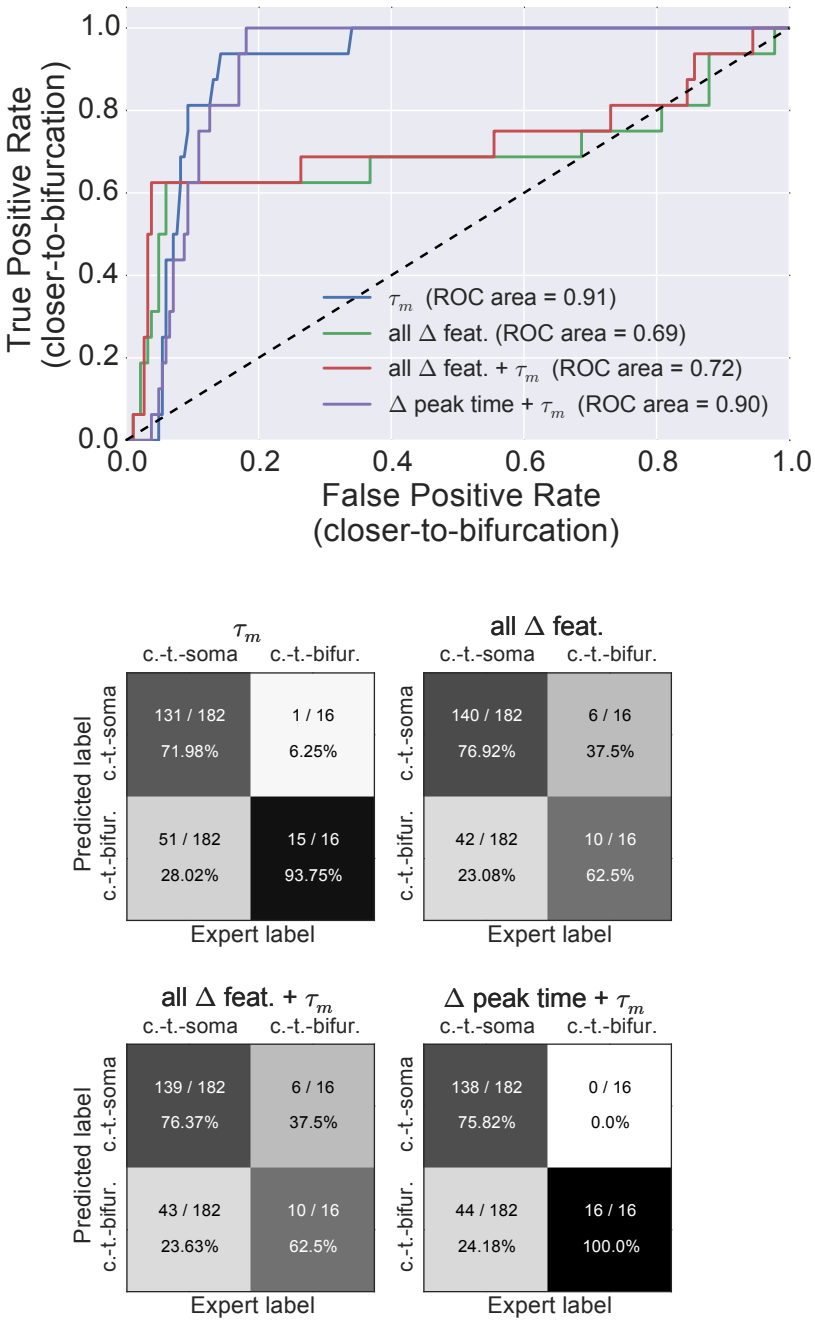

Figure 4.15: **Performance of the classifier trained on simulated data:** Same analysis as in figures 4.11 and 4.14 but this time only for a single case (not averaged) using the simulated dataset for training and tested on the full experimental dataset.

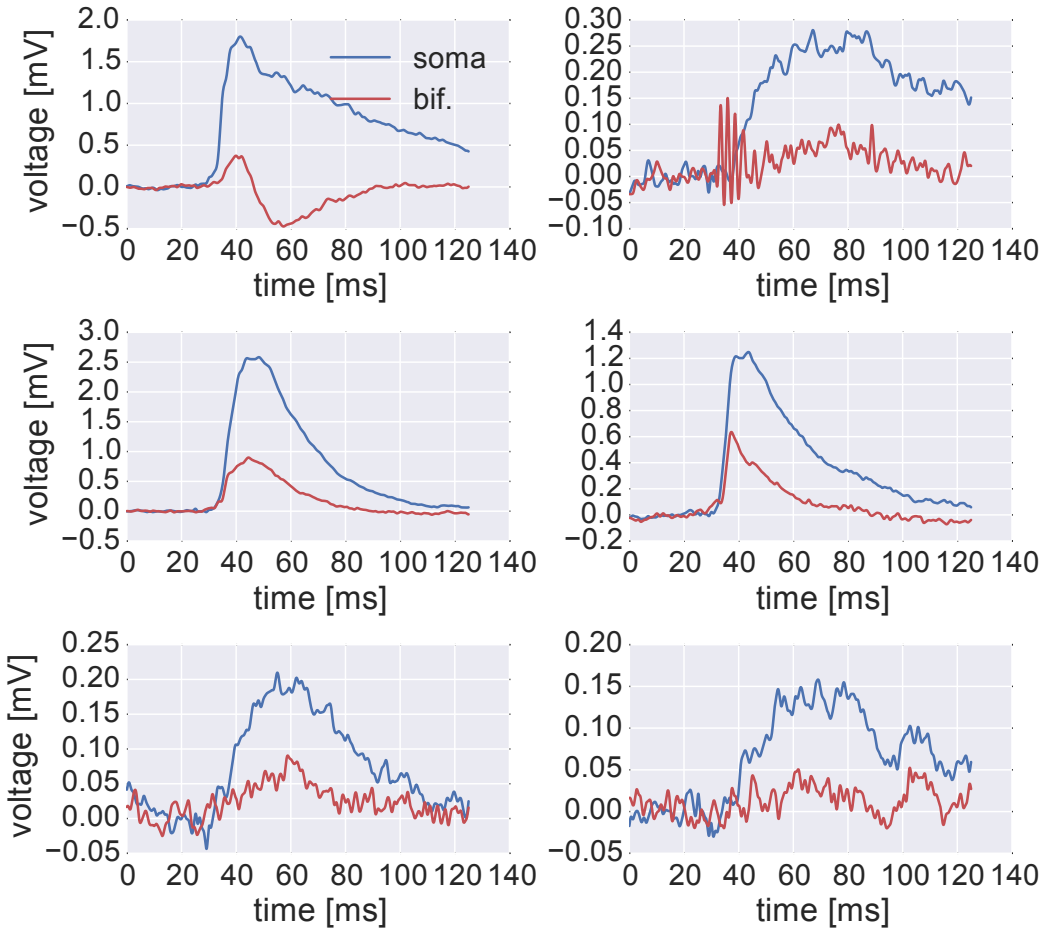

Figure 4.16: **The EPSP pairs where the classifications disagree:** A collection of EPSP pairs classified as closer-to-soma by the experimenter and as closer-to-bifurcation by the classifier using the cross-correlation time lag and the difference in peak time as the classification features. Some of those EPSPs are either very small in size (top right and bottom two) or have incompatible shapes (top left), which is the probable reason for mismatch in classification in those cases.

4.3.11 Customizing the classifier to individual recordings

In the previous section I showed that the classifier using a good set of features (cross-correlation and difference in peak times) performs similarly whether it was trained on the labeled dataset of the same cell it is doing predictions on, or on a simulated dataset. As the simulated dataset was not specifically customized to the recorded cell (i.e. I took an arbitrary model of L5 pyramidal cell without fitting for the attenuation levels between soma and the main bifurcation) this means that we either found a good matching simulation dataset by chance or that our simulation model is generic enough for building the classifier.

It would be possible to adapt the simulation models so that they would better fit with the properties of the arbitrary recorded cell. A relevant measure we can try to optimize for is the attenuation level between the main bifurcation and soma. If we take the spontaneous closer-to-bifurcation EPSPs (see section 4.3.5) which can be extracted from the time during the recording session where there is no stimulation present, we can estimate the attenuation level by looking at the relative difference of EPSP peak sizes at the main bifurcation and the soma (see figure 4.9).

This attenuation can be manipulated in the model in several ways, either by changing the morphology of the model (distance between the soma and the main bifurcation or the diameter of the apical trunk connecting them) or by changing the biophysical properties of the model (relative axial resistance, relative membrane conductance or capacitance). In the figure 4.17 I show the estimations of the relative peak size difference where I modify the relative axial resistance either by doubling it or making it half of the default value. With this we can modify the relative attenuation from 0.8 to an interval between 0.7 (halved membrane resistance) and 0.9 (double membrane resistance).

I tested how the performance of the classifier trained with the examples from modified model would be affected by the modification. I chose the model with the halved resistance as it yields the relative peak difference which better compares to the value obtained from the spontaneous EPSPs (although note that the spontaneous EPSPs are not obtained from the same cell as the labeled experimental dataset so an actual calibration is not possible). The results are presented in figure 4.18.

There is a modest improvement in the classification in the cases where we have all the feature differences compared to the default model case. Also looking at the confusion matrices we see that we are now misestimating less of the closer-to-soma pairs

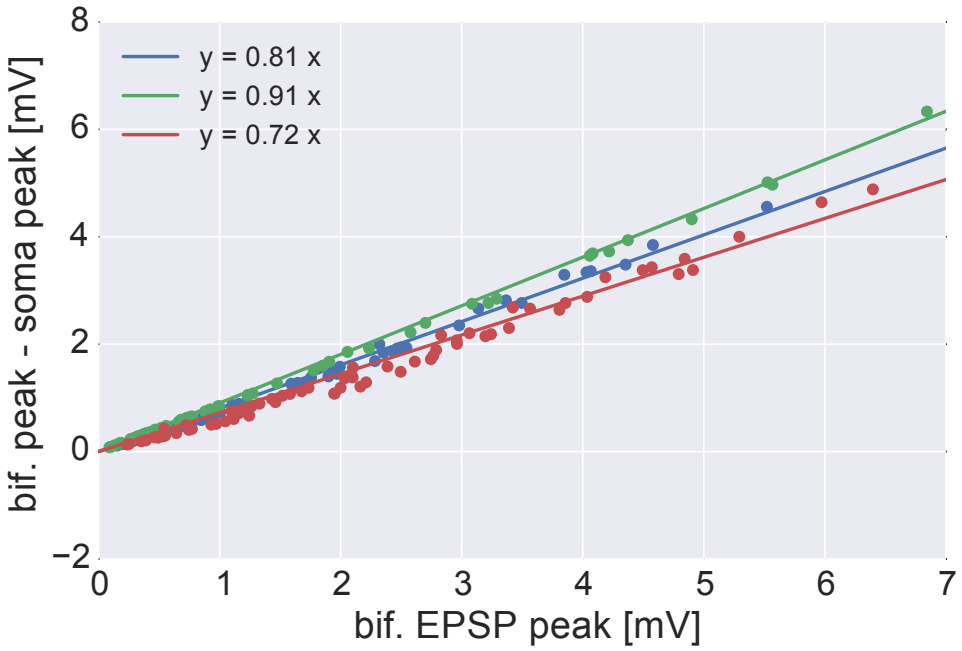

Figure 4.17: **Calibrating the model:** Estimations of the relative peak size difference for different values of the relative axial resistance in the simulation model. All the inputs are located at the apical tuft. Adjusting the axial resistance of the simulation model to fit the relative peak size difference observed in the spontaneous EPSPs analysis (see figure 4.9) is a possible way to calibrate the simulation model to the measured cell. Note that the spontaneous EPSPs in figure 4.9 are not recorded from the same cell as the stimulation-based EPSPs in our experimental dataset so a calibration is not possible using the existing data.

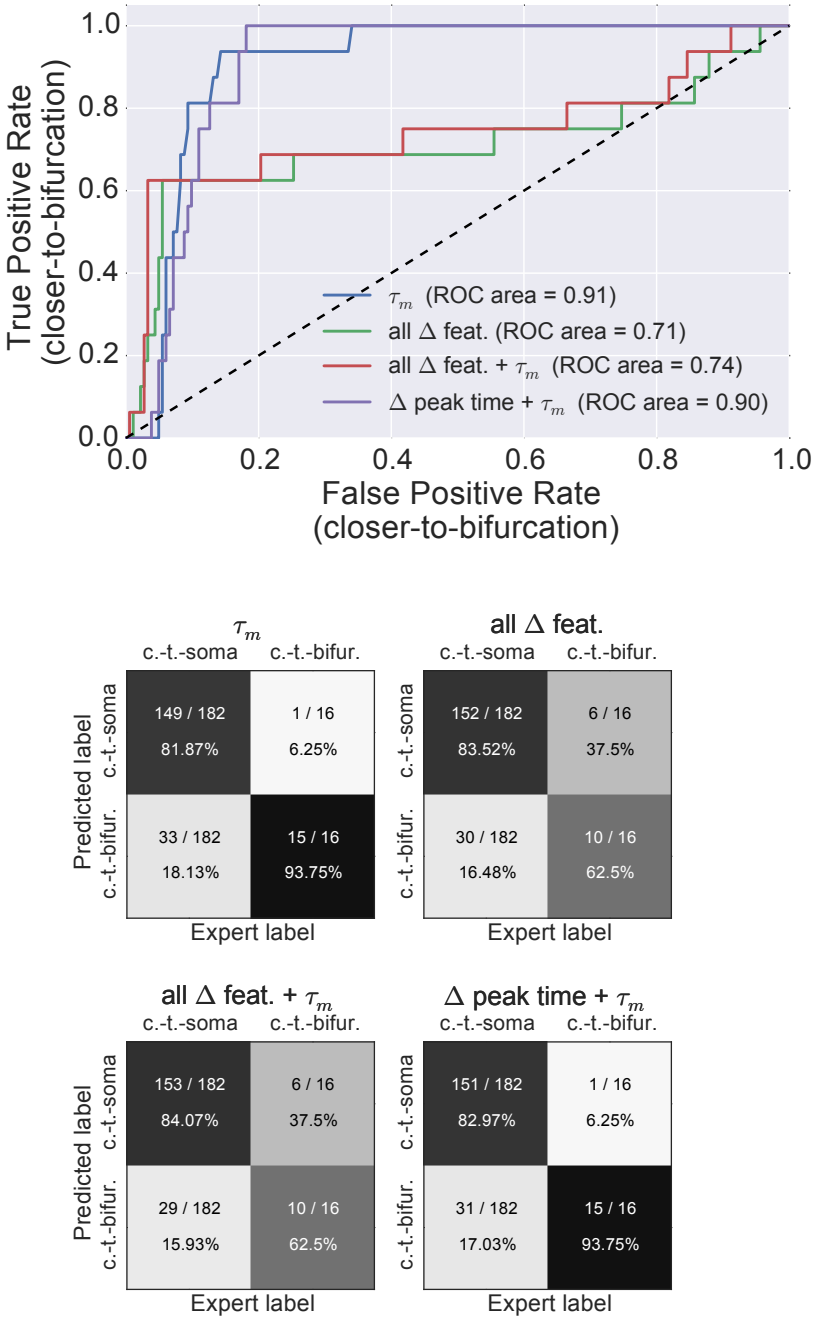

Figure 4.18: **Performance of the classifier trained on simulated data with the modified model:** Same as figure 4.15, but using the data from the modified simulation model as a training data to the classifier. This modification improves the agreement between the automatic classification and the classification done by experimenter to some extent, suggesting it might be beneficial to customize the classifier to each recorded cell.

in the case where we use the cross-correlation and peak time difference (31 instead of 44).

4.4 Discussion

In this study we presented an approach for determining the region of the excitatory synapses on the dendritic tree of a layer 5 pyramidal cell following the photo-stimulation of the presynaptic cell, given the measurements of the excitatory post-synaptic potentials at two locations on the dendritic tree. Using this method on the recordings from a collection of cells would yield a probabilistic map of the connectivity between the excitatory cells in different layers for the somatosensory cortex and the regions on the layer 5 pyramidal cell [86]. This is important as the layer 5 pyramidal cell has been shown to have complex mechanisms of input integration which depends on the location of the inputs on the dendritic tree[17, 18, 19]. Specifically the apical region of the dendrite is thought to be partially dissociated from the basal part including the soma, which could potentially lead to a 2-step integration of the inputs [72, 17].

I investigated the possibility of constructing an objective classifier using the dataset of 198 EPSP pairs where the experimenter has labeled the pairs as being associated to the synapse which is either located in the region closer to the soma (closer-to-soma) or in the region closer to the main apical bifurcation (closer-to-bifurcation). The expert labeling was done based on the onset times of the EPSPs. The experimental technique did not allow for a more direct verification of the synapse location so those labels are taken as the ground truth in the training or evaluation of the automatic classifier. Another difficulty lies in the fact that only 8% of the recorded pairs were labeled as closer-to-bifurcation. It is unclear why this imbalance occurs (whether this is a genuine property of the connectivity to our target cell, a bias of the recording method, or the bias of the labeling).

I find that a classifier based on the difference of the various features (peak size, peak time, onset time, rise time, rise slope, ...) between the two recorded EPSPs – one recorded at the main apical bifurcation and the other recorded at the soma – is not able to split the labelled classes well which is at least in part due to the difficulties in extracting features from noisy measurements, specially in the EPSPs with the small peak sizes. When a more robust measure (the cross-correlation time lag) for the EPSP pair difference is used, the classifier performance is improved.

As the aim was to construct an objective classifier which could be used for the

future recordings, it is not feasible to use the dataset of recordings labeled by the experimenter as the ground truth when training the classifier. I thus used the simulated recordings using the full morphological passive model of the layer 5 pyramidal cell to create a surrogate dataset of recordings and used this dataset for the training of the classifier. The classifier trained in this way performs similarly to the one trained on the portion of the labeled experimental dataset.

Even after the attempted calibration of the neuron model the mismatch between the automatic classification results and the expert classification is worrying (figure 4.18), especially as about two thirds of the pairs classified as closer-to-bifurcation by both classifiers had been classified as closer-to-soma by the experimenter. In order to determine where this mismatch comes from we would require a set of experiments which would provide the ground truth. An example of this could be directly exciting the synapses of the target neuron by either puffing the glutamate or sucrose at the synapses or by using the two-photon excitation methods, which would give a set of recorded pairs with a known location. Another possibility would be to try to patch some of the cells which were excited by the photo-stimulation and fill them with the dye to determine their axonal projections after the morphological reconstructions which in combination with the reconstruction of the recorded cell could yield the synapse locations. It is worth noting all of those would be adding significant experimental complexity to the already challenging method of patching a cell at the two locations.

Especially for the very small EPSPs the signal to noise level becomes very small. One way to improve on this would be to hyperpolarize the recording neuron by injecting it with a current, which would yield higher difference between the reversal potential and the actual cell potential, increasing the size of the EPSPs. This would however introduce a bias, as the increase would be bigger for the EPSPs closer to the soma due to the space-clamp issues [87] (see chapter 3). Another issue with hyper-polarization are the voltage-gated Ih channels which work to counter-balance the injected current. Their opening thus counters the benefits of hyper-polarization and additionally introduces an increase in the input conductance.

To deal with the signal-to-noise level we averaged the recordings from multiple trials. This can introduce deformations in the EPSP shapes, especially due to the delays in photo-stimulation and synaptic transmission delays. A possible extension would be to combine the classifications based on the averaged EPSP pairs with the classification done on the individual EPSP pairs.

We also saw a case of a recording where we clearly excite both the excitatory as

well as inhibitory presynaptic cells which can change the cross-correlation lag feature (τ_m). Typically a photo-excitation of the inhibitory cell which is connected to our target neuron is avoided by choosing the excitation locations further away from the target neuron. To further suppress the cases where there is still the inhibition present, one could consider using the blockers of inhibitory receptors.

There might be cases where the problem is ill-defined. This occurs in the case of multiple contacts between the presynaptic and the postsynaptic cell, when some of the synapses are closer to the soma and some closer to the main bifurcation. The classifier in the current state would not be able to identify those cases. If we used a classifier which instead of a predicted class returns the probability of a class (e.g. logistic regression [88]) we would expect those cases to be close to the classification border between the two classes.

Besides the linear SVM classifier I also tried using the nonlinear SVM classifier with a radial basis function kernel [89] to improve the classification in case the classes were not linearly separable but found the results were comparable or worse than for the linear SVM. Other classification methods such as random forests could be explored.

The use of the model for the training of the classifier allows us to build a classifier specific to each recorded cell by calibrating the model using the spontaneous EPSPs. The calibration is done by changing the relative axial resistance in the model in a way that the relative attenuation of the spontaneous EPSPs from the closer-to-bifurcation region matches the relative attenuation in the model. While the existing data did not allow me to do the calibration (the data from the recorded spontaneous EPSPs and the data from the recorded stimulation induced EPSPs were taken from two different recording sessions), I demonstrated how such calibration could work. However, the results of the classification did not seem to differ much for classifiers trained on two different models. Here we specifically filtered out the spontaneous events with large EPSPs measured at the main bifurcation. For a more precise calibration of the model we could consider using spontaneous events with EPSPs larger at the soma to calibrate the attenuation in both directions independently.

Possible further explorations into the robustness of the method would include exploring the effect of changing the synaptic time constants in the model or the effect of noise on the training of the classifier and its performance.

Chapter 5

Overview and future work

The overarching goal of the thesis was to use computational modeling and simulations to gain insight into the structure and dynamics of the synaptic communication based on data obtained through whole-cell recordings. Specifically, a method for inferring the excitatory and inhibitory input to the cell from the membrane voltage recordings at the soma *in-vivo* was developed and applied to recordings from the layer 5 pyramidal cells from the motor cortex of mice (chapter 2). Using analytical calculations and numerical simulations the influence of neuron morphology on the input estimation was explored (chapter 3). Finally a combination of signal processing methods and simulations was used to determine the region of synaptic input, based on simultaneous membrane voltage recordings at two locations on layer 5 pyramidal neurons in somatosensory cortex (chapter 4).

In this chapter I summarize the results, outline some future extensions for each of the presented chapters and discuss their contributions to the field of neuroscience.

5.1 Estimation of the synaptic input from the intracellular recordings

In chapter 2 we extracted statistics of the synaptic inputs to neurons based on the intracellular recordings of membrane voltage and input conductance. To do this we extended the existing methods for the estimation of the mean global synaptic inputs [29, 24, 23, 30] but also used the second-order statistics (power spectral density) of the membrane potential. We developed a method which combines analytical calculations for a point neuron model with numerical simulations of the modeled system. Taking a

set of assumptions along with parameter values obtained from previous studies found in the literature, the method estimates the mean sizes and frequencies of the excitatory and inhibitory events reaching the soma.

The method was applied to whole-cell membrane voltage recordings from the soma of pyramidal layer 5B cells in the motor cortex of awake behaving mice which are either voluntarily moving or in a quiescent state. The neurons were split based on the statistics of cell activities within those two behavioral states - enhanced or suppressed firing rate during movement. The membrane voltage and firing statistics of both groups of neurons during the quiescent state were not distinguishable ($L5B_{quiet}$) while the statistics of the neural activities during movement for both subgroups of neurons were different ($L5B_{enh}$, $L5B_{supp}$). The main change in the inferred time-averaged input conductance between the two behavioral states in the neurons was the increase of the excitatory conductance between $L5B_{quiet}$ and $L5B_{enh}$ ($\Delta g_e = 0.7$ nS) and a mild decrease of inhibitory conductance between $L5B_{quiet}$ and $L5B_{supp}$ ($\Delta g_i = 0.1$ nS).

Additionally we found an increase in the power spectral density for the frequencies between 1.5-4 Hz in the quiet case $L5B_{quiet}$, which corresponds to the previously reported oscillations in other cortical areas both from intracellular as well as extracellular recordings [53, 54, 55]. We incorporated those oscillations in our simulations with the temporal firing rate modulations in the excitatory inputs.

Most interestingly the amount of the increase in the power spectral density in the frequency range 15-30 Hz between the $L5B_{quiet}$ and $L5B_{enh}$ could not be explained by the increase in the excitatory conductance (and thus the estimated increased excitatory input frequency). There are several possible explanations for this. One possibility is that the overall sizes of the inputs increase from one state to another by some neuromodulatory mechanisms. Another possibility is that the average sizes of input population increase due to the selective increase of the input rates for the bigger sized inputs. Finally there might be a change in the temporal structure of the inputs. While we know of no way to distinguish between those options in the current experimental setup, we show how additional instantaneous correlations in the excitatory inputs could explain the observed effect.

As this question is closely related to the nature of neural coding in the motor cortex, it would be interesting to study it further. To study the increased correlation hypothesis one could experimentally try to determine the state-dependent changes in neuron spike correlations in a population of Layer 5B neurons using extracellular multi-electrode [90, 91] or calcium imaging techniques [92, 93, 94]. To explore the neuromodulatory

hypothesis one could try to repeat the measurements while blocking the effects of neuromodulators in the tissue (although this might perturb the system in other ways).

Most methods for inferring the input conductances focus on estimating the mean conductances [29, 24, 23]. Rudolph *et al.* [30] extended the standard method to also estimate the variances of conductances. We went a step further and derived a method for estimating the mean input sizes and total input frequencies. For this a number of assumptions had to be made. Most notably the input spike trains were presumed to be independent spike trains. While this assumption is most likely too simplistic, the method could naturally be extended to allow for the relaxation of those assumptions once the nature of the correlations in the cortex are better characterized experimentally. Even with these and other assumptions described in section 2.4 the method gives reasonable estimation of the input frequencies and provides an interesting hypothesis about the role of correlations in the motor cortex of mice.

Finally all the inferences we have made in this study relate to the input effects at the soma. While these are the ones relevant to the neuron output and thus interesting on their own, one would ideally also want to know more about the actual synaptic inputs to the neuron. For this we need to understand the effects of neuronal morphology on the membrane potential and input resistance measured at the soma which was the focus of the next study.

5.2 The effect of the morphology on the synaptic input

The synaptic signals are filtered by the dendrites as they are propagated towards the soma. This attenuation is important from the functional perspective of the neuron, as the integrated signal at the soma determines its output. At the same time it is important to understand the filtering properties if we want to infer information about the synaptic inputs in the dendrites from the intracellular recordings at the soma.

In chapter 3 I have explored these morphology effects in the passive models of neurons. First I studied the simplified model of a neuron - a homogenous cable. I considered two extreme cases of synaptic input distribution – input focussed in one location and uniformly distributed along the whole cable. I derived the closed-form solution for the steady-state case. The solution presents the attenuation profiles for the membrane voltage and input conductance based on the synapse location (for the case of localized input) or input size (for the case of distributed synapses). Importantly in both cases the input conductance attenuation is bigger than the membrane voltage

attenuation.

If we were to use the measurements of membrane voltage and input conductance at the soma to directly estimate synaptic inputs using the point-model assumption, we would be underestimating the synaptic conductances as is well known [26, 30]. I showed that due to the different attenuation of membrane voltage and input conductance and due to different driving voltage of excitation and inhibition, also the ratio of excitatory and inhibitory synaptic conductance is misestimated.

Next, I showed how the morphology affects the power spectral density recorded at the soma for a case of a localized input. The morphology acts as a low-pass filter, reducing the power at the higher frequencies more strongly than in the lower ones.

Using numerical simulations I looked at the steady-state effects of the morphology on input misestimation in the morphologies of different neuron types and showed how the conductance misestimation effect is stronger for bigger cells where the inputs can generally be located further from the soma (in terms of the electrotonic distance). For example in the layer 5 cells the conductances are estimated to be between 40% and 70% of the actual conductance value (depending on the actual input size and the distribution of input locations). Assuming a realistic distribution of synapse location with inhibitory synapses located close to the soma and excitatory synapses located uniformly on the dendritic tree [5] and taking the input conductance values estimated in chapter 2 for layer 5B pyramidal cells in the primary cortex of mice, I find both excitatory and inhibitory inputs at the soma are estimated to be at $65 \pm 5\%$ of their actual value. The ratio between excitation and inhibition for these distributions of synapses would be estimated correctly as the proximity of the inhibitory synapses to the soma counterbalances the bias caused by the difference in the driving voltage between excitation and inhibition. The corrected total conductances in the case of quiescence ($L5B_{quiet}$) are then $\langle g_i \rangle = 4.6 \pm 0.4$ nS and $\langle g_e \rangle = 3.4 \pm 0.35$. If the distribution of the inhibitory inputs is uniform across the dendritic tree [95], the underestimation for the inhibitory conductance would be bigger (from 65% to 50% of the actual signal) and the ratio of excitation to inhibition would be overestimated ($\approx$1.3 times the actual value).

The explorations in this chapter offer the insight in the magnitude of the misestimations and will help in the interpretation of experimental studies. A future goal would be obviously to fully integrate chapters 2 and 3, so that the estimating method described in chapter 2 can take the morphology into account. Interestingly the cells measured in the whole-cell recordings are often morphologically reconstructed so a precise geometry is available.

The effects of voltage-gated channels could also be explored. While most of the known voltage gated channels are closed at the sub-threshold voltages and thus don't affect the estimations (as long as the firing rate of the recorded neuron is reasonably small (<10 Hz) [30, 35]), channels such as I_h and channels facilitating the slow K^+ current are opening when the membrane potential is subthreshold, which would interfere with the synaptic input estimations. Furthermore the distribution of the I_h channels across the dendritic tree of layer 5 cells is characteristically non-uniform with higher densities at the distal dendrites [96] so the effects should be studied along with the neural morphology and synapse distribution.

Chapter 3 is not only relevant for the analysis of intracellular recordings. Simplified single-compartment models are often used in theoretical studies [4, 2, 11]. In those cases the synaptic inputs are sometimes modeled as voltage-independent current-based inputs as this allows for easier analytical treatment. Such simplification has been shown to affect the dynamics of neuronal networks [59, 71]. I show that the synapse effects at the soma are in fact a mixture of a current-based and conductance-based input. The findings can serve as the facilitation of the future simplified neuron models where the exact current-to-conductance ratios can be adjusted according to the specific morphology and synapse distribution of a certain neuron type allowing for more precise network models (e.g. cortical network models).

5.3 Input location estimation

In chapter 4 we presented a method for determining the region of excitatory synapse locations on the dendritic tree of layer 5 pyramidal cells. The method aims to classify whether the synapse between the presynaptic cell and the postsynaptic layer 5 pyramidal cell is located closer to the soma or closer to the main bifurcation on the apical trunk by comparing the EPSPs recorded at two different locations on the cell. The presynaptic cells were stimulated by a focussed UV laser beam which releases the caged glutamate from the solution in which the slice is bathed. The position of the laser beam was switched allowing for a fast scanning of the surrounding tissue around the postsynaptic neuron, avoiding the direct stimulation of the recorded cell.

The EPSPs are filtered as they propagate on the dendritic tree, changing their shape and size. In order to determine the region where the synapse is located I took advantage of those changes as well as the temporal lag between the EPSPs measured at the two locations.

The classification method was developed on the dataset where the specific pairs of EPSPs are labelled by the expert based on the EPSP onset times and peaks. As there was no direct access to the locations of the synapses, the expert labels were taken as the ground truth in training the classifiers. The classifiers were trained on the EPSP shape features and their differences extracted from the averaged EPSPs over 3 trials. We found that adding a cross-correlation lag measure between the two EPSPs as the feature to the classifier improves its ability to learn the fitting to the labeling of the expert.

The classifier was then trained on the surrogate simulated data where the synapse location (ground truth) is known in advance. When tested on the labeled experimental dataset it performs similarly as the classifier trained on the subset of the labeled dataset. Ideally, however, one wants to avoid the need for the experimentalist to label each recorded dataset to avoid the human bias and to be able to scale up the analysis. For this I explored the option of training a separate classifier for every recorded cell by first calibrating the neuron model to the recorded cell using the attenuation of spontaneous EPSPs and then using the simulated data from the model to train the classifier. As the data from the spontaneous EPSPs did not come from the same recording as the labeled EPSPs I could not directly assess this method, but have demonstrated the calibration of the cell which shows a modest improvement in the classification match.

To further develop this method one could either consider the improvements on the experimental or analysis side. On the experimental side we could try to improve the quality of the recordings by increasing the driving voltage by hyperpolarising the cell or try to increase the number of recordings at each stimulation location by only repeating the stimulations at the locations where the connected cell has been found. Alternatively one could approach the question of connectivity using different recording techniques such as a combination of dynamic laser stimulation with calcium imaging [92, 93, 94].

For the analysis part the classification could be tested and refined by including realistic noise to the simulated dataset. Further, one could theoretically study the inference of input locations based on the recordings from several sites on the dendrite. Such studies could answer questions such as how many recording sites on the neuron are required for determining the synapse location at a specific spatial resolution and what are the optimal positions of those recording sites on the dendrite to support future experimental studies.

The described method will be unable to classify all of the synaptic inputs even if

the classifier is perfectly calibrated. The photo simulation might excite a presynaptic inhibitory neuron which would corrupt the recording or the presynaptic excitatory neuron might form several synapses in different regions of the dendritic tree.

The locations of the synapses on the dendritic tree importantly shape the integration of the input performed by the neuron and its output [9, 10, 17, 20]. Besides the influence on the conductive input estimation discussed in the previous section, those effects are suggested to be an integral part of the information processing in neurons, implementing a two-stage integration via dendritic spikes [72, 17]. Furthermore the studies in synaptic plasticity show that different plasticity rules apply to different regions of the dendritic tree [97]. When we study the connectivity of the cells in the tissue (e.g. in the cortex) we must thus not only find which neuron types and cortical layers are being connected, but also study where on the dendritic tree of a neuron the connections are formed. This is specifically relevant for the layer 5 pyramidal cells, where the dendritic tree is big and where a large part of the dendrites is located far away from the soma (i.e. apical tuft).

Several methods have been suggested to tackle this. Volume electron microscopy [78, 79, 80] gives a complete image of the tissue but is laborious to process and has thus so far only been applied to smaller volumes of tissue. On the other hand approximate methods which estimate the connectivity location probability based on geometry of cells have been proposed [98, 52]. While such methods can be applied automatically on the larger scale, they are limited by relying on the geometry and would thus be biased by selective synapse formation between neuron cell types. Both the volume electron microscopy and the approximate geometry-based methods are also limited by only describing the structural connectivity while not being able to explore the functional connectivity (the strengths of the connections). The most complete method for a full structural and function connectivity profiling is a combination of patch-clamp recordings from connected pairs of cells with the morphology reconstruction [75]. This method is however very labour intensive as it is first difficult to find the connected cells and then perform the morphological reconstructions for each of the pairs.

The method we described offers the description of both structural and functional connectivity for excitatory connections. While we are only able to estimate the region of the synapse, this is already interesting for the models of two-stage integration [17, 72]. It is particularly useful for examining the long-range projections where the connectivity probability between the cells is smaller [76] and the method of paired patch-clamp recordings thus particularly challenging. The combination of the two

methods could enable us to build more precise models of cortical networks and further advance the understanding of the role of dendritic computation [9, 10] in information processing.

5.4 Final conclusion

The focus of this thesis was the inference of synaptic input integration in the individual neurons. Specifically I have shown how modeling can assist in the analysis and the interpretation of the recordings aimed at determining the synaptic input to the recorded neuron (chapters 2 and 3) and in the estimation of the input locations (chapter 4). As the recordings in single neurons are difficult to perform and require animal sacrifice it is important to extract as much information about the underlying system as possible. Modeling along with the analytical and numerical treatment of the models can be used to provide a better insight into the system. The extracted information can be used to constrain future descriptive models used for exploring the information processing principles of the brain and suggest new experiments to probe the brain function. Repeating this cycle will bring us closer to understanding how the brain functions.

Appendix A

Homeostasis in spiking neural networks[1] [2]

A.1 Introduction

Neurons in the brain are subjected to varying conditions such as developmental processes, synaptic plasticity, changes in the sensory signals, and tissue damage. Those processes can all lead to over- or under-stimulation of neurons. Because it is potentially damaging to cells and energy inefficient, it is undesirable for the activity of individual neurons to be too high for prolonged periods, while prolonged low activity is information poor. Neural homeostasis is believed to prevent such situations by adjusting the neural parameters and keeping neurons in an optimal operating regime. Such a regime can be defined from information processing requirements [99, 100], and possibly supplemented with energy constraints [101]. Homeostasis can greatly enhance computational power in models [102, 103, 104] and a number of diseases have been linked to deficits in homeostasis [105, 106, 107]. Therefore, it is important to know the fundamental properties of homeostatic regulation, its failure modes, and its constraints.

The following work focusses on one of the two homeostatic mechanisms - intrinsic excitability homeostasis (the other one being the synaptic homeostasis) [108, 109]. The other mechanism – synaptic homeostasis – scales excitatory synapses down and

[1] This chapter is a part of the project done in collaboration with Daniel Harnack, Antoine Chaillet, Yacine Chitour and Mark C.W. van Rossum (the full paper is in review). It focuses on my contribution, which is the analysis of the non-linear system, specifically the analysis of the spiking recurrent neural network. It was partially presented at the Cosyne 2014 conference.

[2] Most recently the stability conditions were refined for the non-linear network. While my contribution, the spiking network, is unaltered, and the stability conditions turn out to be very similar, the interested reader is referred to the upcoming paper.

inhibitory synapses up in case of over-excitement, while intrinsic homeostasis reduces the firing rates by increasing the firing threshold of neurons. Intrinsic homeostasis correlates biophysically to changes in the density of voltage gated ion channels, [110, 111, 112], as well as the ion channel location in the axon hillock [113, 114].

All homeostatic mechanisms include a sensor of the activity and a negative feedback that counters deviations of the activity from a desired value. Control theory describes the properties of feedback controllers and the role of their parameters [115]. In engineering one typically strives to bring a system rapidly to its desired state with minimal residual error. While it is reasonable to assume that neural homeostasis has to be fairly rapid too in order to be effective, the homeostatic process should not interfere with the typical timescales of perceptual input or of neural processing (millisecond to seconds). In practice intrinsic excitability homeostasis is typically very slow, on order of many hours or days ([110, 116, 112, 117], but see [111]). One hypothesis is that this is sufficiently fast to keep up with typical natural perturbations. An alternative hypothesis, explored here, is that stable control necessitates such slow homeostasis.

Here the stability conditions for networks of neurons equipped with homeostasis is examined. We show that homeostasis can destabilize otherwise stable networks and that, depending on the amount of recurrence, stable homeostatic feedback needs to be much slower for networks than required for single neurons. Two theoretical limits of the homeostatic speed for the case of linear and the non-linear input-output relations in rate-based networks are described. Finally the activity of the excitatory spiking network with the homeostatic control is analyzed and the results are compared with the theoretical predictions.

The results put constraints on the design and interpretation of homeostatic control and help to understand biological homeostasis.

A.2 Mathematical model

A.2.1 Single neuron

First a model of a single neuron with homeostasis is analyzed. The activity of the neuron is as a function of time with a firing rate $r_1(t)$, thus ignoring exact spike times. The system of differential equations describing the homeostatic mechanism is the following:

$$\tau_1 \frac{dr_1(t)}{dt} = -r_1(t) + g(u(t) - \theta(t)) \quad \text{(A.1)}$$

$$\tau_2 \frac{dr_2(t)}{dt} = -r_2(t) + r_1(t) \quad \text{(A.2)}$$

$$\tau_3 \frac{dr_3(t)}{dt} = -r_{goal} + r_2(t) \quad \text{(A.3)}$$

The function $g()$ is the f-I curve that describes the relation between firing rate and total input. The total input is assumed to be $u(t) - \theta(t)$, where $u(t)$ is the external input current to the neuron, typically from synaptic input, and $\theta(t)$ is the threshold of the neuron. Crucially, this threshold is under homeostatic regulation and thus time dependent. The homeostasis is assumed to act as a bias current which shifts the f-I curve. Rather than reading out the activity directly, the homeostatic controller takes its input from averaged activity $r_2(t)$ which is obtained by filtering the firing rate $r_1(t)$ with a linear first order filter with a time-constant τ_2. Biophysically, the intra-cellular calcium concentration is a very likely candidate for this sensor in which case τ_2 is around 50ms. The final step in the current homeostatic regulation model is to integrate the difference between the average activity and the pre-defined desired activity level, denoted r_{goal}. The feedback loop is closed by setting the threshold equal to this signal, that is $\theta(t) = r_3(t)$. Figure A.1 A shows the schematic representation of the system.

In the limit of small perturbations the system of differential equations is linear. To examine its stability, the results from linear control theory can be applied. One needs to solve the differential equations and check whether the solutions diverge. Various equivalent approaches have been developed to determine stability of controllers [118]. Here the set of first order equations, Eqs.(A.1)-(A.3) in matrix form is written as

$$\frac{d}{dt}\begin{pmatrix} r_1(t) \\ r_2(t) \\ r_3(t) \end{pmatrix} = M \begin{pmatrix} r_1(t) \\ r_2(t) \\ r_3(t) \end{pmatrix} + \mathbf{b}$$

with matrix

$$M = \begin{pmatrix} -\frac{1}{\tau_1} & 0 & -\frac{1}{\tau_1} \\ \frac{1}{\tau_2} & -\frac{1}{\tau_2} & 0 \\ 0 & \frac{1}{\tau_3} & 0 \end{pmatrix}$$

and vector

$$\mathbf{b}(t) = \begin{pmatrix} \frac{1}{\tau_1} u(t) \\ 0 \\ -\frac{1}{\tau_3} r_{goal} \end{pmatrix}$$

The solution to this set of equations is the sum of a particular solution (which is unimportant for our purposes) and solutions to the homogeneous equation, which is the equation with $\mathbf{b} = \mathbf{0}$. Such solution is found by taking the 'ansatz' $r_i(t) = c_i e^{\lambda t}$. The vector $\mathbf{c} = (c_1, c_2, c_3)$ must be an eigenvector of M with eigenvalue λ. This means that λ has to solve the characteristic polynomial, $\det(M - \lambda I) = (1 + \tau_1\lambda)(1 + \tau_2\lambda)\tau_3\lambda + 1 = 0$. The three eigenvalues of M are in general complex numbers and assuming they are distinct, the corresponding eigenvectors (or 'modes') span the space of all possible solutions. The eigenvalue determines the stability of each mode as follows:

- If an eigenvalue is real and negative, the corresponding mode is stable as the exponential $e^{\lambda t}$ decays to zero over time.
- If an eigenvalue is complex and the real part is negative, the corresponding mode decays over time as a damped oscillation. In the context of homeostasis such oscillations in the activity might be biologically undesirable, in particular when they persist for many cycles.
- Finally, the solution will diverge if any of the eigenvalues has a positive real part. In practice, some mechanism, such as a squashing or rectifying f-I curve, will restrain the firing rate and strong non-abating oscillations in the firing rate will occur. This is a situation to be avoided at all cost, because it is almost the opposite of homeostasis as neurons could only code little information, while this state is also energetically costly.

The above options depend exclusively on the relations between the time constants (τ_1,τ_2 and τ_3). Fig. A.1B shows simulated responses of the firing rate $r_1(t)$, and the threshold variable $r_3(t)$ to a step input for various settings of the time-constants. For extremely short values of τ_3 the neuron is unstable (striped region). In the gray region the neuron is stable but displays damped oscillations after changes in the activity. Stability without oscillation (white region) can always be achieved by taking τ_3 slow enough. Keeping the first two time constants fixed, the explicit stability condition following from the Routh–Hurwitz stability criterion [118] is $\tau_3 > \tau_3^{crit}$, where

$$\tau_3^{crit} > \frac{\tau_1\tau_2}{\tau_1 + \tau_2}. \tag{A.4}$$

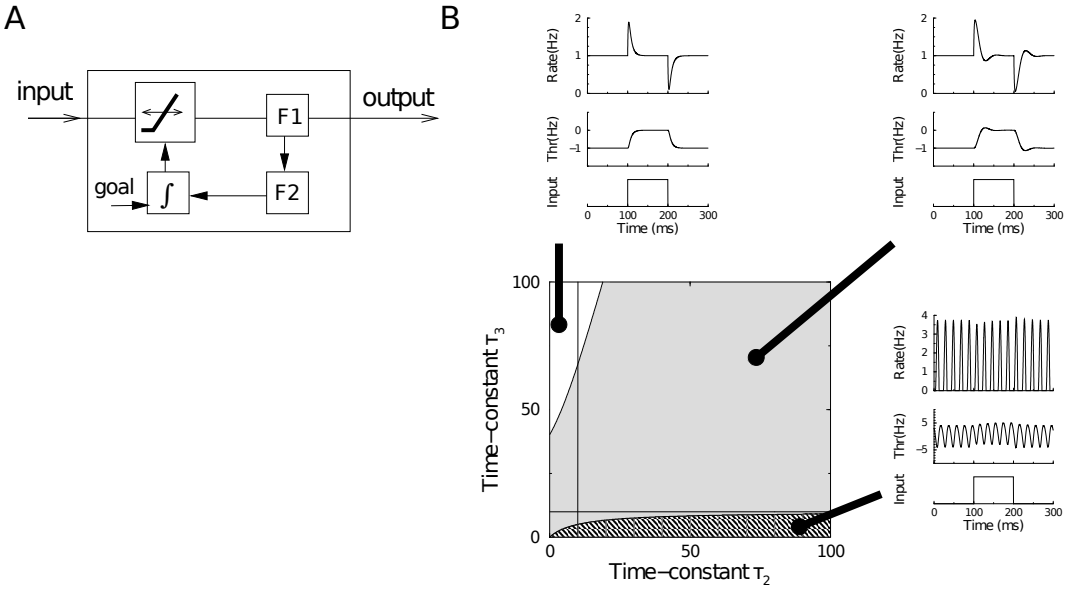

Figure A.1: **Single neuron homeostasis.**

A) Schematic illustration of the homeostatic model. The input current is transformed through an input-output relation and a filter. The input-output curve is shifted by a filtered and integrated copy of the output firing rate, so that the average activity matches a preset goal value.

B) The response of the model for various setting of the homeostatic time-constants. The value of τ_1 was fixed to 10ms (thin lines), while τ_2 and τ_3 were varied. Center plot: the response of the neuron can either be stable (top left plot; white region), damped oscillation (top right plot, gray region), or unstable (bottom right plot, striped region). The surrounding plots show the firing rate of the neuron and the threshold setting in response to a step stimulus.

Figure taken from the paper under revision.

A.2.2 From single neuron to a recurrent neural network

Next a network of N neurons is considered. The network is connected with fast synapses via a $N \times N$ weight matrix W. For ease of presentation W is assumed to be symmetric. In the constructed network a synapse can be excitatory or inhibitory. In the absence of homeostasis the firing rate dynamics obeys

$$\tau_1 \frac{d}{dt}\mathbf{r}_1(t) = (W - I)\mathbf{r}_1(t) + \mathbf{u}(t) \tag{A.5}$$

where $\mathbf{r}_1(t)$ is now a N-dimensional vector containing all firing rates in the network, and $\mathbf{u}(t)$ is a vector of external input to the neurons in the network. The recurrent feedback is contained in the term $W\mathbf{r}_1(t)$. The network activity is stable as long as all eigenvalues of W are less than one. For a given eigenmode with eigenvalue w_n, the recurrent excitatory connectivity slows down the effective time-constant of a given mode to $\tau_1/(1-w_n)$.

In the presence of homeostatic regulation, the system becomes $3N$-dimensional. It is described by the rate of each neuron $\mathbf{r}_1$, its filtered version $\mathbf{r}_2$, and its threshold $\mathbf{r}_3$. The corresponding differential equation is

$$\frac{d}{dt}\begin{pmatrix}\mathbf{r}_1\\ \mathbf{r}_2\\ \mathbf{r}_3\end{pmatrix} = M\begin{pmatrix}\mathbf{r}_1\\ \mathbf{r}_2\\ \mathbf{r}_3\end{pmatrix} + \begin{pmatrix}\frac{1}{\tau_1}\mathbf{u}(t)\\ 0\\ -\frac{1}{\tau_3}\mathbf{r}_{goal}\end{pmatrix}$$

where M is now a block-matrix, given by

$$M = \begin{pmatrix}\frac{1}{\tau_1}(W-I) & 0 & -\frac{1}{\tau_1}I\\ \frac{1}{\tau_2}I & -\frac{1}{\tau_2}I & 0\\ 0 & \frac{1}{\tau_3}I & 0\end{pmatrix} \tag{A.6}$$

We proceed as above to determine the stability of this system. In analogy with the single neuron case, there are three eigenvalues for the full system per eigenvector of W, so that we obtain $3N$ eigenvalues. In principle, one should now research the stability of each W eigenvector. Yet the analysis can be simplified. In a network without homeostasis the most critical mode is the one with the largest eigenvalue. This also holds in networks with homeostasis: the network is stable if and only if this mode is stable. Thus, rather than analyzing the full network, we only need to analyze the stability of this most critical mode, which is given by a three dimensional system similar to the single neuron system studied above with as only modification the pre-factor of $r_1(t)$ on the right hand side,

$$\tau_1 \frac{dr_1(t)}{dt} = [w_m - 1]r_1(t) + u(t) - \theta(t) \tag{A.7}$$

where $w_m = \max(w_n)$ is the maximal eigenvalue of W. The other equations for homeostatic control, Eqs.A.2 and A.3, remain unchanged. The resulting three dimensional system describes the dynamics of the critical eigenmode and its homeostatic variables. The stability is now determined by the roots of the polynomial

$$(1 - w_m + \tau_1\lambda)(1 + \tau_2\lambda)\tau_3\lambda + 1 = 0 \tag{A.8}$$

The network is again stable if all roots have a negative real part. Again the application of the Routh–Hurwitz criterion yields the stability condition $\tau_3 > \tau_3^{crit}$, where

$$\tau_3^{crit} = \frac{1}{1 - w_m}\frac{\tau_1\tau_2}{\tau_1 + (1 - w_m)\tau_2} \tag{A.9}$$

Comparing the stability criterion equation for the network A.9 with the stability criterion equation for the single neuron A.4, one can see that the conditions on homeostatic control are much more stringent for the networks than for single neurons. In particular when the recurrence is very strong ($w_m = 1 - \varepsilon$), the τ_3^{crit} can be many hours.

Here we presumed the f-I relationship of individual neurons in the network is linear with the coefficient 1 ($g(x) = x$) for simplicity. It is easy to show that when the coefficient is different from one ($g(x) = g'x$, $g' > 0$) the τ_3^{crit} defined in equation A.9 changes to

$$\tilde{\tau}_3^{crit} = \frac{g'}{1 - w_m}\frac{\tau_1\tau_2}{\tau_1 + (1 - w_m)\tau_2}. \tag{A.10}$$

$\frac{g'}{1-w_m} \equiv \tilde{g}'$ is the slope of the linear f-I curve of the connected network which directly follows from the steady state solution ($dr_1/dt = 0$) of the equation A.7 in the absence of homeostasis ($\theta(t) = 0$), modified to include the coefficient g':

$$\tau_1\frac{dr_1(t)}{dt} = [w_m - 1]r_1(t) + g'(u(t) - \theta(t)) \tag{A.11}$$

$$r_1 = \frac{g'}{1 - w_m}u(t) = \tilde{g}'u(t) \tag{A.12}$$

A.2.3 Nonlinear system

So far we have only considered the case of the linear f-I curve ($g(x) = x$). i.e. only local stability to small perturbation is guaranteed. It is easy to see how this assumption must break down as negative firing rates are not possible (the curve is truncated at zero) and because neurons are limited with the maximum firing rate (the f-I curve is saturated for large values of input).

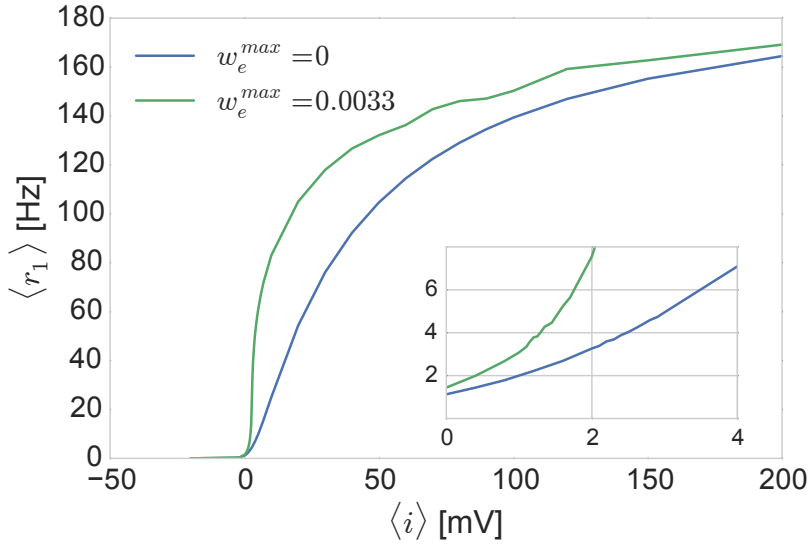

Figure A.2: **f-I curve of the average network activity:** Mean response of a network of 16000 excitatory leaky integrate and fire neurons to a varying noisy input in the case when network is either connected (green) or unconnected (blue - the f-I curve corresponds to the f-I curve of a single neuron). The neurons in the connected network are connected randomly with the 2% probability of connection. The input is white noise given to all neurons, where its mean value is expressed as the average membrane voltage an individual neuron would reach (relative to its resting voltage) if the spiking mechanism was turned off. For both cases the response is nonlinear – non-negative for negative input and saturated in the case of strong input. The connected network has a stronger response to the input than the unconnected network.
The inset figure is close-up to the region of interest around the default target firing rate of 4Hz.

For the case of a non-linear f-I curve it can be shown that only when

$$0 < \frac{\sigma(x)}{x} < \frac{\tau_3}{(1-w_m)\tau_3^{crit}} \qquad \forall x \in \mathbb{R} \tag{A.13}$$

the system is guaranteed to be stable. Here $\sigma(x)$ is defined as the re-centered f-I curve of the connected network such that the origin $\sigma(x=0)=0$ corresponds to the set-point of the homeostasis. The criterion is known as the Aizerman conjecture [119], and although not generally true, it is known to hold for this particular 3 dimensional system [120]. Note that for a linear system $\sigma(x)/x$ is constant ($\tilde{g'}$) one retrieves Eq. A.10.

A.3 Spiking neural network

A.3.1 Simulations and analysis

I simulate a network of 16000 excitatory leaky integrate and fire neurons. They are randomly interconnected with the probability of connection $p = 0.02$ (the exact connectivity is randomly redrawn for each simulation). The connections are excitatory and modeled as exponentially decaying synapses with the time constant τ_e=5ms and the maximum conductance (w_e^{max}).

In addition I introduce a homeostatic current (hr_3) which drives the neurons towards a target firing rate. The dynamics of each neuron in the network thus follows

$$\frac{dV(t)}{dt} = \frac{(V_{rest}-V) + g_e(V_e-V) + i(t) - hr_3}{\tau_m} \tag{A.14}$$

$$\frac{dg_e(t)}{dt} = \frac{-g_e + w_e \sum_i \delta(t-t_i)}{\tau_e} \tag{A.15}$$

$$\frac{dr_2(t)}{dt} = -\frac{r_2}{\tau_2} + \frac{1}{\tau_2^2}\sum_k \delta(t-t_k) \tag{A.16}$$

$$\frac{dr_3(t)}{dt} = \frac{r_2 - r_g}{\tau_3} \tag{A.17}$$

where V is the neuron membrane voltage and $g_e(t)$ is the total excitatory conductance. The conductive input is caused by the spikes in the presynaptic neurons (t_i represents the presynaptic spike times from neurons in the population). As the membrane voltage reaches the threshold voltage (V_{thr}), the neuron emits a spike and its voltage is clamped to V_{rest} for the refractory period of $5ms$. r_2 represents the filtered firing rate of the neuron which is computed in Eq. A.16 while r_g is the target value for the neuron

firing rate. r_3 is the integrated difference between the filtered neuron rate and the target rate. h is the homeostatic strength factor in mV/Hz. It is set to 1 when homeostasis is present and to 0 in the simulations without homeostasis. To prevent synchrony each neuron also receives a noisy external input $i(t)$ (an independent white noise drawn from the uncorrelated multivariate normal distribution with mean $\langle i \rangle$ and standard deviation std_{inp} for each neuron). The mean value of the external input $i(t)$ is expressed as the average membrane voltage an individual neuron would reach (relative to its resting voltage) if the spiking mechanism was turned off.

The default parameter values are given in Table A.1. These are the values used in all simulations unless specified differently in the description of the figure. The simulations were performed using the Brian simulator [37] with the time step of 0.1 ms. The default target firing rate is set to $r_g = 4$Hz.

number of neurons	N	16000
resting and reset potential	V_{rest}	-60 mV
input reversal potential	V_e	0 mV
spiking threshold potential	V_{thr}	-50 mV
homeostatic strength factor	h	1 mV/Hz
membrane time constant	τ_m	20 ms
maximum synaptic input conductance	w_e^{max}	0.0033
input decay time constant	τ_e	5 ms
time constant of the first filter	τ_2	50 ms
time constant of the second filter	τ_3	50 ms
target homeostatic firing rate	r_g	4 Hz
standard deviation of external input	std_{inp}	75 mV

Table A.1: Default parameter values for the network simulation.

Most of the analysis is performed on the population firing rate ($\bar{r}(t)$) of the network. The rate is calculated by binning the spikes of all the neurons. When calculating the the standard deviations of population firing rate ($std(\bar{r})$) the time window of 1ms is used for the binning.

To measure the I/f curves I turn the homeostatic current off ($h = 0mv/Hz$) and measure the time-averaged mean population firing rate $\langle \bar{r} \rangle$ for different mean input currents.

A.3.2 Rate-based approximation

For the spiking network in such an asynchronous regime, the population firing rate of the spiking network can be reasonably approximated by the rate equation A.1, where r_1 now denotes the network population firing rate (or a mean firing rate of a neuron averaged over the whole population). However the f-I curve $g()$ is nonlinear (see figure A.2) and the input includes the recurrent feedback. We can thus rewrite the equation A.1 to

$$\tau_1 \frac{dr_1(t)}{dt} = -r_1(t) + g(wr_1 + u(t) - \theta(t)), \tag{A.18}$$

where w is the recurrence coefficient depending on the network connectivity (in our case both the connection probability as well as the connection strength) and is related to the maximum eigenvalue of the connectivity matrix w_m introduced in section A.2.2.

For the case of small deviations from the target firing rate r_g we can linearize the f-I curve ($g()$) of the system around the target firing rate. The equation (A.18) in the absence of homeostasis ($\theta(t) = 0$) then becomes

$$\tau_1 \frac{d\tilde{r}_i(t)}{dt} = -\tilde{r}_1(t) + g'w\tilde{r}_1(t) + g'\tilde{u}(t) - g'\theta(t) = [g'w - 1]\tilde{r}_1(t) + g'(\tilde{u}(t) - \theta(t)), \tag{A.19}$$

where $\tilde{r_1} = r_1 - r_g$ is the rate relative to the target rate, $\tilde{u} = u - u^*$ is the external input relative to the amount of external input required for the connected network to achieve the target firing rate (u^*) and $g' = g'(x)|_{x=g^{-1}(r_g)}$ is the gradient of the underlying f-I curve at the total input which leads to the target firing rate (where $g()$ is the f-I curve for the unconnected network or in our case of a homogenous population also the f-I curve for a single neuron). Now the rate-based approximation (A.19) corresponds to the equation (A.7) derived for the linear network. Here the maximum eigenvalue of W (w_m) from the equation (A.7) is substituted by $g'w$ and the external and homeostatic inputs are multiplied by the factor g'.

The linear criteria for the stability for the approximated system can then be expressed as in the linear case of the rate-based network (see Eq. (A.10))

$$\tau_3^{crit} = \frac{g'}{1 - \hat{w}} \frac{\tau_1 \tau_2}{\tau_1 + (1 - \hat{w})\tau_2}, \tag{A.20}$$

where $\hat{w} \equiv g'w$ is a modified recurrence coefficient.

A.3.3 Estimating the effective time constant and modified recurrence factor

For given connectivity parameters of the network (connection probability p and maximum synaptic input conductance w_e^{max}) the modified recurrence coefficient $\hat{w}$ can be estimated in different ways by observing the network response to the input in the absence of the homeostasis. In the following part three such methods are presented. First one estimates $\hat{w}$ through the network time constant, the other two estimate it through examining the f-I curves of the unconnected and connected network.

Method 1: Estimation based on the network time constant One way to estimate the modified recurrence coefficient $\hat{w}$ is to determine the time course of the relaxation of network activity when we change the external input from u^* (the amount of input required to keep the network firing rate at the set point) to $u^* + du$ in the absence of homeostasis ($\theta(t) = 0$). If the change of the input is small (so the linear approximation holds) and instantaneous (a step function), then the firing rate r_1 will relax to the new value exponentially with the characteristic time $\tilde{\tau}_1 = \frac{\tau_1}{1-\hat{w}}$ according to the solution of the differential equation (A.19) (but with $\theta(t) = 0$).

I did such an estimation for the network of $N = 16000$ neurons (default simulation is described in the section A.3.1). The results are presented in figure A.3. The estimations were done for the set-point $r_g = 4Hz$ and the instantaneous change of the external current was chosen to increase the network firing rate to 6Hz (fig. A.3 left) or to decrease it to 2Hz (fig. A.3 right). In all of these simulations the homeostasis was turned off ($h = 0$). To change the recurrence of the network, the maximum synaptic input conductance w_e^{max} was varied. For each case the network firing rate response was averaged over 10 simulations and then fitted with the exponential curve to estimate the characteristic time constant. Finally the dependence of $\tilde{\tau}_1$ on the recurrence was fitted according to the linear approximation $\tilde{\tau}_1 = \frac{\tau_1}{1-\hat{w}}$ to derive the relationship between w_e^{max} and $\hat{w}$.

In the bottom plots of fig. A.3 the black arrows are pointing to the default maximum synaptic input conductance value of $w_e^{max} = 0.0033$. The estimated values of $\hat{w}$ for this connectivity are $\widehat{w} \approx 0.62$ for the case of increased firing rate and $\widehat{w} \approx 0.42$ for the case of the decreased firing rate. The difference is likely due to the intrinsic nonlinearity of the underlying f-I curve $g()$ and the relative large change in the external inputs (50% increase and decrease of firing rates). Decreasing the absolute change in the external

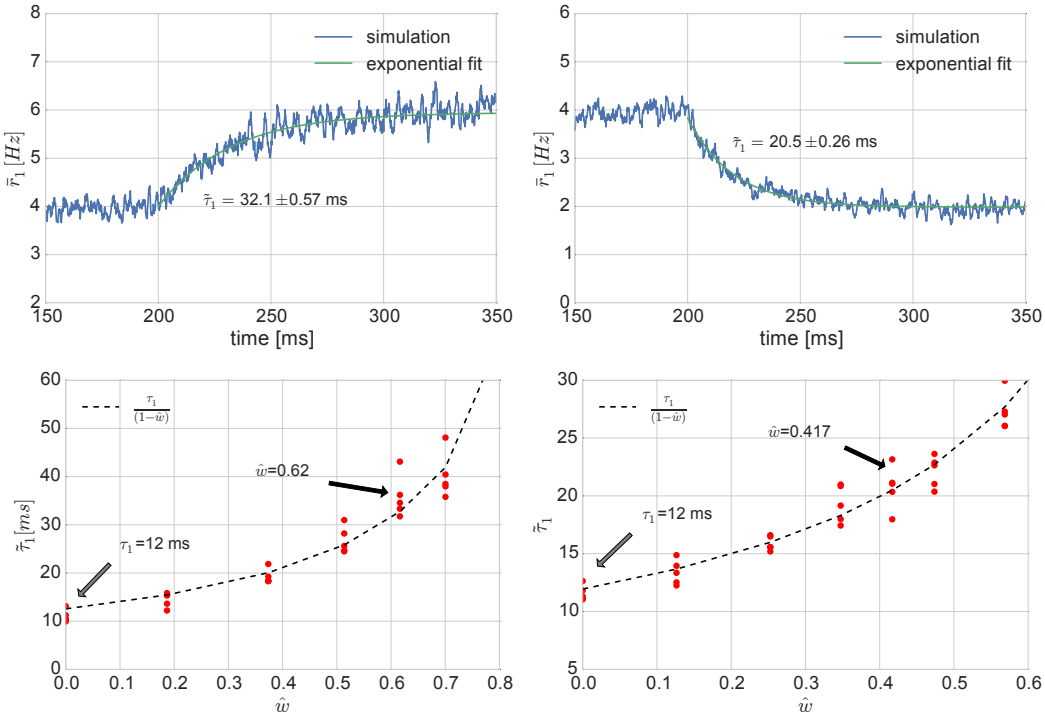

Figure A.3: **The estimations of $\hat{w}$ and τ_1 (method 1).**
(top) Example of the fitting of the characteristic time constant of the network activity ($\tilde{\tau}_1$) when we apply a step increase (left) or a step decrease (right) of the external input for a network with a default connectivity parameters ($p = 0.02$, $w_e^{max} = 0.0033$).
(bottom) Each red dot represents a network time constant $\tilde{\tau}_1$ for a specific connectivity strength, measured by the external input change causing the increase of the stable network rates from 4Hz to 6Hz (left) or causing the decrease of network rates from 4Hz to 2 Hz (right) and fitting the time course of the response by an exponential curve. The $\widehat{w}$ is estimated based on the resulting time constants as per the equation given in the figure. The black arrows indicates the default connectivity strength chosen for the further simulations ($w_e^{max} = 0.0033$). The estimates based on the input increase and the input decrease differ in value for the same connectivity strength ($\widehat{w} \approx 0.62$ and $\widehat{w} \approx 0.42$ measured by input increase and decrease respectively). Measuring the network time constant of a non-connected network $\tau_1 = \tilde{\tau}_1(\widehat{w} = 0)$ we get $\tau_1 = 12 \pm 2$ ms (indicated by gray arrows in the figure).

inputs would make it hard to estimate the characteristic relaxation times. Finally given the monotonic nonlinearity of the f-I curve around the set-point (see the inset in figure A.2), the modified recurrence coefficient is likely to lie between the two estimated values.

The time constant for the unconnected network is estimated to $\tau_1 = 12 \pm 2$ ms and matches both cases (gray arrows in figure A.3, where $\hat{w} = 0$).

Methods 2 and 3: Estimation based on the f/I curves As shown in the figure A.2 the f-I curve of the connected network is different from the f-I curve of the unconnected network. If we take the approximated linearized equation for the connected network activity (A.19) in the absence of homeostasis ($\theta = 0$) and look at the steady state ($\frac{dr_1(t)}{dt} = 0$) we can express $\tilde{r}_1$ as

$$\tilde{r}_1 = \frac{g'}{1 - g'w}u = \frac{g'}{1 - \hat{w}}u \equiv \tilde{g}'u. \tag{A.21}$$

This is an expression for the approximate linear activity of the connected network around the set-point ($r_1 = r_g$). $\tilde{g}'$ represents the gradient of the f-I curve of the connected network around the set-point. Since it is possible to measure the gradients of both unconnected and connected networks, this can be used as another way to estimate the modified recurrence factor $\hat{w} = \frac{\tilde{g}' - g'}{\tilde{g}'}$ (method 2).

I show the f-I curves and the estimation of their gradients around the set-point ($r_g = 4Hz$) in figure A.4. According to the estimated gradient values for our default connectivity ($g' \approx 1.64$, $\tilde{g}' \approx 3.19$) the modified recurrence coefficient is $\hat{w} \approx 0.49$, which is within the interval $[0.42, 0.62]$ obtained by the method 1.

All those estimations relied on the specific set-point. To relax this constraint and verify that the estimation of the recurrent coefficient applies across different set-points I estimated the f-I curve of the connected network ($\tilde{g}()$) using the measured f-I curve of the connected network ($g()$) and a recurrent connectivity coefficient w (method 3). To do that I numerically solved the static state of the equation (A.18) in the absence of homeostasis $r_1(t) = g(wr_1 + u(t))$ for different values of w. The bottom plot in figure A.4 shows the fit between the numerically estimated f-I curve (dashed line) and the f-I curve measured in the simulations of the connected network (green line) for the best matching value of $w = 0.29$. Combining this result with the estimation of the gradient of the f-I curve of the unconnected network around the set-point $g' \approx 1.62$, we get $\hat{w} = g'w \approx 0.49$ which fits exactly with the estimations from the previous two methods.

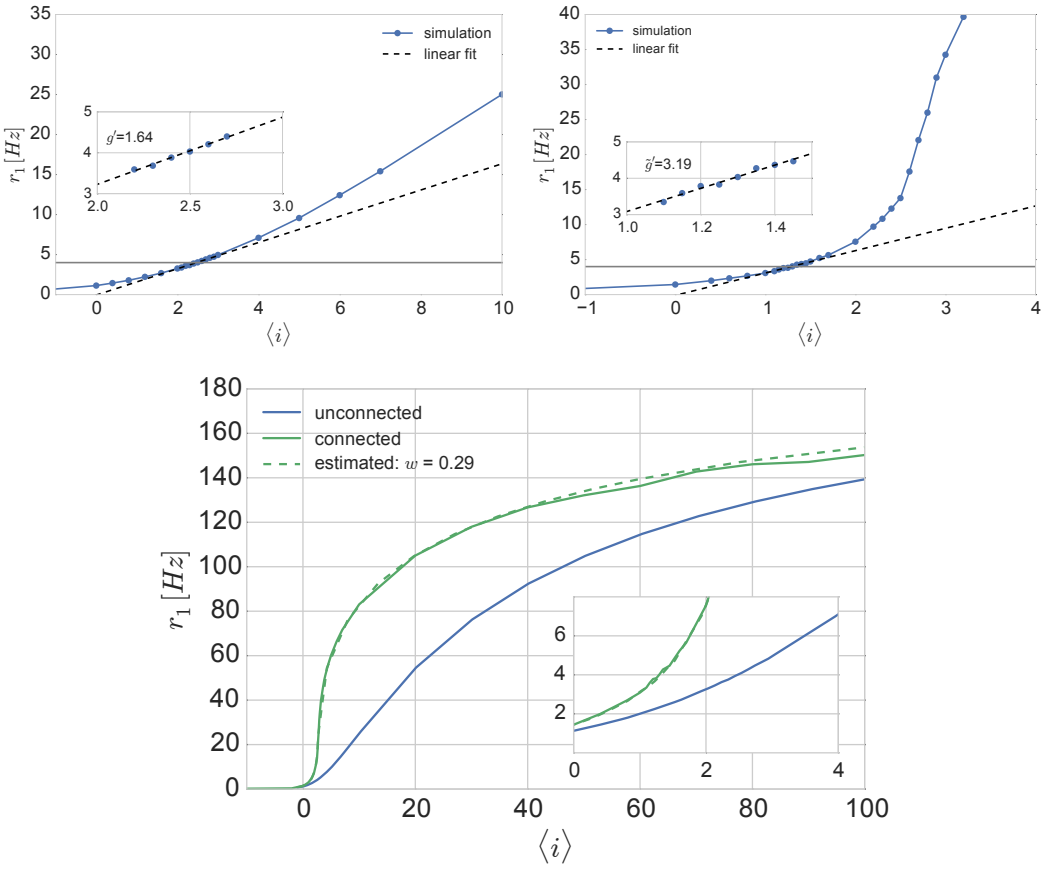

Figure A.4: **The estimations of $\hat{w}$ (methods 2 and 3).**

(left - method 2) Estimation of the gradient of the f-I curve of the unconnected network around the set-point (the horizontal gray line). The f-I curve was measured by simulating the network activity in the absence of homeostasis ($h = 0$) at different levels of the mean input current (blue dots).

(right) Same as left but for the connected network. The two gradient values give us the estimation for $\hat{w} \approx 0.49$.

(bottom - method 3) Numerical estimation of the f-I curve of the connected network (dashed green line) using the measured f-I curve of the unconnected network (blue line) and the best fitting recurrent connectivity coefficient $w = 0.29$ (corresponding to $\hat{w} \approx 0.49$). The numerical estimation for this recurrent connectivity coefficient fits well with the measured f-I curve of the connected network (solid green line).

A.3.4 The stability criteria

In section (A.2) we presented two separate criteria for the stability of the recurrent system under homeostasis. How does the activity of the recurrent spiking network correspond to those criteria?

The first criteria was developed for the rate-based system with the assumption of the linear response of neurons ($g(x) = g'$, where g' is a constant of x) and sets a limit on how small the homeostatic time constant τ_3 can be (Equation A.9) to still have a system that achieves asymptotic stability. Taking the firing rates of the excitatory spiking network (r_1) averaged over all the neurons I approximated the dynamics of the system (A.18) and linearized it around the target firing rate (A.19) to be able to apply the linear criteria (A.20). Here I defined the modified recurrence coefficient $\hat{w}$ which indicates the strength of the network connectivity and needs to be smaller than 1 for the network to be stable even in the absence of homeostasis. Once I estimated the coefficient $\hat{w}$ and the network time constant τ_1 the critical homeostasis time constant $\tau_3^{crit_{lin}}$ for the target firing rate ($r_g = 4Hz$) was estimated to $52 \pm 10ms$ (figure A.5 - top left). Given that the f-I curve of the spiking network is not linear, the criterion is only valid for small perturbations around the target firing rates and as such can only serve as the lower bound on the critical time constant required for a global stability.

The second, more strict, criteria is developed for the rate-based system with the non-linear response of neurons according to the Aizerman conjecture (equation A.13). For our rate-based approximation of the spiking network the critical value for τ_3 according to this criterion is

$$\tau_3^{crit_{aiz}} = \frac{\tau_1\tau_2}{\tau_1 + (1 - \hat{w}\tau_2)} \max(\frac{\sigma(x)}{x}). \tag{A.22}$$

The calculated critical value for the default network using the estimations of $\hat{w}$, τ_1 and $\max(\frac{\sigma(x)}{x})$ is presented in figure A.5 (top right). $\max(\frac{\sigma(x)}{x})$ is estimated by measuring the f-I relation of the connected network in the absence of homeostasis (bottom plots in figure A.5). According to those estimations the critical τ_3 value is $\tau_3^{crit_{aiz}} = 300 \pm 100$ms. Note that this is a sufficient but not necessary criterion, and as such provides an upper bound on the critical time constant required for the global stability.

Simulations of the network with the homeostasis turned on correspond well with the predictions. Firstly we see the homeostasis can destabilize the network by comparing the variability of network activity 2.5s after a step increase in the external input

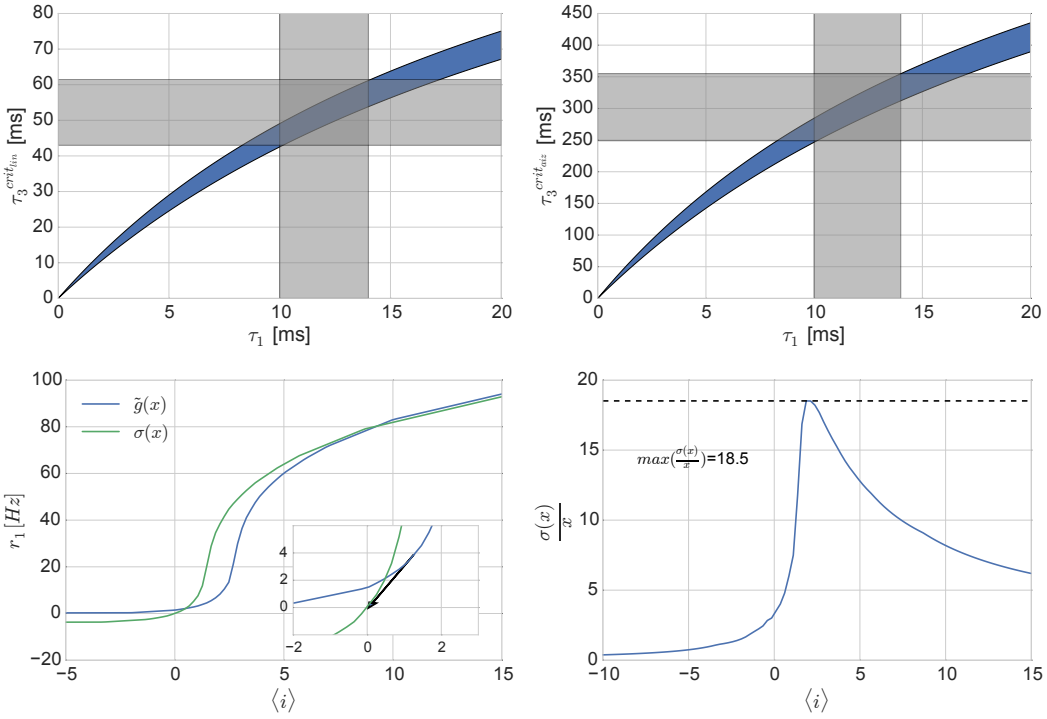

Figure A.5: **The critical τ_3 values.**

(top) The theoretical estimations of the critical τ_3 values as a function of τ_1 for the linear (left, Eq. A.10) and nonlinear (Aizenman) criteria (right, Eq. A.22). First the blue areas are calculated based on the default parameter values (τ_2 = 50 ms) and the estimations of $\hat{w} = 0.49 \pm 0.05$, $g' = 3.19$ and $\max(\frac{\sigma(x)}{x}) = 18.5$, according to the equations (A.20) and (A.22) for left and right plot respectively. Using the estimation $\tau_1 = 12 \pm 2ms$ we can then read out the critical values for the linear criteria ($52 \pm 10ms$) and for the nonlinear Aizerman criteria ($300 \pm 50ms$) - represented by the gray shading.

(bottom) Determining the criterion for the nonlinear case. (left) Function $\sigma(x)$ is defined as the re-centered f-I curve of the connected network ($\tilde{g}(x)$) so that the $\sigma(x = 0) = 0$ corresponds to the set-point of the homeostasis. (right) Determining $max(\sigma(x)/x)$ used in the calculation of the critical τ_3 value.

(figure A.6 - top left) with the variability of the network activity at the same mean activity level ($4Hz$). This also allows for empirical estimation of the critical τ_3 value (~210 ms).

As expected due to the nonlinear nature of the system, the empirical critical value is higher than the theoretical linear criterion ($\tau_3^{crit_{lin}} = 52 \pm 10ms$). Compared to the Aizerman conjecture criterion the empirical critical value is smaller - however, it should again be noted that the criterion for stability is not tight. Thus networks for which one cannot prove stability *can* nevertheless be stable; this is a well-known property of non-linear control theory. The top right plot of the figure A.6 graphically expresses the theoretical and empirically observed criteria for stability.

The bottom plots of A.6 show the activity of the network for various values of τ_3 (left) and the power spectrum of the activity (right). We can see the oscillations for the small τ_3 values. The amplitude of oscillations is dropping as τ_3 increased until the stability is achieved. Interestingly the frequency of the oscillations corresponds to the target firing rate (4 Hz), which is the direct result of fast homeostasis pushing individual neurons to fire at 4 Hz.

A.4 Discussion

In this chapter I have considered instabilities in the neural activity due to homeostasis of intrinsic excitability, focussing on how the theoretical predictions in rate-based systems translate to the activities in the excitatory spiking network which has a non-linear input-output relationship.

In the worst case, homeostasis can lead to continuous oscillations of the activity. Homeostasis can also lead to damped oscillations in the activity, which are less disastrous to information processing, provided the oscillations don't persist too long. To our knowledge such damped oscillations in the homeostatic response have not been observed experimentally, although averaging of experimental data could have obscured their detection.

The control theoretic framework for homeostasis sets precise constraints on homeostatic control to prevent the instability in the case of the linear input-output relationship. While a typical single neuron model with just two filters in the feedback loop has no stability issues even when the homeostatic control is very fast this is no longer true when network interactions are included. The stronger the recurrence of the network, the slower the feedback needs to be (Eq. A.10). Networks with time-constants on the

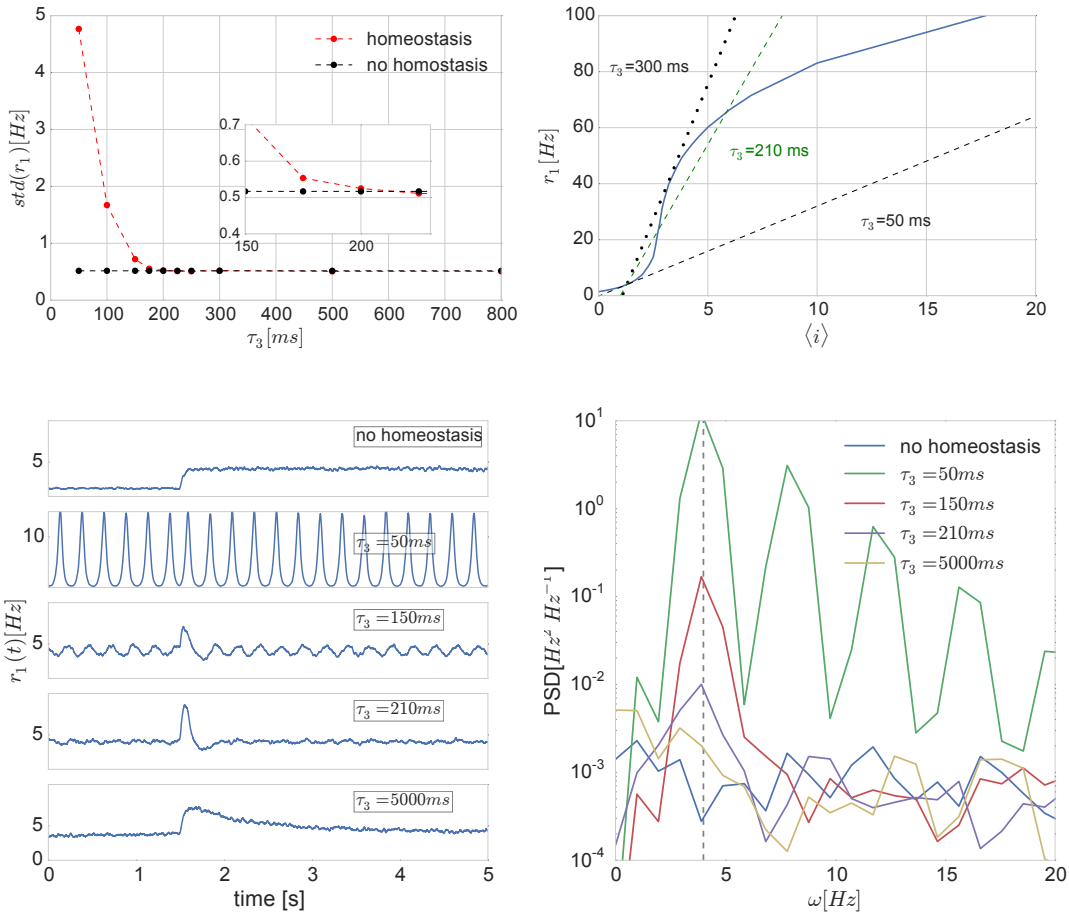

Figure A.6: **Effect of homeostasis for different values of τ_3**

(top left) Determining the empirical τ_3^{crit} from the variability of the population rates 2.5 s after a step increase in stimulus for different values of τ_3. At about $\tau_3 = 210$ ms the variability in firing rates drops down to the variability of the network without homeostasis indicating the network is in a stable state.

(top right) The f-I curve and the stability criterion. The solid curve shows the f-I curve of the connected network ($\tilde{g}()$) as determined from the simulations with homeostasis turned off. The various lines have a slope proportional to τ_3. According to linear theory stability the minimal τ_3 required is given by the slope at the set point (dashed line). Stability of a system with a non-linear f-I curve requires the time-constant to be such that the line encompasses the f-I curve - the Aizerman criteria (dotted line). In practice stability is achieved for a slightly smaller value of τ_3 (green dashed line).

(bottom) Example of the network activity following a step stimulus for different interesting values of τ_3 (left) and the power spectra of those activities (right).

order of seconds have been proposed to explain sensory evidence integration, decision making and motor control [121, 122]. As the minimal homeostatic time constant for oscillation-free homeostasis scales quadratically with the network time-constant, the required homeostatic time-constant becomes of the order of hours, which is comparable to experimentally observed homeostatic action [110, 116, 112, 117].

In addition, the condition for stability if the neuronal input-output relationship is non-linear (a non-linear f-I curve) is described. A non-linear f-I curve further limits the minimal homeostatic time-constant. Ideally, one would like to know the stability requirements for any given non-linear homeostatic controller. However, only in a very limited number of cases extensions of our mathematical results to either multiple non-linearities in the control loop or to higher dimensional systems (i.e. with longer feedback cascades) are known. We describe a sufficient (but not necessary) condition for the stability of the system with two linear filters in the feedback loop based on the Aizerman conjecture (Eq. A.22) which gives an upper bound for the minimal homeostatic time constant.

The described limits are explored in the case of an excitatory recurrent spiking network. To be able to do the comparison with the theoretical predictions we first approximate the dynamics of the network with a one-dimensional rate-based model. The parameters of the approximated model (network time constant, modified recurrence factor) are estimated from simulations of the network activity in the absence of homeostasis. A specific connectivity ($\hat{w} \approx 0.49$) and target firing rate ($r_g = 4Hz$) are chosen for the exploration of homeostatic effects in the network. As predicted from the theoretical rate models the spiking network exhibits unstable behavior (oscillations) for a fast homeostatic time constant. The criterion derived from the linear approximation is not sufficient to stabilize the network, while the criterion based on the Aizerman conjecture demands a slower homeostatic time constant than what we observed empirically. This still fits with the theory, as the criterion is not supposed to give a tight bound.

While we see the activity undershoot caused by a homeostatic response to an increase in input (see figure A.6) we do not observe any prolonged dampened oscillations as predicted by the theory. The reason for this could be the intrinsic variability of the individual neuron activities which desynchronize the oscillatory activity. Furthermore, unless the spiking network is silent, it is never really static (as its activity is essentially a collection of discrete events) so the input to an individual neuron is never stable. This non-static input can be viewed as a constant collection of small perturbations which

makes it hard to clearly distinguish the stable regime from the regime of dampened oscillations. One way to address this is to look at the power spectral density of the network activity. As the homeostasis mechanism is applied to individual neurons it not only forces each neuron's spiking frequency to the frequency of the target firing rate but also makes the spiking regular if the homeostasis is fast enough (the coefficient of inter-spike interval becomes small). Those regular spikes of individual neurons are synchronized by the network which leads to the oscillations on the network level at the same frequency as the target firing rate. We can therefore look for the signature of the homeostasis in the power spectral density of the network activity (figure A.6). Even for the case where the network was empirically determined to be stable ($\tau_3 = 210ms$, purple line) we can still see the increased power at the frequency of the target firing rate.

Stability of homeostatic control has been the main consideration in this study. This is of course of utmost importance biologically, but it is unlikely to be the only criterion. Another reason for slow homeostasis is that it would allow the processing of slow varying stimuli; homeostasis filters out all fluctuations slower than its response time.

A very simple fast homeostasis could lead to a system in which nothing changes eliminating all possibilities for any information processing. Such naïve homeostasis would go against the observed heterogeneities in intrinsic properties of cells over a defined brain region [123]. On the other hand, heterogeneities in the homeostatically regulated conductance profiles of coupled neurons can lead to heterogeneities even when target activity levels are identical [124].

There can also be cases where rapid acting homeostasis is needed. For instance, one might want to minimize periods of prolonged hyperactivity, while in a recent study fast *synaptic* homeostasis was required to counter synaptic plasticity [125]. It suggests that homeostatic control is constrained "from below and from above", and therefore more finely tuned than previously thought. Unfortunately data on the time-course of the homeostasis of intrinsic excitability, its mediators and regulation cascade is limited, hindering a direct comparison of data to our analysis. Nevertheless a prediction that follows from this work is that homeostasis should be slower in brain regions with strong recurrent connections and long network integration times.

The introduced framework is very general. A recent study examined simple homeostatic control for a network with separate excitatory and inhibitory populations and found that excitatory neurons require faster homeostasis than inhibitory neurons [126]. Our results can be used to extend those results to more realistic control loops. Other

targets for extension and application of this theory include the effect of neuronal heterogeneity, excitatory/inhibitory balanced networks, controllers with a combination of parallel and sequential slow and fast components, as well models that include dynamical synapses. Finally, these results might be important for other regulatory feedback systems such as synaptic homeostasis and spike frequency adaptation.

Bibliography

[1] Kandel, E. R, Schwartz, J. H, Jessell, T. M, Siegelbaum, S. A, & Hudspeth, A. J. (2012) *Principles of Neural Science, Fifth Edition*. (McGraw-Hill Medical, New York), 5 edition edition. (Cited on page 1.)

[2] Dayan, P & Abbott, L. F. (2005) *Theoretical Neuroscience: Computational and Mathematical Modeling of Neural Systems*. (The MIT Press), 1 edition. (Cited on pages 1 and 105.)

[3] Rieke, F, Warland, D, Steveninck, R. d. R. v, & Bialek, W. (1999) *Spikes: Exploring the Neural Code*. (The MIT Press). (Cited on pages 1 and 10.)

[4] Gerstner, W & Kistler, W. M. (2002) *Spiking Neuron Models: Single Neurons, Populations, Plasticity*. (Cambridge University Press, Cambridge, U.K. ; New York). (Cited on pages 1, 10, 63, and 105.)

[5] White, E. L. (2012) *Cortical Circuits: Synaptic Organization of the Cerebral Cortex Structure, Function, and Theory*. (Birkhäuser), Softcover reprint of the original 1st ed. 1989 edition edition. (Cited on pages 1, 60, and 104.)

[6] Izhikevich, E. M. (2006) *Dynamical Systems in Neuroscience: The Geometry of Excitability and Bursting*. (MIT Press), 1 edition. (Cited on pages 1 and 63.)

[7] Segev, I, Rinzel, J, & Shepherd, G. M, eds. (1994) *The Theoretical Foundations of Dendritic Function: The Selected Papers of Wilfrid Rall with Commentaries*. (The MIT Press, Cambridge, Mass), 1 edition edition. (Cited on pages 2, 7, 36, and 62.)

[8] Koch, C. (2004) *Biophysics of Computation: Information Processing in Single Neurons*. (Oxford University Press, USA), 1 edition. (Cited on pages 2, 4, 7, 10, 16, 35, 36, 38, 40, and 46.)

[9] London, M & Häusser, M. (2005) Dendritic computation. *Annual Review of Neuroscience* **28**, 503–532. (Cited on pages 2, 5, 65, 107, and 108.)

[10] Gulledge, A. T, Kampa, B. M, & Stuart, G. J. (2005) Synaptic integration in dendritic trees. *Journal of Neurobiology* **64**, 75–90. (Cited on pages 2, 107, and 108.)

[11] Brunel, N, Hakim, V, & Richardson, M. J. (2014) Single neuron dynamics and computation. *Current opinion in neurobiology* **25**, 149–155. (Cited on pages 4 and 105.)

[12] Gerstner, W & Naud, R. (2009) How Good Are Neuron Models? *Science* **326**, 379–380. (Cited on pages 4, 10, and 17.)

[13] Hinton, G, Deng, L, Yu, D, Dahl, G, Mohamed, A.-r, Jaitly, N, Senior, A, Vanhoucke, V, Nguyen, P, Sainath, T, & Kingsbury, B. (2012) Deep Neural Networks for Acoustic Modeling in Speech Recognition. *Signal Processing Magazine*. (Cited on page 4.)

[14] Krizhevsky, A, Sutskever, I, & Hinton, G. E. (2012) in *Advances in Neural Information Processing Systems 25*, eds. Pereira, F, Burges, C. J. C, Bottou, L, & Weinberger, K. Q. (Curran Associates, Inc.), pp. 1097–1105. (Cited on page 4.)

[15] Rall, W. (1964) in *Neural Theory and Modeling*. (Stanford Univ. Press.). (Cited on pages 4 and 36.)

[16] Kumar, A, Rotter, S, & Aertsen, A. (2010) Spiking activity propagation in neuronal networks: reconciling different perspectives on neural coding. *Nature Reviews Neuroscience* **11**, 615–627. (Cited on page 5.)

[17] Larkum, M. E, Nevian, T, Sandler, M, Polsky, A, & Schiller, J. (2009) Synaptic Integration in Tuft Dendrites of Layer 5 Pyramidal Neurons: A New Unifying Principle. *Science* **325**, 756 –760. (Cited on pages 5, 65, 98, and 107.)

[18] Branco, T, Clark, B. A, & Häusser, M. (2010) Dendritic discrimination of temporal input sequences in cortical neurons. *Science (New York, N.Y.)* **329**, 1671–1675. (Cited on pages 5 and 98.)

[19] Branco, T & Häusser, M. (2011) Synaptic Integration Gradients in Single Cortical Pyramidal Cell Dendrites. *Neuron* **69**, 885–892. (Cited on pages 5 and 98.)

[20] Schiller, J, Major, G, Koester, H. J, & Schiller, Y. (2000) NMDA spikes in basal dendrites of cortical pyramidal neurons. *Nature* **404**, 285–289. (Cited on pages 5, 65, and 107.)

[21] Neher, E & Sakmann, B. (1976) Single-channel currents recorded from membrane of denervated frog muscle fibres. *Nature* **260**, 799–802. (Cited on pages 5 and 9.)

[22] Hamill, O. P, Marty, A, Neher, E, Sakmann, B, & Sigworth, F. J. (1981) Improved patch-clamp techniques for high-resolution current recording from cells and cell-free membrane patches. *Pflügers Archiv: European Journal of Physiology* **391**, 85–100. (Cited on pages 5 and 9.)

[23] Hirsch, J. A, Alonso, J. M, Reid, R. C, & Martinez, L. M. (1998) Synaptic integration in striate cortical simple cells. *The Journal of Neuroscience: The Official Journal of the Society for Neuroscience* **18**, 9517–9528. (Cited on pages 7, 10, 60, 64, 101, and 103.)

[24] Anderson, J. S, Carandini, M, & Ferster, D. (2000) Orientation Tuning of Input Conductance, Excitation, and Inhibition in Cat Primary Visual Cortex. *Journal of Neurophysiology* **84**, 909–926. (Cited on pages 7, 9, 10, 60, 64, 101, and 103.)

[25] Rudolph, M & Destexhe, A. (2005) An Extended Analytic Expression for the Membrane Potential Distribution of Conductance-Based Synaptic Noise. *Neural Computation* **17**, 2301–2315. (Cited on page 7.)

[26] Koch, C, Douglas, R, & Wehmeier, U. (1990) Visibility of synaptically induced conductance changes: theory and simulations of anatomically characterized cortical pyramidal cells. *The Journal of Neuroscience* **10**, 1728–1744. (Cited on pages 7 and 104.)

[27] Haider, B, Häusser, M, & Carandini, M. (2013) Inhibition dominates sensory responses in the awake cortex. *Nature* **493**, 97–100. (Cited on pages 7, 23, and 60.)

[28] Margrie, T. W, Brecht, M, & Sakmann, B. (2002) In vivo, low-resistance, whole-cell recordings from neurons in the anaesthetized and awake mammalian brain. *Pflügers Archiv: European Journal of Physiology* **444**, 491–498. (Cited on page 9.)

[29] Borg-Graham, L, Monier, C, & Frégnac, Y. (1996) Voltage-clamp measurement of visually-evoked conductances with whole-cell patch recordings in primary visual cortex. *Journal of Physiology, Paris* **90**, 185–188. (Cited on pages 9, 101, and 103.)

[30] Rudolph, M, Piwkowska, Z, Badoual, M, Bal, T, & Destexhe, A. (2004) A Method to Estimate Synaptic Conductances From Membrane Potential Fluctuations. *Journal of Neurophysiology* **91**, 2884–2896. (Cited on pages 9, 31, 64, 101, 103, 104, and 105.)

[31] Kobayashi, R, Shinomoto, S, & Lansky, P. (2011) Estimation of Time-Dependent Input from Neuronal Membrane Potential. *Neural Computation* **23**, 3070–3093. (Cited on page 9.)

[32] Kobayashi, R, Tsubo, Y, & Shinomoto, S. (2009) Made-to-order spiking neuron model equipped with a multi-timescale adaptive threshold. *Frontiers in Computational Neuroscience* **3**, 9. (Cited on pages 10 and 17.)

[33] Sterratt, D, Graham, B, Gillies, A, & Willshaw, D. (2011) *Principles of Computational Modelling in Neuroscience*. (Cambridge University Press), 1 edition. (Cited on page 10.)

[34] Jolivet, R, Kobayashi, R, Rauch, A, Naud, R, Shinomoto, S, & Gerstner, W. (2008) A benchmark test for a quantitative assessment of simple neuron models. *Journal of Neuroscience Methods* **169**, 417–424. (Cited on pages 10 and 17.)

[35] Guillamon, A, McLaughlin, D. W, & Rinzel, J. (2006) Estimation of synaptic conductances. *Journal of Physiology, Paris* **100**, 31–42. (Cited on pages 12, 31, and 105.)

[36] Song, S, Sjöström, P. J, Reigl, M, Nelson, S, & Chklovskii, D. B. (2005) Highly Nonrandom Features of Synaptic Connectivity in Local Cortical Circuits. *PLoS Biology* **3**. (Cited on page 13.)

[37] Goodman, D. (2008) Brian: a simulator for spiking neural networks in Python. *Frontiers in Neuroinformatics* **2**. (Cited on pages 16 and 118.)

[38] Sheets, P. L, Suter, B. A, Kiritani, T, Chan, C. S, Surmeier, D. J, & Shepherd, G. M. G. (2011) Corticospinal-specific HCN expression in mouse motor cortex: I(h)-dependent synaptic integration as a candidate microcircuit mechanism involved in motor control. *Journal of Neurophysiology* **106**, 2216–2231. (Cited on pages 17 and 23.)

[39] Yu, J, Anderson, C. T, Kiritani, T, Sheets, P. L, Wokosin, D. L, Wood, L, & Shepherd, G. M. G. (2008) Local-Circuit Phenotypes of Layer 5 Neurons in Motor-Frontal Cortex of YFP-H Mice. *Frontiers in Neural Circuits* **2**. (Cited on pages 17, 23, and 44.)

[40] Uhlenbeck, G. E & Ornstein, L. S. (1930) On the Theory of the Brownian Motion. *Physical Review* **36**, 823–841. (Cited on pages 17 and 18.)

[41] Rossant, C, Leijon, S, Magnusson, A. K, & Brette, R. (2011) Sensitivity of Noisy Neurons to Coincident Inputs. *The Journal of Neuroscience* **31**, 17193 –17206. (Cited on page 19.)

[42] Häusser, M & Roth, A. (1997) Estimating the Time Course of the Excitatory Synaptic Conductance in Neocortical Pyramidal Cells Using a Novel Voltage

Jump Method. *The Journal of Neuroscience* **17**, 7606 –7625. (Cited on pages 23, 44, and 78.)

[43] Berger, T. K, Perin, R, Silberberg, G, & Markram, H. (2009) Frequency-dependent disynaptic inhibition in the pyramidal network: a ubiquitous pathway in the developing rat neocortex. *The Journal of Physiology* **587**, 5411–5425. (Cited on page 23.)

[44] Silberberg, G & Markram, H. (2007) Disynaptic inhibition between neocortical pyramidal cells mediated by Martinotti cells. *Neuron* **53**, 735–746. (Cited on page 23.)

[45] Song, M, Liu, Y, Zhou, Y, Wang, K, Yu, C, & Jiang, T. (2009) *Default network and intelligence difference*. (Minneapolis, MN, USA), pp. 2212–2215. (Cited on page 23.)

[46] Markram, H, Gupta, A, Uziel, A, Wang, Y, & Tsodyks, M. (1998) Information processing with frequency-dependent synaptic connections. *Neurobiology of Learning and Memory* **70**, 101–112. (Cited on page 31.)

[47] Cohen, M. R & Kohn, A. (2011) Measuring and interpreting neuronal correlations. *Nature Neuroscience* **14**, 811–819. (Cited on page 32.)

[48] Okun, M & Lampl, I. (2008) Instantaneous correlation of excitation and inhibition during ongoing and sensory-evoked activities. *Nat Neurosci* **11**, 535–537. (Cited on page 32.)

[49] Ecker, A. S, Berens, P, Keliris, G. A, Bethge, M, Logothetis, N. K, & Tolias, A. S. (2010) Decorrelated Neuronal Firing in Cortical Microcircuits. *Science* **327**, 584 –587. (Cited on page 32.)

[50] Larkman, A. U. (1991) Dendritic morphology of pyramidal neurones of the visual cortex of the rat: III. Spine distributions. *The Journal of Comparative Neurology* **306**, 332–343. (Cited on page 33.)

[51] Abeles, M. (1991) *Corticonics: neural circuits of the cerebral cortex*. (Cambridge University Press, Cambridge; New York). (Cited on page 33.)

[52] Ramaswamy, S, Hill, S. L, King, J. G, Schürmann, F, Wang, Y, & Markram, H. (2011) Intrinsic Morphological Diversity of Thick-tufted Layer 5 Pyramidal Neurons Ensures Robust and Invariant Properties of in silico Synaptic Connections. *The Journal of Physiology*. (Cited on pages 33 and 107.)

[53] Poulet, J. F. A & Petersen, C. C. H. (2008) Internal brain state regulates membrane potential synchrony in barrel cortex of behaving mice. *Nature* **454**, 881–885. (Cited on pages 33 and 102.)

[54] Poulet, J. F. A, Fernandez, L. M. J, Crochet, S, & Petersen, C. C. H. (2012) Thalamic control of cortical states. *Nature Neuroscience* **15**, 370–372. (Cited on pages 33 and 102.)

[55] Crochet, S & Petersen, C. C. H. (2006) Correlating whisker behavior with membrane potential in barrel cortex of awake mice. *Nature Neuroscience* **9**, 608–610. (Cited on pages 33 and 102.)

[56] Rall, W. (1967) Distinguishing theoretical synaptic potentials computed for different soma-dendritic distributions of synaptic input. *Journal of Neurophysiology* **30**, 1138–1168. (Cited on page 36.)

[57] Hay, E, Hill, S, Schürmann, F, Markram, H, & Segev, I. (2011) Models of Neocortical Layer 5b Pyramidal Cells Capturing a Wide Range of Dendritic and Perisomatic Active Properties. *PLoS Comput Biol* **7**, e1002107. (Cited on pages 37, 43, 66, and 78.)

[58] Gidon, A & Segev, I. (2012) Principles Governing the Operation of Synaptic Inhibition in Dendrites. *Neuron* **75**, 330–341. (Cited on page 40.)

[59] Vogels, T. P. (2007) Ph.D. thesis (Brandeis University). (Cited on pages 42, 63, 64, and 105.)

[60] Hines, M & Carnevale, N. (1997) The NEURON simulation environment. (Cited on pages 43 and 78.)

[61] Butcher, J. C. (2009) *By J. C. Butcher - Numerical Methods for Ordinary Differential Equations: 2nd (second) Edition*. (Wiley, John & Sons, Incorporated). (Cited on page 43.)

[62] Meyer, H. S, Wimmer, V. C, Hemberger, M, Bruno, R. M, de Kock, C. P. J, Frick, A, Sakmann, B, & Helmstaedter, M. (2010) Cell type-specific thalamic innervation in a column of rat vibrissal cortex. *Cerebral Cortex (New York, N.Y.: 1991)* **20**, 2287–2303. (Cited on page 43.)

[63] Furtak, S. C, Moyer, J. R, & Brown, T. H. (2007) Morphology and ontogeny of rat perirhinal cortical neurons. *The Journal of Comparative Neurology* **505**, 493–510. (Cited on page 43.)

[64] Ascoli, G. A, Donohue, D. E, & Halavi, M. (2007) NeuroMorpho.Org: A Central Resource for Neuronal Morphologies. *The Journal of Neuroscience* **27**, 9247–9251. (Cited on page 43.)

[65] Wolfram Research, I. (2010) *Mathematica*. Vol. 8.0. (Cited on page 46.)

[66] Destexhe, A. (2001) Simplified models of neocortical pyramidal cells preserving somatodendritic voltage attenuation. *Neurocomputing* **38–40**, 167–173. (Cited on page 62.)

[67] Vogels, T. P, Rajan, K, & Abbott, L. (2005) NEURAL NETWORK DYNAMICS. *Annual Review of Neuroscience* **28**, 357–376. (Cited on page 63.)

[68] Izhikevich, E. M. (2004) Which model to use for cortical spiking neurons? *IEEE Trans Neural Netw* **15**, 1063–70. (Cited on page 63.)

[69] Brunel, N. (2000) Dynamics of sparsely connected networks of excitatory and inhibitory spiking neurons. *Journal of Computational Neuroscience* **8**, 183–208. (Cited on page 63.)

[70] Vogels, T. P & Abbott, L. F. (2005) Signal Propagation and Logic Gating in Networks of Integrate-and-Fire Neurons. *The Journal of Neuroscience* **25**, 10786–10795. (Cited on page 63.)

[71] Cavallari, S, Panzeri, S, & Mazzoni, A. (2014) Comparison of the dynamics of neural interactions between current-based and conductance-based integrate-and-fire recurrent networks. *Frontiers in Neural Circuits* **8**. (Cited on pages 63 and 105.)

[72] Poirazi, P, Brannon, T, & Mel, B. W. (2003) Pyramidal neuron as two-layer neural network. *Neuron* **37**, 989–999. (Cited on pages 65, 98, and 107.)

[73] Jia, H, Rochefort, N. L, Chen, X, & Konnerth, A. (2010) Dendritic organization of sensory input to cortical neurons in vivo. *Nature* **464**, 1307–1312. (Cited on page 65.)

[74] Parekh, R & Ascoli, G. A. (2013) Neuronal Morphology Goes Digital: A Research Hub for Cellular and System Neuroscience. *Neuron* **77**, 1017–1038. (Cited on page 67.)

[75] Qi, G, Radnikow, G, & Feldmeyer, D. (2015) Electrophysiological and morphological characterization of neuronal microcircuits in acute brain slices using paired patch-clamp recordings. *Journal of Visualized Experiments: JoVE* p. 52358. (Cited on pages 67 and 107.)

[76] Perin, R, Berger, T. K, & Markram, H. (2011) A synaptic organizing principle for cortical neuronal groups. *Proceedings of the National Academy of Sciences*. (Cited on pages 67 and 107.)

[77] Thomson, A. M & Lamy, C. (2007) Functional Maps of Neocortical Local Circuitry. *Frontiers in Neuroscience* **1**, 19–42. (Cited on page 67.)

[78] Shepherd, G. M & Harris, K. M. (1998) Three-dimensional structure and composition of CA3–>CA1 axons in rat hippocampal slices: implications for presynaptic connectivity and compartmentalization. *The Journal of Neuroscience: The Official Journal of the Society for Neuroscience* **18**, 8300–8310. (Cited on pages 67 and 107.)

[79] Mishchenko, Y, Hu, T, Spacek, J, Mendenhall, J, Harris, K. M, & Chklovskii, D. B. (2010) Ultrastructural analysis of hippocampal neuropil from the connectomics perspective. *Neuron* **67**, 1009–1020. (Cited on pages 67 and 107.)

[80] Anderson, J. R, Jones, B. W, Yang, J.-H, Shaw, M. V, Watt, C. B, Koshevoy, P, Spaltenstein, J, Jurrus, E, UV, K, Whitaker, R. T, Mastronarde, D, Tasdizen, T, & Marc, R. E. (2009) A Computational Framework for Ultrastructural Mapping of Neural Circuitry. *PLoS Biol* **7**, e1000074. (Cited on pages 67 and 107.)

[81] Boucsein, C, Nawrot, M, Rotter, S, Aertsen, A, & Heck, D. (2005) Controlling Synaptic Input Patterns In Vitro by Dynamic Photo Stimulation. *J Neurophysiol* **94**, 2948–2958. (Cited on pages 69 and 70.)

[82] Nawrot, M. P, Boucsein, C, Rodriguez Molina, V, Riehle, A, Aertsen, A, & Rotter, S. (2008) Measurement of variability dynamics in cortical spike trains. *Journal of Neuroscience Methods* **169**, 374–390. (Cited on page 69.)

[83] Schnepel, P, Kumar, A, Zohar, M, Aertsen, A, & Boucsein, C. (2014) Physiology and Impact of Horizontal Connections in Rat Neocortex. *Cerebral Cortex* p. bhu265. (Cited on page 69.)

[84] Fan, Rong-En, K.-W. C. (2008) LIBLINEAR: A Library for Large Linear Classification. *Journal of Machine Learning Research* **9**, 1871–1874. (Cited on page 73.)

[85] Pedregosa, F, Varoquaux, G, Gramfort, A, Michel, V, Thirion, B, Grisel, O, Blondel, M, Prettenhofer, P, Weiss, R, Dubourg, V, Vanderplas, J, Passos, A, Cournapeau, D, Brucher, M, Perrot, M, & Duchesnay, É. (2012) Scikit-learn: Machine Learning in Python. *arXiv:1201.0490 [cs]*. arXiv: 1201.0490. (Cited on page 73.)

[86] Binzegger, T, Douglas, R. J, & Martin, K. A. C. (2004) A Quantitative Map of the Circuit of Cat Primary Visual Cortex. *The Journal of Neuroscience* **24**, 8441 –8453. (Cited on page 98.)

[87] Williams, S. R & Mitchell, S. J. (2008) Direct measurement of somatic voltage clamp errors in central neurons. *Nat Neurosci* **11**, 790–798. (Cited on page 99.)

[88] Feng, J, Xu, H, Mannor, S, & Yan, S. (2014) Robust Logistic Regression and Classification. *NIPS procedings*. (Cited on page 100.)

[89] Fan, R.-E, Chen, P.-H, & Lin, C.-J. (2005) Working Set Selection Using Second Order Information for Training Support Vector Machines. *J. Mach. Learn. Res.* **6**, 1889–1918. (Cited on page 100.)

[90] McNaughton, B. L, O'Keefe, J, & Barnes, C. A. (1983) The stereotrode: a new technique for simultaneous isolation of several single units in the central nervous system from multiple unit records. *Journal of Neuroscience Methods* **8**, 391–397. (Cited on page 102.)

[91] Drake, K. L, Wise, K. D, Farraye, J, Anderson, D. J, & BeMent, S. L. (1988) Performance of planar multisite microprobes in recording extracellular single-unit intracortical activity. *IEEE transactions on bio-medical engineering* **35**, 719–732. (Cited on page 102.)

[92] Göbel, W, Kampa, B. M, & Helmchen, F. (2007) Imaging cellular network dynamics in three dimensions using fast 3d laser scanning. *Nature Methods* **4**, 73–79. (Cited on pages 102 and 106.)

[93] Grewe, B. F, Langer, D, Kasper, H, Kampa, B. M, & Helmchen, F. (2010) High-speed in vivo calcium imaging reveals neuronal network activity with near-millisecond precision. *Nat Meth* **7**, 399–405. (Cited on pages 102 and 106.)

[94] Siegel, F & Lohmann, C. (2013) Probing synaptic function in dendrites with calcium imaging. *Experimental Neurology* **242**, 27–32. (Cited on pages 102 and 106.)

[95] Fritschy, J.-M, Panzanelli, P, & Tyagarajan, S. K. (2012) Molecular and functional heterogeneity of GABAergic synapses. *Cellular and molecular life sciences: CMLS* **69**, 2485–2499. (Cited on page 104.)

[96] Kole, M. H. P, Hallermann, S, & Stuart, G. J. (2006) Single Ih channels in pyramidal neuron dendrites: properties, distribution, and impact on action potential output. *The Journal of Neuroscience: The Official Journal of the Society for Neuroscience* **26**, 1677–1687. (Cited on page 105.)

[97] Letzkus, J. J, Kampa, B. M, & Stuart, G. J. (2006) Learning rules for spike timing-dependent plasticity depend on dendritic synapse location. *The Journal of Neuroscience: The Official Journal of the Society for Neuroscience* **26**, 10420–10429. (Cited on page 107.)

[98] Amirikian, B. (2005) A Phenomenological Theory of Spatially Structured Local Synaptic Connectivity. *PLoS Comput Biol* **1**, e11. (Cited on page 107.)

[99] Laughlin, S. (1981) A simple coding procedure enhances a neuron's information capacity. *Zeitschrift Für Naturforschung. Section C: Biosciences* **36**, 910–912. (Cited on page 109.)

[100] Stemmler, M & Koch, C. (1999) How voltage-dependent conductances can adapt to maximize the information encoded by neuronal firing rate. *Nature Neuroscience* **2**, 521–527. (Cited on page 109.)

[101] Perrinet, L. U. (2010) Role of homeostasis in learning sparse representations. *Neural Computation* **22**, 1812–1836. (Cited on page 109.)

[102] Triesch, J. (2007) Synergies Between Intrinsic and Synaptic Plasticity Mechanisms. *Neural Computation* **19**, 885–909. (Cited on page 109.)

[103] Lazar, A, Pipa, G, & Triesch, J. (2009) SORN: A Self-Organizing Recurrent Neural Network. *Frontiers in Computational Neuroscience* **3**. (Cited on page 109.)

[104] Naudé, J, Cessac, B, Berry, H, & Delord, B. (2013) Effects of cellular homeostatic intrinsic plasticity on dynamical and computational properties of biological recurrent neural networks. *The Journal of Neuroscience: The Official Journal of the Society for Neuroscience* **33**, 15032–15043. (Cited on page 109.)

[105] Horn, D, Levy, N, & Ruppin, E. (1996) Neuronal-based synaptic compensation: a computational study in Alzheimer's disease. (Cited on page 109.)

[106] Frohlich, F & Bazhenov, M. (2008) Pathological effect of homeostatic synaptic scaling on network dynamics in diseases of the cortex. (Cited on page 109.)

[107] Chakroborty, S, Goussakov, I, & Miller, M. (2009) Deviant ryanodine receptor-mediated calcium release resets synaptic homeostasis in presymptomatic 3xtg-AD mice. (Cited on page 109.)

[108] Davis, G. W. (2006) Homeostatic control of neural activity: from phenomenology to molecular design. *Annual Review of Neuroscience* **29**, 307–323. (Cited on page 109.)

[109] Turrigiano, G. (2011) Too many cooks? Intrinsic and synaptic homeostatic mechanisms in cortical circuit refinement. *Annual Review of Neuroscience* **34**, 89–103. (Cited on page 109.)

[110] Desai, N. S, Rutherford, L. C, & Turrigiano, G. G. (1999) Plasticity in the intrinsic excitability of cortical pyramidal neurons. *Nature Neuroscience* **2**, 515–520. (Cited on pages 110 and 128.)

[111] van Welie, I, Hooft, J. A. v, & Wadman, W. J. (2004) Homeostatic scaling of neuronal excitability by synaptic modulation of somatic hyperpolarization-activated Ih channels. *Proceedings of the National Academy of Sciences of the United States of America* **101**, 5123–5128. (Cited on page 110.)

[112] O'Leary, T, van Rossum, M. C. W, & Wyllie, D. J. A. (2010) Homeostasis of intrinsic excitability in hippocampal neurones: dynamics and mechanism of the response to chronic depolarization. *The Journal of Physiology* **588**, 157–170. (Cited on pages 110 and 128.)

[113] Kuba, H, Oichi, Y, & Ohmori, H. (2010) Presynaptic activity regulates Na+ channel distribution at the axon initial segment. *Nature* **465**, 1075–1078. (Cited on page 110.)

[114] Grubb, M. S & Burrone, J. (2010) Activity-dependent relocation of the axon initial segment fine-tunes neuronal excitability. *Nature* **465**, 1070–1074. (Cited on page 110.)

[115] O'Leary, T & Wyllie, D. J. A. (2011) Neuronal homeostasis: time for a change? *The Journal of Physiology* **589**, 4811–4826. (Cited on page 110.)

[116] Karmarkar, U. R & Buonomano, D. V. (2006) Different forms of homeostatic plasticity are engaged with distinct temporal profiles. *The European Journal of Neuroscience* **23**, 1575–1584. (Cited on pages 110 and 128.)

[117] Gal, A, Eytan, D, Wallach, A, Sandler, M, Schiller, J, & Marom, S. (2010) Dynamics of Excitability over Extended Timescales in Cultured Cortical Neurons. *The Journal of Neuroscience* **30**, 16332 –16342. (Cited on pages 110 and 128.)

[118] Distefano, J. J. (2014) *Schaum's Outline of Feedback and Control Systems, 2nd Edition*. (McGraw-Hill Professional, New York, NY), 2 edition edition. (Cited on pages 111 and 112.)

[119] Leigh, J. R. (1992) *Control Theory: A Guided Tour*. (P. Peregrinus on the behalf of the Institution of Electrical Engineers). (Cited on page 117.)

[120] Fujii, K & Shoji, K. (1972) Verification of the Aizerman and/or Kalman conjecture. *IEEE Transactions on Automatic Control* **17**, 406–408. (Cited on page 117.)

[121] Seung, H. S, Lee, D. D, Reis, B. Y, & Tank, D. W. (2000) Stability of the memory of eye position in a recurrent network of conductance-based model neurons. *Neuron* **26**, 259–271. (Cited on page 128.)

[122] Gold, J. I & Shadlen, M. N. (2007) The neural basis of decision making. *Annual Review of Neuroscience* **30**, 535–574. (Cited on page 128.)

[123] O'Donnell, C & Nolan, M. F. (2010) Tuning of synaptic responses: an organizing principle for optimization of neural circuits. *Trends in Neurosciences*. (Cited on page 129.)

[124] Abbott, L & LeMasson, G. (1993) Analysis of Neuron Models with Dynamically Regulated Conductances. *Neural Computation* **5**, 823–842. (Cited on page 129.)

[125] Zenke, F, Hennequin, G, & Gerstner, W. (2013) Synaptic Plasticity in Neural Networks Needs Homeostasis with a Fast Rate Detector. *PLoS Computational Biology* **9**. (Cited on page 129.)

[126] Remme, M. W. H & Wadman, W. J. (2012) Homeostatic Scaling of Excitability in Recurrent Neural Networks. *PLoS Comput Biol* **8**, e1002494. (Cited on page 129.)